Dark Matter Searches in the Gamma-ray Sky with the Fermi-LAT Space Telescope

Doctoral thesis by:
Germán A. Gómez Vargas

Dark Matter Searches in the Gamma-ray Sky with the *Fermi*-LAT Space Telescope

Germán Arturo Gómez Vargas

T E S I S D O C T O R A L

Presentada ante el Departamento de Física Teórica
de la Universidad Autónoma de Madrid (UAM)
para la obtención del titulo de Doctor

Proyecto dirigido por los Profesores:

Luis Labarga y Carlos Muñoz

Madrid, Septiembre 2013

Acknowledgments

Nada de esto hubiera sido posible sin el apoyo incondicional de mi Mamá, me lo ha dado todo.

I am especially grateful to Luis Labarga and Carlos Muñoz, they have granted me the freedom I wanted and given me the guidance I needed, providing the best possible environment for the completion of this thesis. Also, I want to express my deeply felt gratitude towards Aldo Morselli for giving me the opportunity to work in the *Fermi*-LAT collaboration and visit la bella Italia many times.

Furthermore, I thank Jenny Siegal-Gaskins, Beatriz Cañadas, Fernando Campos, Mattia Fornasa, Guðlaugur Jóhannesson, and Vincenzo Vitale. I have learned a lot of physics and/or computer stuff from that people. Also, a big thanks to all the co-authors of my papers, it has been a real pleasure to work with all of them!

I thank Stanford, SLAC, Caltech, INFN Tor Vergata, and KITPC Beijing for their hospitality, part of this thesis was made there. Also to the *Fermi*-LAT collaboration, this thesis is only possible due to its work.

To the UAM astro-ph journal club for introduce me the world of N-body cosmological simulations, specially Alexander Knebe for his clear explanations.

To the Italian team for giving me a lot of fun and food: Edoardo Carlesi, Adriano Bonforti, Arianna di Cintio, Elodie Louis de Malherbe, Elisabetta Majerotto, Stefania Sarno, and many other Italians that I have the pleasure to meet during my PhD journey all around the planet Earth.

To the Rios Rosas girls: Deicy Tabares, Cristina de Blas, Andrea Ruiz, and Andrea Pacheco, they remained me Colombia and life outside physics.

To the IFT kitchen girls: Monica Encinas, Susana Hernandez, Isabel Pérez, Chabely Prats, and Roxana Rodríguez, for their helpful admin work and the transcendental conversations at lunch time.

This work was supported by the Spanish MINECO's Consolider-Ingenio 2010 Programme under grant MultiDark CSD2009-00064. Also supported in part by MINECO under grants FPA2009-08958 and FPA2012-34694, and under the 'Centro de Excelencia Severo Ochoa' Programme SEV-2012-0249, by the Comunidad de Madrid under grant HEPHACOS S2009/ESP-1473, and by the European Union under the Marie Curie-ITN program PITN-GA-2009-237920.

Lo que ocurrió en la canoa

En ese entonces no existía la noche,
había que viajar siempre en la luz.

Él le había dado a cada uno un regalo,
cosas ocultas que no había que mirar.
Pero uno de ellos abrió la bolsa oscura
y brotaron de ella las hormigas.
Cubrieron las manos, los brazos, el cuerpo,
cubrieron los vecinos, la canoa, el agua,
cubrieron todas las paredes del cielo
y así llegó la noche.

Pamurí-maxsé dio a cada uno un cocuyo
y en esa débil claridad avanzaron.
Las hormigas eran más y más a cada instante,
iban llenando todo.
Entonces vino el hombre amarillo
vino el sol con su corona de plumas
y a él no lo cubrían las hormigas.

Con una vara hizo retroceder la mancha oscura
devolvió las hormigas a la bolsa
llenó la bolsa con millones de hormigas.
Pero ya no cabían en ella y se regaron por la selva.

Aunque volvió la luz, desde entonces existe la noche,
pero ninguna noche será tan cerrada,
tan espesa y oscura como la noche de la hormiga.

Llegaron a la roca, la gran roca horadada,
creyendo que habían alcanzado el final de su viaje.
Salieron por un hueco en la punta de la canoa.

Se dispersaron por el mundo antes de tiempo
llevando cada uno su regalo.

El arco y la flecha, la vara de pescar,
el rallo de yuca,
la cerbatana y el canasto,
la máscara de tela de corteza.

Los hombres escogieron dónde vivir.
En las orillas, en la selva, en las cabeceras de los ríos,
en las nubes, arriba.

William Ospina.

Contents

1 Introduction **1**
- 1.1 Prologue . . . 1
- 1.2 Publications . . . 7

2 Dark matter shapes the universe **9**
- 2.1 Dark matter halos . . . 9
  - 2.1.1 Extragalactic distribution . . . 11
  - 2.1.2 Milky Way's halo density profile . . . 13
- 2.2 The WIMP scenario . . . 16
  - 2.2.1 Gamma-ray flux from WIMP annihilation . . . 18
- 2.3 The $\mu\nu$SSM and gravitino dark matter . . . 22
  - 2.3.1 Gamma-rays from gravitino decay in the $\mu\nu$SSM . . . 24

3 The Fermi-LAT instrument **27**
- 3.1 Telescope components . . . 28
- 3.2 Performance . . . 30
- 3.3 Science analysis environment . . . 31
  - 3.3.1 Binned likelihood analysis . . . 31

4 Line signal and background **35**
- 4.1 CLUES on *Fermi*-LAT prospects for detection of $\mu\nu$SSM gravitino DM . . . 36
  - 4.1.1 Introduction . . . 36
  - 4.1.2 Simulations with the Fermi Science Tools . . . 37
  - 4.1.3 $\mu\nu$SSM gravitino dark matter: prospects of detection with Fermi-LAT . . . 38
  - 4.1.4 Conclusions and outlook . . . 42
- 4.2 Tentative line at 130 GeV? . . . 43
  - 4.2.1 The *Fermi*-LAT search for gamma-ray lines: focusing on 130 GeV . . . 45
  - 4.2.2 Fitting results and upper limits . . . 46
  - 4.2.3 133 GeV feature in the control regions . . . 46
  - 4.2.4 Conclusions . . . 49

5 Diffuse signal and background in the inner region of the Milky Way **53**
- 5.1 Constraints on WIMP Annihilation for contracted DM in the Inner Galaxy with the *Fermi*-LAT . . . 54

5.1.1 DM density profiles 55
5.1.2 DM induced gamma rays from WIMP annihilations 56
5.1.3 Gamma-ray flux from *Fermi*-LAT measurements 58
5.1.4 Flux measurement 61
5.1.5 Limits on the dark matter annihilation cross-section 61
5.1.6 Conclusions 66
5.2 *Fermi*-LAT view of the inner Galaxy 66
5.2.1 Diffuse emission model uncertainties 67
5.2.2 Fitting procedure and preliminary results 69
5.2.3 Conclusions 70

6 Measurement of anisotropies in the gamma-ray diffuse background: DM signal and background 73
6.1 *Fermi*-LAT measurement of anisotropies in the IGRB 74
6.1.1 The angular power spectrum (APS) as a metric for anisotropy 75
6.1.2 Method 75
6.1.3 Results and conclusions 76
6.2 DM implications of *Fermi*-LAT measurement of anisotropies in the IGRB 78
6.2.1 DM predictions 78
6.2.2 Setting constraints 79
6.2.3 Preliminary results 79

7 Conclusions and Outlook 85

Bibliography 89

Chapter 1

Introduction

Voy a contarte cómo es el mundo que vamos a conquistar.
William Ospina, *La serpiente sin ojos*.

Contents

1.1 Prologue 1
1.2 Publications 7

1.1 Prologue

Since the last few years two fields of physics that remained separated have started to interact, elementary particle physics and cosmology. On one hand, particle physics ideas help in cosmological issues, and on the other hand the most compelling evidences for physics beyond the standard model (BSM) come from observations at both cosmological and astrophysical level.

At cosmological scales the analysis of anisotropies observed in the cosmic microwave background shed light on important parameters of the early universe. For instance, the amplitude of the gravitational potential when photons decoupled from matter and the baryon content of the primordial plasma can be measured from the height of the peaks of anisotropies produced by acoustic oscillations [1]. The amount of baryons needed to explain the amplitude of the potential inferred is quite larger than the measured value [2, 3].

Galaxy clusters are at the cross-roads of cosmology and astrophysics scales. In these systems the largest amount of visible matter is in the form of hot gas that can be detected with X-ray satellites. However, galaxies bounded to clusters feel gravitational forces that can not be explained using the gas mass observed [4, 5]. Historically, Fritz Zwicky in the 1930's realized that galaxies in the Coma cluster seem to be moving too fast to keep held bound by their mutual gravity [6].

On galactic scales valuable information on galaxies can be extracted from their rotation curves. This relate the velocity of stars or gas in galaxies with their orbits. In spiral galaxies the flatness of rotation curves reveals that stars and gas are moving

in a gravitational potential many times larger than the one produced by all the material observed within their orbits [7].

In addition, some Hubble Space Telescope images of galaxies and clusters look as if they were seen through wavy glass. It is because gravity bends light rays. Making use of this, the total mass of gravitational bound systems can be inferred from their influence on the light emitted by objects behind them. This phenomenon is called gravitational lensing. A discrepancy in all the cosmic lenses detected has been established, the mass needed to explain distortions in images is larger than the observed mass of the foreground systems [8].

The discrepancies presented above, among others, are based on the assumption that light trace matter. However to make sense of dynamics, distribution, or shape of celestial objects that emit any type of light, a material that does not interact electromagnetically is invoked [9, 10, 11], this is known as Dark Matter (DM). In the framework of the standard cosmological model, Λ Cold Dark Matter (ΛCDM), DM make up 26.8% of the universe's energy density budget, and about 85% of its total mass [2, 3, 12]. Without it, galaxies (including our own) would never be formed [13].

DM can be probed detecting the unseen matter needed. In this thesis we aim on shedding light on the DM issue by focussing on the understanding of its fundamental nature and the observational search for particles of DM. First, we need to figure out what all the observed discrepancies imply for the DM particle's nature. The evidences only can tell us that DM has to be mainly non-baryonic [14, 15]. If we assume that DM is baryonic, the DM density needed to account the observations at cosmological scales there is a direct conflict with the Helium, Deuterium and Lithium abundances successfully predicted by primordial nucleosynthesis and confirmed by observations [16, 17].

The Standard Model (SM) of particle physics does not provide any viable non-baryonic candidate, therefore we need to look into theories BSM for particles that can fulfill the requirements of being the fundamental bricks of the DM. Exotic particles in theories BSM that can make up the DM normally have interactions other than gravitational with particles of the SM and therefore, in DM annihilation or decay some of them may be created. The SM particles produced in this way would induce measurable effects in astrophysical observations, modifying fluxes and spatial distribution of cosmic rays (CR), i.e. protons, antiprotons, electrons, positrons, gamma-rays and neutrinos arriving to the Earth. This was proposed first in the context of CR anti-Protons for photino DM by Silk and Srednicki in [18]. Since charged cosmic rays are deflected by interstellar magnetic fields, disentangle their sources is not straightforward. Therefore we focus on DM-induced gamma-rays: they are expected to be only marginally affected by energy loses and because of it, to travel along geodesics. Search for non-gravitational signals of DM in the gamma-ray sky is the main subject of this thesis.

In order to extract information on the DM nature from gamma-ray data some characteristics of DM candidates in BSM theories must be convolved with the distribution of DM around us predicted by cosmological N-body simulations. In this way we can calculate both, flux and distribution of DM-induced gamma-rays on the sky. The basic characteristics of DM candidates relevant for gamma-ray searches are:

- DM mass, m_{DM}, since it sets the energy scale of the gamma-rays produced.
- Annihilation rate $\sigma_{ann}v$ or lifetime τ_{dec} for stable or decaying DM, respectively
- The number of SM particles produced due to DM annihilation or decay, $N_{\gamma,ann}$ and $N_{\gamma,dec}$ respectively.

With those characteristics we can predict energy spectral signatures of DM, like sharp features. The ingredients needed to calculate the prompt gamma-ray emission in a volume V containing DM particles are sketched in the following equations:

$$\Phi\gamma, ann = \left(N_{\gamma,ann}\right) \times (\sigma_{ann}v) \times \left(\int \frac{\rho_{DM}^2}{m_{DM}^2} dV\right), \tag{1.1}$$

$$\Phi\gamma, dec = \left(N_{\gamma,dec}\right) \times \left(\frac{1}{\tau_{dec}}\right) \times \left(\int \frac{\rho_{DM}}{m_{DM}} dV\right) \tag{1.2}$$

where the DM-SM cross section times DM relative velocity $\sigma_{ann}v$ and the inverse of the DM lifetime $1/\tau_{dec}$, for annihilation and decay respectively, measure the connection of visible to dark matter and can be related to the mechanism of DM production in the early universe. The integrals give the number of DM particle pairs, in the case of annihilation, or DM particles for decay, in V. ρ_{DM} encloses the information on the spatial DM distribution and density.

Estimates of ρ_{DM} are obtained from cosmological N-body simulations; they provide the preferred regions of the sky to look for a DM signal, i.e., those with the highest expected DM concentrations and still close enough to yield high DM-induced fluxes at the Earth: the Galactic Center (GC), nearby dwarf spheroidal galaxy (dSphs) satellites of the Milky Way, as well as local galaxy clusters are thought to be among the most promising objects for DM searches.

It is worth noting that even if those systems were DM dominated and could produce detectable signals on the Earth, there are other astrophysical gamma-ray emitters that could contaminate the signal and indeed account for almost all the gamma-rays observed by space and ground based telescopes. Furthermore, as gamma-ray astronomy is a relatively new field of research, most of those background sources are poorly understood, thus making difficult to disentangle a DM

signal. Other potential difficulty at DM searches are instrumental effects, since gamma rays cannot be observed by optical methods, particle detectors, that have very poor energy and spatial resolution in comparison with optical telescopes, are needed to perform the observations. Since gamma rays are absorbed by the Earth's atmosphere they can not be detected directly by telescopes on the Earth. Imaging Air Cherenkov Telescopes (IACTs) detect Cherenkov light produced by interaction of gamma rays arriving to the planet with the atmosphere. Currently there are three operating IACTs systems: HESS, MAGIC and VERITAS. They can only make pointing observations and need complex algorithms to discriminate gamma rays from a huge cosmic-ray background. Another possibility to detect gamma rays is with space-based telescopes that can observe the gamma-ray sky directly.

In this thesis, observations are made using the Fermi Large Area Telescope (*Fermi*-LAT), the main instrument of the Fermi satellite on orbit since June 11, 2008 [19]. The *Fermi*-LAT performs gamma-ray measurements covering an energy range from $\sim$ 20 MeV to $>$ 300 GeV over the whole celestial sphere. It has detected point and small extended sources, e.g. blazars, supernova remnants (SNRs) and pulsars [20], and a strong diffuse component in the whole sky first observed by the OSO-3 satellite in the inner Galaxy region [21]. The main contribution of the diffuse emission is correlated with Milky Way structures, those gamma-rays arise from interactions of high-energy cosmic rays with the interstellar medium and the interstellar radiation field (ISRF). A fainter component considered to have an isotropic or nearly isotropic distribution on the sky, the so-called isotropic gamma-ray background (IGRB), has also been observed.

The main purpose of this work is the analysis of the gamma-ray sky in order to probe the DM paradigm by testing the predictions of theories BSM on gamma-ray signatures induced by particle's DM annihilation or decay. The analysis implicitly carries the needed thorough study of astrophysical and instrumental backgrounds that can mimic those signals; this also constituting a significant part of the work.

In chapter 2 we present results of N-body simulations of galactic and extra-galactic DM structures in order to predict their distribution on the sky. Also we discus some of the exotic particle candidates for DM and the way how they produce gamma-ray signals that could be detected by the *Fermi*-LAT. In chapter 3 the *Fermi*-LAT telescope is described. In chapters 4, 5 and 6 we present observations of the target regions optimized for DM searches, the subsequent data analysis and the comparison with optimum predictions. These chapters are based on original work already published in peer review journals or about to be published. Conclusions and outlook about further work are presented in chapter 7.

A more detail description of chapters 4, 5 and 6 follows:

- In chapter 4 we present the work [22] carried out in collaboration with Dr. M. Fornasa (Nottingham), Dr. F. Zandanel (GRAPPA), Dr. A. J. Cuesta

(Yale), Prof. C. Munoz (UAM & IFT), Prof. F. Prada (UAM & IFT) and Prof. G. Yepes (UAM). We study the gamma-ray line produced by gravitinos as DM in a new, phenomenologically well motivated, supersymmetric model, the $\mu\nu$SSM, proposed some years ago by one of my advisors, Prof. Carlos Muñoz [23, 24]. In particular, for this work we simulate both DM signals and background, and set prospects of gravitino DM detection in the region of the Virgo cluster. We have confirmed the potential of using extragalactic massive structures as optimal targets for decaying DM detection.

In addition, in this chapter we present the bottom line and main conclusions of our the work [25] where the *Fermi*-LAT collaboration performs a thorough search of gamma-ray lines paying special attention to the energy range about 130 GeV, where the detection of a line has been claimed [26, 27].

- In chapter 5 we discuss the Fermi-MultiDark[1] project [28], category II paper of the *Fermi*-LAT collaboration, focused on the inner region of the Milky Way. This is one of the most interesting and complicated regions of the gamma-ray sky because of the many point sources and potential confusion, the uncertainties associated with the diffuse gamma-ray emission, together with the potential for DM detection. We derive constraints on parameters of generic dark matter candidates by comparing theoretical predictions with the gamma-ray emission observed by the *Fermi*-LAT from the region around the Galactic Center. Our analysis is conservative since it simply requires that the expected dark matter signal does not exceed the observed emission. The constraints obtained in the likely case that the collapse of baryons to the Galactic Center is accompanied by the contraction of the DM are strong. My role in this project was the *Fermi*-LAT data analysis, the optimization of the region of interest (in collaboration with Dr. J.-H. Huh (UCLA)), the estimate of the predictions for DM density profile (in collaboration Prof. A. Klypin (New Mexico State), Prof. F. Prada and Dr. M Sánchez-Conde (SLAC)) and the setting of constraints from the comparison between data and DM predictions (in collaboration with Dr. J.-H. Huh and M. Peiró (IFT & UAM)).

  In addition, I have performed within *Fermi*-LAT a novel analysis of this region based on GALPROP [29] [2] (in collaboration with Prof. Igor V. Moskalenko and Prof. Troy Porter), during my stay at Stanford University in 2011. The preliminary results of this work were presented at the Fermi

[1] Multimessenger Approach for Dark Matter Detection (MultiDark) is a Spanish Project supported by the Consolider-Ingenio 2010 Programme of the Ministry of Economy and Competitiveness. The main goal of MultiDark is to push forward the Spanish position in the field by creating synergies and collaborations among the participating groups, in order to contribute significantly to the worldwide efforts to identify and detect the dark matter. `http://www.multidark.es/`

[2] A numerical code for cosmic-ray transport and diffuse emission production.

Symposium 2011 at Rome by Prof. Troy Porter, and also by myself at the international workshop DSU 2011 at Beijing [3]. In summary, regarding the uncertainties in the astrophysical inputs for the calculation of a diffuse gamma-ray emission model, after subtraction of a physically-motivated model based on GALPROP from the *Fermi*-LAT data, the residual is compatible with detected point sources and small fluctuations.

- In chapter 6, first the angular power spectrum (APS) measurement of the extragalactic gamma-ray background is presented [30]. My contribution to this category I paper of the whole *Fermi*-LAT collaboration was the creation and analysis of residual maps between real and mock dataset. Second, we have analysed the implication of this work for DM studies in the Fermi-MultiDark project [31, 32]. In this project we set constrains on generic DM models using the APS measured. MultiDark contributes with predictions of the DM distribution from N-body simulations and well motivated extrapolations of those simulations to small scales, as presented in ref. [33]. Multidark also provides gamma-ray yield by both, prompt and inverse Compton scattering (ICS) emission in DM decay and annihilation. During my research stay in Caltech in 2012 in collaboration with Dr. M. Fornasa and Dr. J. Siegal-Gaskins (Caltech) we make the DM-induced APS predictions for different DM masses and annihilation/decay channels based on the maps presented in [33]. In parallel with Dr. A. Cuocco (Torino), Prof. E. Komatsu (MPI for Astrophysics), Dr. T. Linden (U. of Chicago), and Dr. J. Siegal-Gaskins, we have updated the *Fermi*-LAT APS measurement using 45 months data and new *Fermi*-LAT performance [32]. Using the DM predictions and the already published APS measurement [30] we have set interesting constraints on annihilating DM [31].

[3] http://kitpc.itp.ac.cn/dsu2011/index.html

1.2 Publications

This thesis gave rise to the following papers:

Peer review publications

1. Constraints on WIMP Annihilation for Contracted Dark Matter in the Inner Galaxy with the *Fermi*-LAT

G. A. Gomez-Vargas, M. A. Sanchez-Conde, J-H Huh, M. Peiro, F. Prada, A. Morselli, A. Klypin, D. G. Cerdeño, Y. Mambrini, C. Muñoz. *JCAP* **1210** *(2013) 029*

2. Dark Matter implications of *Fermi*-LAT measurement of anisotropies in the diffuse gamma-ray background

G. A. Gomez-Vargas, A. Cuoco, T. Linden, M.A. Sanchez-Conde, and J.M. Siegal-Gaskins for the *Fermi*-LAT collaboration, and T. Delahaye, M. Fornasa, E. Komatsu, F. Prada, J. Zavala. arXiv:1303.2154 [astro-ph.HE] *Accepted for publication in Nuclear Instruments and Methods in Physics Research A.*

Proceedings of the 4th International Fermi Symposium, 28 Oct - 2 Nov 2012, Monterey, California, USA. Proceedings of RICAP 2013, Roma International Conference on Astro-Particle physics, May 22 - 24, 2013, Rome, Italy.

3. Observations of γ-Ray Emission from the Moon

A. Abdo *et al.* [*Fermi LAT Collaboration*], *Astrophys. J.* **758** *(2012) 140*

4. Anisotropies in the diffuse gamma-ray background measured by the *Fermi* LAT

M. Ackermann *et al.* [*Fermi LAT Collaboration*], *Phys. Rev. D* **85** *(2012) 083007*

5. CLUES on *Fermi*-LAT prospects for the extragalactic detection of $\mu\nu$SSM gravitino Dark Matter

G. A. Gomez-Vargas, M. Fornasa, F. Zandanel, A. J. Cuesta, C. Munoz, F. Prada, G. Yepes, *JCAP* **1202** *(2012) 001*

6. Measurement of anisotropies in the large-scale diffuse gamma-ray emission

G. A. Gomez-Vargas, for the *Fermi*-LAT collaboration, and E. Komatsu, Proceedings of the 8th Workshop on Science with the New Generation of High Energy Gamma-ray Experiments, SciNeGHE 2010, Sept. 8-10, Trieste, Italy. *Nuovo Cim. C* **034N3** *(2011) 327*

Pre-prints

7. The First *Fermi*-LAT Catalog of Sources Above 10 GeV

M. Ackermann *et al.* [*Fermi LAT Collaboration*], *Submitted to Astrophysical Journal Supplement Series,* arXiv:1306.6772 [astro-ph.IM]

8. Search for Gamma-ray Spectral Lines with the Fermi Large Area Telescope and Dark Matter Implications

M. Ackermann *et al.* [*Fermi LAT Collaboration*], *Submitted to Phys. Rev. D,* arXiv:1305.5597 [astro-ph.HE]

Papers in preparation

9. Dark Matter implications of *Fermi*-LAT measurement of anisotropies in the diffuse gamma-ray background

A. Cuoco, *G. A. Gomez-Vargas*, L. Latronico T. Linden, A. Morselli, M.A. Sanchez-Conde, J.M. Siegal-Gaskins, V. Vitale for the *Fermi*-LAT collaboration, and T. Delahaye, M. Fornasa, C. Frenk, E. Komatsu, F. Prada, M. Vogelsberger, J. Zavala, *Preliminary results already presented in the 4th International Fermi Symposium, 28 Oct - 2 Nov 2012, Monterey, California, USA*

10. Searching for sub-GeV Gamma-ray Lines from $\mu\nu$SSM Gravitino Dark Matter with *Fermi*-LAT Data

G. A. Gomez-Vargas, M. Grefe, A. Morselli, C. Munoz, C. Weniger, et al., *Project approved by the Fermi-LAT Publication Board*

11. High concentration NFW profiles in simulated L* galaxies and the effect on rotation curve shapes

C. B. Brook, A. Di Cintio, A. V. Maccio, G. S. Stinson, A. Dutton, *G. A. Gomez-Vargas. To be submitted to Mon. Not. R. Astron. Soc.*

CHAPTER 2

Dark matter shapes the universe

The moral of this section is the unity of the universe.
Robert H. Dicke & Jim Peebles, *Gravitation and Space Science*.

Contents

2.1 Dark matter halos 9
2.1.1 Extragalactic distribution 11
2.1.2 Milky Way's halo density profile 13
2.2 The WIMP scenario 16
2.2.1 Gamma-ray flux from WIMP annihilation 18
2.3 The $\mu\nu$SSM and gravitino dark matter 22
2.3.1 Gamma-rays from gravitino decay in the $\mu\nu$SSM 24

The large scale structure of the universe as seeing today has two challenging puzzles, its origin and evolution. The solution to these problems will help to understand the epoch of galaxy formation, the clustering in galaxy distribution, the amplitude and form of anisotropies in the CMB. The leading idea in structure formation theories is that the origin of structures are quantum fluctuations in the primeval fireball. The evolution of these quantum seeds to form galaxies, groups and clusters of galaxies and the cosmic web of filaments needs to be speed up by the inclusion of an enormous dark source of gravity that indeed constitutes the skeleton of cosmic structures. In this chapter we review results of N-body simulations of extragalactic and galactic DM structures in order to predict their distribution on the sky. Then, we discus some of the exotic particle candidates to DM and the way how they produce gamma-ray signatures that could be detected by the *Fermi*-LAT. Therefore the aim of this chapter is to discuss the connection between structure evolution and the DM fundamental nature.

2.1 Dark matter halos

Jim Peebles in late 1960s simulated the movement of galaxies under the influence of gravitational forces in order to understand their clustering. For today's stan-

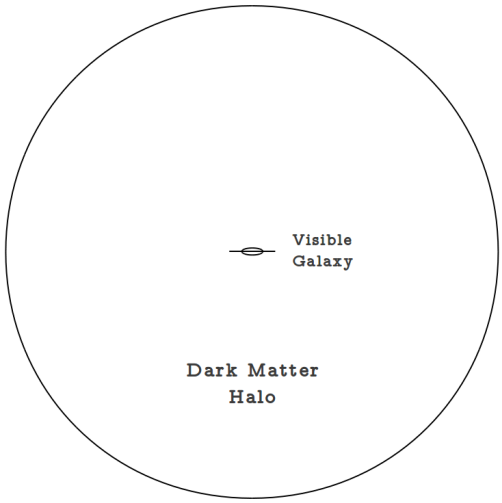

Figure 2.1: Galaxy embedded into a DM halo

dards that was a very poor N-body simulation with only 300 objects, the important result was that galaxies not only follow the Hubble flow, but they also move under the influence of their mutual gravitational attractions until finally fall back on themselves. Peebles concluded that in order to understand the evolution of the universe their components must no longer be treated as individual lonely objects but as members of a complex interacting system. That first N-body simulation was made during a Peebles' summer visit to Los Alamos Scientific Laboratory. When he went back to Princeton he worked further on his simulations, now with up to 2000 objects, confirming the initial results. Simultaneously, Jeremiah Ostriker, also at Princeton, was trying to understand the Milky Way formation but without much success. He was able to see easily using his models that the Milky Way should have become bar-shaped or broken up into two galaxies after one rotation. The problem was that our galaxy is old enough to have completed too many rotations. Ostriker approached Peebles and showed his strange results. After that they started a set of N-body simulations trying to replicate the Milky Way. In their first simulations the galaxies wobbled catastrophically during their first 200-million-year rotation. Nevertheless, Ostriker and Peebles knew that if they added more matter they could generate enough gravity to stabilize and hold the galaxy together. They added a large halo of some material that telescopes couldn't see but that had to be there (see figure 2.1), and the computer finally produced pictures of a galaxy as the Milky Way [34]. Those simulations including a huge DM halo suggested that there is more mass in the universe than accounted for, and this brought them back to the "missing mass" problem pointed out by Fritz Zwicky 40 years earlier. The Zwicky's study was on galaxies in clusters as Coma, as we discussed in the

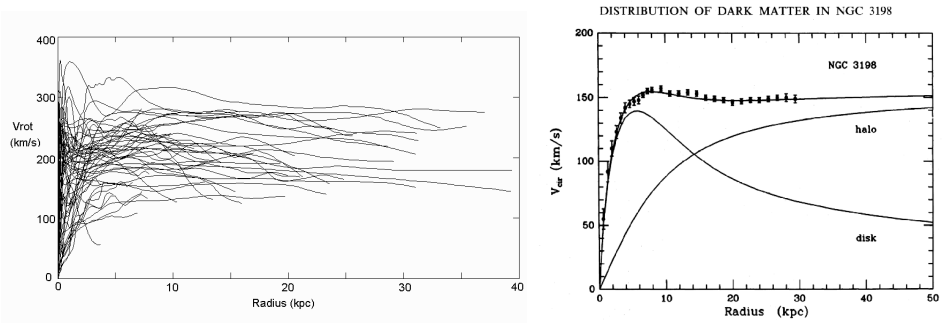

Figure 2.2: Left: Rotation curves of spiral galaxies [35]. Right: Rotation curve of the spiral galaxy NGC3198 explained with the embedding of the galaxy in a gigantic DM halo.

prologue, but Ostriker and Peebles were studying a single galaxy evolution. It was Vera Rubin's velocity curves (see a complete review in [7]) what provided observational support to the Ostriker-Peebles idea of galaxies embedded in huge DM halos (see figure 2.1). The argument is as follows: in a rotating galaxy with mass $M(r)$ inside the galactocentric radius r where the circular velocity is v, the condition for stability is that the centrifugal acceleration v^2/r should be equal to the gravitational pull $GM(r)/r^2$, thus we can get the radial dependence of v:

$$v^2 = \frac{GM(r)}{r}, \tag{2.1}$$

in this way the rotation curves of spiral galaxies can be explained if $M(r)$ split in two components, one visible that decrease with r and other dark proportional to r, thus fitting the Ostriker-Peebles picture of galaxies embedded in enormous DM halos (see figure 2.2). Although the ΛCDM model can explain observations, and brilliant ideas on the nature of DM had been proposed, only a clear indication from direct and indirect DM searches can guide us to a final cosmological model [36].

2.1.1 Extragalactic distribution

In the ΛCDM structure formation, DM clumps to form halos where galaxies are created via complex baryonic physics. DM halos distribute in the universe to assemble voids, walls, and filaments; statistical description of these objects is in impressive agreement with the large scale distribution of galaxies, see figure 2.3.

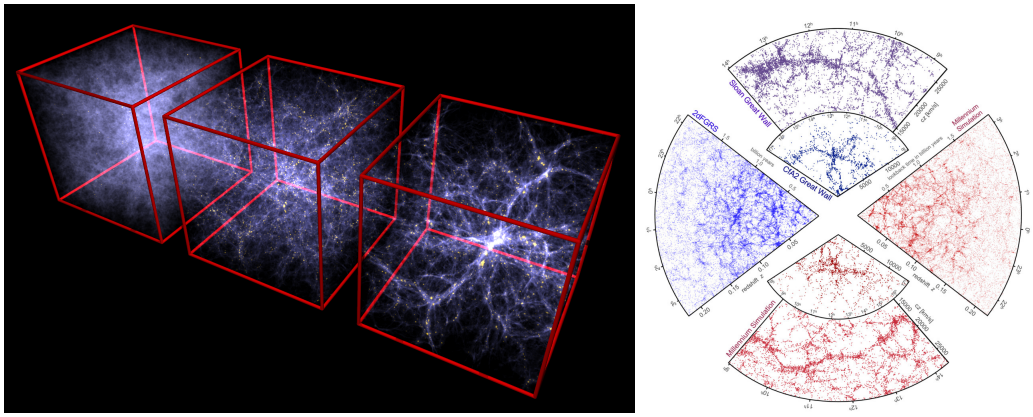

Figure 2.3: Left: A Millenium simulation run in a box of size 100 Mpc h^{-1} with matched sides. Here three snapshot at $z = 6$, $z = 2$, and $z = 0$ from left to right respectively, are shown [Picture credits V. Springel]. Right: Large scale structure from observations (in blue and violet) and numerical simulations (in red and burgundy). One can see voids, walls, and filaments. These are the constituents of the cosmic web. [Picture credits V. Springel, C. S. Frenk and S. D. M. White [38]]

Millennium-II simulation

The Millennium-II simulation (MS-II) [37] traces the formation and evolution of DM structures at cosmological scale. The MS-II follows 2160^3 particles within a comoving cube of 100 Mpc h^{-1} on a side. Each simulation particle represents $m_{res} = 6.885 \times 10^6\ h^{-1} M_\odot$. This mass resolution allows to resolve galaxies as the Milky Way's dwarf spheroidals with about 20 particles and Milky Way-mass galaxies with hundreds of thousands of particles. The MS-II simulation reproduces and improves the results of the first Millennium simulation giving at large scales a distribution remarkable compatible with the structures observed (see the right panel of figure 2.3). At low scales MS-II allows to resolve the granulated structure of halos, i.e. subhalos with masses above few times m_{res} that are hosted by main halos, see figure 2.4. The Friend-Of-Friends (FOF) halo and subhalo catalogs are products of the simulation what provide a tool to study different aspects of structures in the universe as, for instance, their anisotropic distribution.

CLUES simulations

CLUES (Constrained Local UniversE Simulations) N-body simulations[1] aim at describing the formation and evolution of DM halos in a way to reproduce, as precise as possible, our Local Universe. To this goal, constrained initial conditions

[1] http://www.clues-project.org

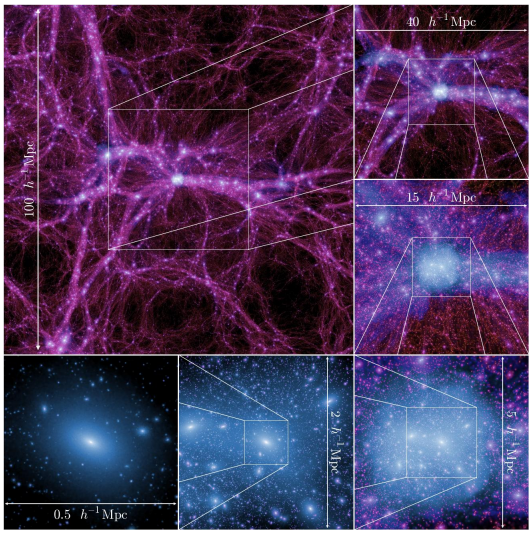

Figure 2.4: A sequential zoom through the Millennium-II Simulation. The large image (upper left) is a 15 Mpc h^{-1} thick slice through the full 100 Mpc h^{-1} simulation box at redshift zero, centered on the most massive halo in the simulation. This halo has a mass similar to the Coma cluster mass, is composed of 119.5 million particles, and contains approximately 36,000 resolved subhalos spanning 6.7 decades in mass. Starting from the upper right and moving clockwise, subsequent panels zoom into the cluster region and show slices that are 40, 15, 5, 2, and 0.5 Mpc h^{-1} on a side (with thicknesses of 10, 6, 5, 2, and 0.5 Mpc h^{-1}). Even at 0.5 Mpc h^{-1}, which is approximately 1/10th the diameter of the halo, a rich variety of substructure is visible.

are set up using the information from radial and peculiar velocities of galaxies from astrophysical catalogs, together with the determination of the masses of the galaxy clusters detected in X-rays [39, 40]. In particular, the characteristics of the most massive clusters such as Virgo, Coma and Perseus, together with the Great Attractor, are well reproduced compared to the real objects, apart from a typical mismatch around 5 Mpc h^{-1} in their position, see figure 2.5.

2.1.2 Milky Way's halo density profile

Cosmological N-body simulations provide important results regarding the expected DM density in our Galaxy. Simulations suggest the existence of a universal DM density profile, valid for all masses and cosmological epochs. It is convenient to use the following parametrization for the DM halo density [41], which covers different

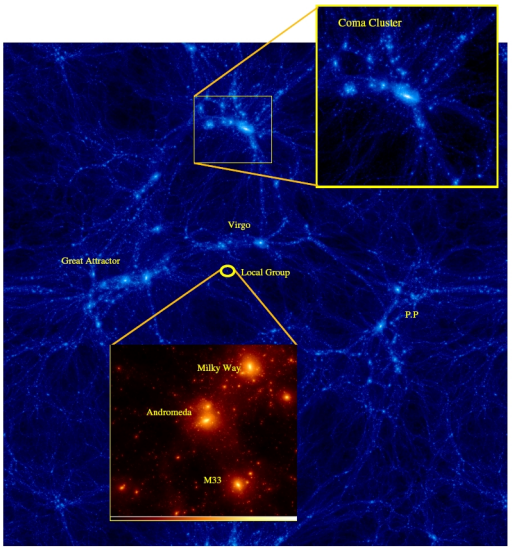

Figure 2.5: Large scale dark matter density distribution in a CLUES simulation. The image covers the full box range of 160 Mpc h^{-1}. Several objects of the real universe are identified: the circle shows the position of our Local Group, a blown up panel shows the detailed structure of the simulated Local Group. The resolution of this small region of 2 Mpc h^{-1} radius is equivalent to having a total of 4096^3 (70 billion) particles in the whole box, which translates in a dynamical range of more than 106.

approximations for DM density:

$$\rho(r) = \frac{\rho_s}{\left(\frac{r}{r_s}\right)^{\gamma}\left[1+\left(\frac{r}{r_s}\right)^{\alpha}\right]^{\frac{\beta-\gamma}{\alpha}}}\,, \tag{2.2}$$

where ρ_s and r_s represent a characteristic density and a scale radius, respectively. The NFW density profile [42, 43], with $(\alpha,\beta,\gamma) = (1,3,1)$, is by far the most widely used in the literature. Another approximation is the so-called Einasto profile [44, 45]

$$\rho_{\rm Ein}(r) = \rho_s \exp\left\{-\frac{2}{\alpha}\left[\left(\frac{r}{r_s}\right)^{\alpha} - 1\right]\right\}\,, \tag{2.3}$$

which provides a better fit than NFW to numerical results [45, 46]. Finally, it is important to keep in mind that DM density profiles can possess a core at the center. With the purely phenomenologically motivated Burkert profile [47] cores can be parametrized:

$$\rho_{\rm Burkert}(r) = \frac{\rho_s\, r_s^3}{(r+r_s)\,(r^2+r_s^2)}\,, \tag{2.4}$$

where the scale radius r_s is the size of the core.

Early results on the central slopes of the DM profiles showed some significant disagreement between the estimates, with values ranging from $\gamma = 1.5$ [48] to $\gamma = 1$ [42, 43]. As the accuracy of the simulations improved, the disagreement became smaller. For the Via Lactea II (VLII) simulation the slope in Ref. [49] was estimated to be $\gamma = 1.24$. A re-analysis of the VLII simulation and new simulations performed by the same group give the slope $\gamma = 0.8 - 1.0$ [50], which is consistent with the Aquarius simulation [51]. Another improvement comes from the fact that the simulations now resolve the cusp down to a radius of ~ 100 pc, which means that less extrapolation is required for the density of the central region.

Yet, there is an additional ingredient that is expected to play a prominent role in the centers of DM halos: baryons. Although only a very small fraction of the total matter content in the Universe is due to baryons, they represent the dominant component at the very centers of galaxies like the Milky Way. Actually, the fact that current N-body simulations do not resolve the innermost regions of the halos, is a minor consideration relative to the uncertainties due to the interplay between baryons and DM.

The baryons lose energy through radiative processes and fall into the central regions of a forming galaxy. As a consequence of this redistribution of mass, the resulting gravitational potential is deeper, and the DM must move closer to the center, increasing its density. This *compression* of DM halos due to baryonic infall was first studied in Ref. [52] for a spherically symmetric DM halo using simple simulations and adiabatic invariants. A convenient analytical approximation was provided in Ref. [53]. The model was later modified [54] to account for the eccentricity of orbits of DM particles. The effect seems to be confirmed by recent hydrodynamic simulations (see e.g. Refs. [55, 56, 57, 58, 59, 60].). In Ref. [58], for instance, the authors ran a set of high-resolution hydrodynamic simulations that self-consistently included complex baryonic physics such as gas dissipation, star formation and supernova feedback. They all showed a clear steepening of the inner DM density profiles with respect to DM-only simulations. Indeed, it is argued by the authors that such effect should be always included in order to correctly model the mass distribution in galaxies and galaxy clusters.

As pointed out in Ref. [61], the effect of the baryonic adiabatic compression might be crucial for indirect DM searches, as it increases by several orders of magnitude the gamma-ray flux from DM annihilation in the inner regions, and therefore the DM detectability. In Ref. [62], this effect was used to study the detection of supersymmetric DM by the *Fermi*-LAT, with the conclusion that fluxes from the GC would be largely reachable in significant regions of the supersymmetric parameter space. The effect of compression on galaxy clusters was recently studied in Ref. [63].

There is however another possible effect related to baryons that tends to de-

crease the DM density and flatten the DM cusp [64, 65, 66]. The mechanism relies on numerous episodes of baryon infall followed by a strong burst of star formation, which expels the baryons. At the beginning of each episode the baryons dominate the gravitational potential. The DM contracts to respond to the changed potential. A sudden onset of star formation drives the baryons out. The DM also moves out because of the shallower potential. Each episode produces a relatively small effect on the DM, but a large number of them results in a significant decline of the DM density. Indeed, cosmological simulations that implement this process show a strong decline of the DM density [67, 68]. Whether the process happens in reality is still unclear. Simulations with the cycles of infall-burst-expansion process require that the gas during the burst stage does not lose energy through radiation, which is not realistic. Still, the strong energy release needed by the mechanism may be provided by other processes and the flattening of the DM cusp may occur. If this happened to our Galaxy, then the DM density within the central $\sim$ 500 pc may become constant [68]. We note that this mechanism would wipe out the DM cusp also in centers of dwarf galaxies [67]. Yet, a recent work that also includes stellar feedback offers a much more complicated picture in which galaxies may retain or not their DM cusps depending on the ratio between their stellar-to-halo masses [69].

2.2 The WIMP scenario

A large variety of particle DM candidates can be labeled as Weakly Interactive Massive Particles (WIMPs). In WIMP models the observed abundance of DM is connected (via thermal decoupling and cosmology) to its particle nature throughout the so-called *WIMP miracle*. In the following we review this connection based in the references [14, 79]. Let us assume that DM particles today are thermal relics of the Early Universe, using the Boltzmann equation we can track the DM number density, n:

$$\hat{L}[f] = \hat{C}[f], \tag{2.5}$$

with $\hat{L}$ the Liouville operator that model the change in time of the phase space density, $f = f(\vec{p}, \vec{x}, t)$, and $\hat{C}$ the collision operator that describe the number of particles per phase-space volume lost or gained per unit time. In a Friedman-Lemaître-Robertson-Walker universe, i.e. imposing homogeneity and isotropy, $f(\vec{p}, \vec{x}, t)$ does not depends on direction, and moments in all directions are equally distributed, therefore $f(\vec{p}, \vec{x}, t) = f(E, t)$. The Liouville operator working on $f(E, t)$ integrated over momentum space reads

$$\int \hat{L}[f] \cdot g \frac{\mathrm{d}^3 p}{(2\pi)^3} = \frac{\mathrm{d}n}{\mathrm{d}t} + 3H \cdot n, \tag{2.6}$$

with g the number of spin degrees of freedom and H is Hubble constant. This result can be easily understood. The first term describes the number density of particles varying in time and the second one gives the dilution of particles due to the universe's expansion. For the right hand side of equation 2.5 we consider two DM particles annihilating to a SM pair, $DM_1 + DM_2 = q_3 + q_4$, thus the momentum space integrated collision term applied to the phase space of the DM_1 particles $f_1(E,t)$ reads

$$g_1 \int \hat{C}[f_1] \frac{\mathrm{d}^3 p}{(2\pi)^3} = -\langle \sigma v \rangle \, (n_{DM_1} n_{DM_2} - n^{eq}_{DM_1} n^{eq}_{DM_2}), \tag{2.7}$$

where $\langle \sigma v \rangle$ is the annihilation cross-section averaged over the velocity distribution of the DM particles, and $n^{eq}_{DM_i}$ is the number density of the particle DM_i at thermal equilibrium. Assuming self-conjugated DM particles $DM_1 = DM_2 = DM$ the Boltzmann equation can be expressed as

$$\frac{\mathrm{d}n_{DM}}{\mathrm{d}t} + 3H \cdot n_{DM} = -\langle \sigma v \rangle \, (n^2_{DM} - (n^{eq}_{DM})^2). \tag{2.8}$$

We next introduce the variables: $Y = n_{DM}/s$ and $Y^{eq} = n^{eq}_{DM}/s$, with s the entropy density. In a comoving volume (sa^3 = constant) the entropy keeps constant and $\dot{n}_{DM} + 3Hn_{DM} = s\dot{Y}$, thus the particle dilution term disappear introducing the variable Y. Now the equation 2.8 reads

$$s\dot{Y} = -\langle \sigma v \rangle \, s^2 (Y^2 - (Y^{eq})^2). \tag{2.9}$$

Figure 2.6 shows the solution of Y as function of the quantity $x = m_{DM}/T$ with m_{DM} the DM mass and T the universe's temperature. In the Early Universe at high temperature the DM interaction rate $\Gamma \approx n_{DM} \langle \sigma v \rangle$ is larger than the expansion rate of the universe H, and DM particles are producing and disappearing all the time, in other words, DM is coupled to the primaeval plasma. The universe expands cooling down, increasing x, and at some point $\Gamma \approx H$, there are not enough energy in the plasma to keep DM coupled and the quantity Y "freeze out". If no entropy is produced $Y_{\text{today}} = Y_{\text{freeze out}}$, therefore $n_{DM\text{today}} = s_{\text{today}} \cdot Y_{\text{freeze out}}$. In figure 2.6 we can see that the freeze out point for Y depends on $\langle \sigma v \rangle$, the more interaction between DM and SM particles, the lower DM particle density today. This density has been infered from many observations including the CMB anisotropies by WMAP and PLANK satellites, which gives:

$$\Omega_{DM} h^2 = \frac{m_{DM} n_{DM\text{today}}}{\rho_c} h^2 \approx 0.1, \tag{2.10}$$

with $h = H/100$, $\rho_c = 3H^2/8\pi G$ the universe's critical density. Assuming m_{DM} in the GeV range, one gets:

$$\Omega_{DM} h^2 \approx \frac{3 \times 10^{-27} \mathrm{cm}^3/\mathrm{s}}{\langle \sigma v \rangle}. \tag{2.11}$$

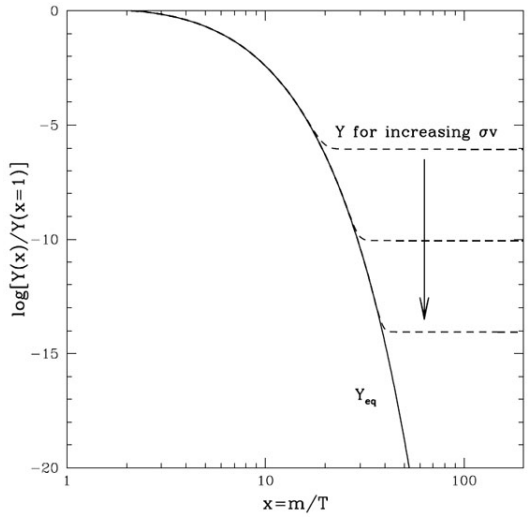

Figure 2.6: Y as function $x = m_{DM}/T$. The quantity x is proportional to time, as the universe expands its temperature drops, thus x increase with cosmological time.

The WIMP miracle is that an electroweak interaction between DM and SM particles of $\langle\sigma v\rangle \approx 3 \times 10^{-26}$ cm^3/s, naturally produce $\Omega_{DM}h^2 \approx 0.1$.

2.2.1 Gamma-ray flux from WIMP annihilation

If DM relic particles annihilate to SM ones some gamma rays can be produced, as we discuss in the following. In the Galactic halo, the gamma-ray flux from DM annihilation has two main contributions [80]: prompt photons and photons induced via Inverse Compton Scattering (ICS). The former are produced indirectly through hadronization, fragmentation and decays of the DM annihilation products or by internal bremsstrahlung, or directly through one-loop processes (but these are typically suppressed in most DM models). The second contribution originates from electrons and positrons produced in DM annihilations, via ICS off the ambient photon background. The other two possible contributions to the gamma-ray flux from DM annihilation can be neglected in our analysis: radiation from bremsstrahlung is expected to be sub-dominant with respect to ICS in the energy range considered (1 - 100 GeV) and a few degrees off the Galactic plane (see Fig. 14 in Ref. [81]), and synchrotron radiation is only relevant at radio frequencies, below the *Fermi*-LAT threshold. Thus the gamma-ray differential flux from DM annihilation from a given observational region $\Delta\Omega$ in the Galactic halo can be written as follows:

$$\frac{d\Phi_\gamma}{dE_\gamma}(E_\gamma, \Delta\Omega) = \left(\frac{d\Phi_\gamma}{dE_\gamma}\right)_{prompt} + \left(\frac{d\Phi_\gamma}{dE_\gamma}\right)_{ICS} . \tag{2.12}$$

We discuss in detail both components below. It is worth mentioning that in some models pairs of WIMPs can also annihilate to a photon (γ) and a second particle (X), for example, $\gamma\gamma$, γZ boson, or γ Higgs, producing monochromatic gamma rays. DM particles do not couple directly to photons since DM is strongly constrained to be electrically neutral. Therefore, sharp features due to the process $DM + DM \rightarrow \gamma + X$ are loop suppressed. The rest frame-energy of the line produced in WIMP annihilations to γX reads

$$E_\gamma = m_{DM}\left(1 - \frac{m_X^2}{4m_{DM}^2}\right). \tag{2.13}$$

In the case of WIMP annihilating to two photons, the line appears at the mass of the WIMP particle.

Prompt gamma rays

A continuous spectrum of gamma rays is produced mainly by the decays of π^0's generated in the cascading of annihilation products and also by internal bremsstrahlung. While the former process is completely determined for each given final state of annihilation (the standard channels used in literature are $b\bar{b}$, $\tau^+\tau^-$, $\mu^+\mu^-$ and W^+W^-), the latter depends in general on the details of the DM model such as the DM particle spin and the properties of the mediating particle. Nevertheless, it is known that internal bremsstrahlung always includes much model-independent final state radiation (FSR), which is emitted directly from charged particles in the external legs [82, 83]. In analysis of generic DM models, only these FSR model-independent components of the internal bremsstrahlung are considered. It is a safe choice for conservative approaches, since the inclusion of model-dependent emission from virtual charged mediators would increase the amount of photons generated in annihilations making constraints only stronger [83, 26].

As we will consider throughout this thesis the case of self-conjugated DM particles, the prompt contribution can be written as

$$\left(\frac{d\Phi_\gamma}{dE_\gamma}\right)_{prompt} = \sum_i \frac{dN_\gamma^i}{dE_\gamma}\,\frac{\langle\sigma_i v\rangle}{8\pi m_{DM}^2}\,\bar{J}(\Delta\Omega)\Delta\Omega\,. \tag{2.14}$$

This equation has to be multiplied by an additional factor of $1/2$ if the DM particle studied is not its own anti-particle. The discrete sum is over all DM annihilation channels. dN_γ^i/dE_γ is the differential gamma-ray yield[2], the quantity $\bar{J}(\Delta\Omega)$ (commonly known as the *J-factor*) is defined as

$$\bar{J}(\Delta\Omega) \equiv \frac{1}{\Delta\Omega}\int d\Omega \int_{l.o.s.} \rho^2(r(l,\Psi))\,dl\,. \tag{2.15}$$

[2] For the spectra of gamma rays we use pre-evaluated tables in [86], which are generated using `PYTHIA` [87] and thus containing FSR properly.

The J-factor accounts for both the DM distribution and the geometry of the system[3]. The integral of the square of the DM density ρ^2 in the direction of observation Ψ is along the line of sight (*l.o.s*), and r and l represent the galactocentric distance and the distance to the Earth, respectively. Indeed, in Eq. (2.14), all the dependence on astrophysical parameters is encoded in the J-factor itself, whereas the rest of the terms encode the particle physics input[4]. The most crucial aspect in the calculation of $\bar{J}(\Delta\Omega)\Delta\Omega$ is related to the modeling of the DM distribution in the GC.

Gamma rays from Inverse Compton Scattering

Electron and positron ($e^{\pm}$) fluxes are generated in DM annihilations mainly through the hadronization, fragmentation and decays of the annihilation products, since direct production of e^+e^- is supressed by small couplings in most DM models. These $e^{\pm}$ propagate in the Galaxy and produce high-energy gamma rays via ICS off the ambient photon background. The differential flux produced by ICS from a given observational region $\Delta\Omega$ in the Galactic halo is given by [86]

$$\frac{d\Phi_\gamma^{ICS}}{dE_\gamma} = \sum_i \frac{\langle\sigma_i v\rangle}{8\pi m_{DM}^2} \int_{m_e}^{m_{DM}} \frac{dE_I}{E_\gamma} \frac{dN_{e^\pm}^i}{dE_e}(E_I) \int d\Omega \, \frac{I_{IC}(E_\gamma, E_I; \Psi)}{E_\gamma} \,, \quad (2.16)$$

where E_I is the $e^{\pm}$ injection energy, Ψ corresponds to the angular position where the ICS gamma rays are produced, and the function $I_{IC}(E_\gamma, E_I; \Psi)$ is given by

$$I_{IC}(E_\gamma, E_I; \Psi) = 2E_\gamma \int_{l.o.s.} dl \int_{m_e}^{E_I} dE_e \, \frac{P_{IC}(E_\gamma, E_e; \mathbf{x})}{b_T(E_e; \mathbf{x})} \, \tilde{I}(E_e, E_I; \mathbf{x}) \,. \quad (2.17)$$

Here $\mathbf{x} = (l, \Psi)$ and $b_T \propto E^2$ is the energy-loss rate of the electron in the Thomson limit. The function P_{IC} is the photon emission power for ICS, and it depends on the interstellar radiation (ISR) densities for each of the species composing the photon background. It is known that the ISR in the inner Galactic region can be well modeled as a sum of separate black body radiation components corresponding to star-light (SL), infrared radiation (IR), and cosmic microwave background

[3] Although in principle the point-spread function (PSF) should be included in this formula (see e.g., Refs.[61, 84, 85]), it turns out to be not relevant in our study mainly for two reasons: i) we deal with fluxes integrated in large regions of the sky, much larger than the PSF, and ii) we avoid the very center of the Galaxy, where the PSF would artificially smear out the cusps expected from some of the DM density profiles.

[4] Strictly speaking, both terms are not completely independent of each other, as the minimum predicted mass for DM halos is set by the properties of the DM particle and is expected to play an important role also in the J-factor when substructures are taken into account. Here, we do not consider the effect of substructures on the annihilation flux, as large substructure boosts are only expected for the outskirts of DM halos [88, 89], and thus they should have a very small impact on inner Galaxy studies.

(CMB) [91]. In this work we have used the interstellar radiation field provided by GALPROP [92] to calculate the normalization and the temperature for each of these three components. For the injection spectra of $e^{\pm}$, we utilize pre-evaluated tables in [86].

The last ingredient in Eq. (2.17) is the $\tilde{I}(E_e, E_I; \mathbf{x})$ function, which can be given in terms of the well- known halo function [86],

$$I(E, E_I; \mathbf{x}) = \tilde{I}(E, E_I; \mathbf{x})[(b_T(E)/b(E, \mathbf{x}))(\rho(\mathbf{x})/\rho_\odot)^2]^{-1}, \tag{2.18}$$

where $\rho_\odot$ is the DM density at Sun's position and $b(E, \mathbf{x})$ encodes the energy loss of the $e^{\pm}$. The $\tilde{I}(E_e, E_I; \mathbf{x})$ function obeys the diffusion loss equation [86],

$$\nabla^2 \tilde{I}(E_e, E_I; \mathbf{x}) + \frac{E_e^2}{K(E_e; \mathbf{x})} \frac{\partial}{\partial E_e} \left[\frac{b(E_e; \mathbf{x})}{E_e^2} \tilde{I}(E_e, E_I; \mathbf{x}) \right] = 0 \,, \tag{2.19}$$

and is commonly solved by modeling the diffusion region as a cylinder with radius $R_{\rm max}$ =20 kpc, height z equal to $2L$ and vanishing boundary conditions. Also the diffusion coefficient $K(E; \mathbf{x})$ has been taken as homogeneous inside the cylinder with an energy dependence following a power law $K(E) = K_0(E/1\text{GeV})^\delta$. For these three parameters L, K_0 and δ, the so called diffusion coefficient, we have adopted three sets referred to as MIN, MED and MAX models [93], which account for the degeneracy given by the local observations of the cosmic rays at the Earth including the boron to carbon ratio, B/C [94]. We take them as our benchmark points, although we note that MIN and MAX models do not imply minimal or maximal expected gamma-ray signal, respectively. To solve this equation under the described conditions, we have used BoxLib [95] which is a general purpose partial differential equation solver with an adaptive mesh refinement method.

Let us finally remark about the importance of the energy loss function $b(E; \mathbf{x})$. The two main energy loss mechanisms of $e^{\pm}$ in the Galaxy are the ICS and synchrotron radiation produced by interaction with the Galactic magnetic field. The former is the only contribution to the energy losses that is usually considered, since it is the most important one in studies of sources far from the GC. But when the $e^{\pm}$ energy reaches several hundreds of GeV, synchrotron radiation can dominate the energy loss rate due to the suppression factor in the ICS contribution in the Klein-Nishina regime. By contrast, synchrotron radiation losses do not have this suppression, and are driven by the magnetic field energy density $u_B(\mathbf{x}) = B^2/2$. Although the strength and exact shape of the Galactic magnetic field is not well known, in the literature it is broadly described by the from [86],

$$B(r, z) = B_0 \exp\left(-\frac{r - 8.5 \text{ kpc}}{10 \text{ kpc}} - \frac{z}{2 \text{ kpc}} \right) , \tag{2.20}$$

normalized with the strength of the magnetic field around the solar system, B_0, which is known to be in the range of 1 to 10 μG [92]. This field grows towards the

GC and therefore one should expect that the energy losses are dominated by synchrotron radiation in the inner part of the galaxy [86]. On the other hand, we can expect that when the magnetic field is stronger, the energy of the injected $e^{\pm}$ is more efficiently liberated in the form of synchrotron emission resulting in a softer spectrum, and producing therefore smaller constraints on the DM annihilation cross-section. The ICS effect becomes relevant only for the $\mu^+\mu^-$ annihilation channel, since the contribution of the prompt gamma rays is less important than in other channels with hadronic decays.

2.3 The $\mu\nu$SSM and gravitino dark matter

One of the most attractive theories for physics BSM is supersymmetry, which not only solves theoretical problems of the Standard Model, but also has spectacular experimental implications, with signatures expected to be found at the LHC.

There is no unique supersymmetric model, and in fact several of them have been proposed in the literature with interesting properties [96], and implying different candidates for DM. The most popular one is the Minimal Supersymmetric Standard Model (MSSM) [97], where the lightest neutralino is a viable DM candidate once R-parity conservation is imposed. However, the MSSM has the so-called μ-problem [98] arising from the requirement of a supersymmetric mass term for the Higgs bosons in the superpotential, $\mu\hat{H}_u\hat{H}_d$, necessary e.g. to generate Higgsino masses in order to fulfill the current experimental bounds on chargino masses implying $\mu > 100\,\text{GeV}$. In the presence of a GUT and/or a gravitational theory with typical scales 10^{16} and $10^{19}\,\text{GeV}$, respectively, one should be able to explain how to obtain such a supersymmetric mass term μ of the order of only 1 TeV.

The "μ from ν" Supersymmetric Standard Model ($\mu\nu$SSM) [23, 24, 99, 100, 101] provides a solution to the μ-problem. The superpotential of the $\mu\nu$SSM contains, in addition to the usual Yukawa terms for quarks and charged leptons of the MSSM, Yukawa terms for neutrinos $Y_{\nu_{ij}}\hat{H}_u\,\hat{L}_i\,\hat{\nu}^c_j$, and terms of the type $\lambda_i\hat{\nu}^c_i\hat{H}_d\hat{H}_u$ and $\kappa_{ijk}\hat{\nu}^c_i\hat{\nu}^c_j\hat{\nu}^c_k$. The mixing terms between the three right-handed neutrinos ν^c_i and the two Higgs doublets H_u, H_d, produce precisely an effective μ-term through electroweak-scale right-handed sneutrino vacuum expectation values (VEVs), $\mu \equiv \lambda_i\langle\tilde{\nu}^c_i\rangle$. This solves the μ-problem without having to introduce an extra singlet superfield as in the case of the Next-to-MSSM (NMSSM) [102]. The mixing terms among right-handed neutrinos avoid the existence of a Goldstone boson and contribute to generate effective Majorana masses for neutrinos at the electroweak scale $\sim \kappa\langle\tilde{\nu}^c\rangle$. Because of the explicit breaking of R-parity by the above three terms, the neutralino is no longer a candidate for DM in this model, but nevertheless the gravitino can be a good substitute as will be discussed below.

In addition, the breaking of R-parity produces a mixing of the neutralinos with

the left- and right-handed neutrinos, and as a consequence a generalized matrix of the seesaw type that gives rise to three light eigenvalues corresponding to neutrino masses at tree level. As shown in [99, 103, 104, 105] current measurements of the neutrino mass differences and mixing angles can be easily reproduced. This dynamically generated electroweak-scale seesaw mechanism also avoids the introduction of *ad-hoc* high energy scales in the model. Thus, in addition to solving the μ-problem, the $\mu\nu$SSM explains at tree level the origin of neutrino masses. We also note here that in the Bilinear R-parity Violation model (BRpV) [106], the bilinear terms $\mu_i \hat{L}_i \hat{H}_u$ induce neutrino masses through the mixing of the left-handed neutrinos $\hat{\nu}_i$ with the neutralinos (one mass at tree level and the other two at one-loop level), without the need of using right-handed neutrino superfields. However, the μ-problem is in fact augmented with the three new bilinear terms, which have to be of the order $\mu_i \lesssim 10^{-4}$ GeV to reproduce current neutrino data.

Given that the $\mu\nu$SSM is a very well motivated and attractive model, its phenomenology at the LHC has been analysed in detail recently [110, 107, 108, 109, 104, 105, 111]. Cosmological issues in this model have also been considered, and in particular the generation of the baryon asymmetry of the Universe was studied in detail [112, 113], with the interesting result that electroweak baryogenesis can be realized [113] while thermal leptogenesis is disfavored in the context of the $\mu\nu$SSM [112]. Extensions of the $\mu\nu$SSM with an extra $U(1)$ gauge symmetry, and the corresponding phenomenology, have been discussed in Ref. [114].

As mentioned above, the three terms characterizing the $\mu\nu$SSM produce an explicit breaking of R-parity.[5] The size of the breaking can be understood if we realize that in the limit where neutrino Yukawa couplings Y_ν are vanishing, the $\hat{\nu}^c$ are just ordinary singlet superfields, without any connection with neutrinos, and this model would coincide (although with three singlets instead of only one) with the NMSSM where R-parity is conserved. Once we switch on Y_ν, the fields $\hat{\nu}^c$ become right-handed neutrinos, and, as a consequence, R-parity is broken. Indeed this breaking is small because, as mentioned above, we have an electroweak-scale seesaw, implying Y_ν no larger than about 10^{-6} (like the electron Yukawa coupling) in order to reproduce neutrino masses smaller than about 10^{-2} eV.

Since R-parity is broken in the $\mu\nu$SSM, the lightest supersymmetric particle (LSP) is no longer stable. Thus, the lightest neutralino, with now very short lifetime, cannot be a candidate for the DM in the Universe anymore. Nevertheless, if the role of the LSP is played by the gravitino, its decay is suppressed both by

[5] One could worry about fast proton decay through the usual baryon and lepton number violating operators of the MSSM. Nevertheless, the choice of R-parity is *ad hoc*. There are other discrete symmetries, like e.g. baryon triality which only forbids the baryon violating operators [115]. Besides, in string constructions the matter superfields can be located in different sectors of the compact space or have different extra $U(1)$ charges, in such a way that some operators violating R-parity can be forbidden while others remain allowed [116, 117].

the feebleness of the gravitational interaction and by the small R-parity violating coupling. As a consequence, its lifetime can be much longer than the age of the Universe and the gravitino can represent a good DM candidate. Besides, as pointed out in Ref. [118] for the case of R-parity violation, the decay of the gravitino produces a monochromatic photon with an energy equal to half of the gravitino mass, and therefore its presence can, in principle, be inferred indirectly from observations of the diffuse photon background.[6]

2.3.1 Gamma-rays from gravitino decay in the $\mu\nu$SSM

In the supergravity Lagrangian an interaction term is predicted between the gravitino, the field strength for the photon, and the photino. Since, due to the breaking of R-parity, the photino and the left-handed neutrinos are mixed, the gravitino will be able to decay through the interaction term into a photon and a neutrino [118]. [7]. The gravitino lifetime $\tau_{3/2}$ results to be:

$$\tau_{3/2} \simeq 3.8 \times 10^{27} \mathrm{s} \left(\frac{|U_{\tilde{\gamma}\nu}|^2}{10^{-16}} \right)^{-1} \left(\frac{m_{3/2}}{10\ \mathrm{GeV}} \right)^{-3}, \tag{2.21}$$

where $|U_{\tilde{\gamma}\nu}|^2$ is the photino content of the neutrino, and is constrained to be $|U_{\tilde{\gamma}\nu}|^2 \sim 10^{-16} - 10^{-12}$ in the $\mu\nu$SSM, in order to reproduce neutrino masses [120]. As a consequence, the gravitino will be very long lived. (recall that the lifetime of the Universe is about 10^{17} s). Additionally, adjusting the reheating temperature one can reproduce the correct relic density for each possible value of the gravitino mass (see [120] and references therein).

The detection of DM in several R-parity breaking scenarios has been studied in the literature [118, 121, 120] considering the case of gravitinos emitting gamma-rays when decaying in *i*) the smooth galactic halo, and *ii*) extragalactic regions at cosmological distances.

In *i*), the gamma-ray signal is an anisotropic sharp line and the flux is given by

$$\frac{d\Phi}{dE}(E) = \frac{\delta(E - \frac{m_{3/2}}{2})}{4\pi\tau_{3/2} m_{3/2}} \int_{\mathrm{los}} \rho_{halo}(\vec{l}) d\vec{l}, \tag{2.22}$$

[6] The gravitino decay as well produces a flux monochromatic neutrinos that, in principle, could be observed in neutrino detectors. However, at energies around 1 GeV the signal is expected to be overwhelmed by atmospheric neutrinos and, given the bad neutrino energy resolution, also a spectral analysis is not of much help. Moreover, the effective volume of neutrino detectors in the GeV range is too small to expect a sizeable signal event rate. See Ref. [119] for a related discussion. Thus we concentrate on gamma-ray line searches throughout this work.

[7] Other possible decay modes such as gravitino decay into a $W^{\pm}$ and a charged lepton, or into a Z^0 and a neutrino [**?**] are not relevant in our case, since we will obtain below that a gravitino mass smaller than 20 GeV is convenient in order to fulfill experimental constraints. Neither we consider the possibility that the gravitino might in principle decay to singlet Higgs-neutrino if the Higgs is sufficiently light.

where the halo DM density is integrated along the line of sight l, and we will use a NFW density profile for the Milky Way halo compatible with the latest observational constraints as modeled in [61]. Let us remark, nevertheless, that since the region that we will study below does not include the inner galaxy, any density profile will give rise to similar results.

On the other hand, in *ii*), the photons produced by gravitinos decaying at cosmological distances are red-shifted during their journey to the observer, and we obtain the isotropic extragalactic flux applying the analysis of Refs. [118, 122] to the $\mu\nu$SSM. As can be seen e.g. in Figs. 3 and 4 of Ref. [120], the sharp line produced by the galactic halo dominates over this extragalactic signal.

Finally, for nearby extragalactic structures *iii*), the gamma-ray signal is a monochromatic line similarly to *i*), and Eq. (2.22) can also be used for the computation of the flux. Actually the contribution from the smooth galactic DM halo is practically isotropic in the region around a particular nearby extragalactic structure (at least at high latitudes) and less important than the contribution from the object itself. Moreover at high latitudes, the galactic foreground is smaller than near the galactic center, so that objects with a lower DM-induced gamma-ray flux can potentially be associated to larger prospects of detection than the region near the galactic center. Thus, the study of the extragalactic density field is something worth carrying out. Actually, as the contribution from the smooth galactic halo is practically isotropic in the region around a particular nearby extragalactic structure and less important than the contribution from the structure itself for high galactic latitudes, accounting for the extragalactic density field represents an important ingredient.

Chapter 3

The Fermi-LAT instrument

Antes que nada: ésta no es una novela *de* ciencia-ficción.
Ésta -ésta fue y ésta será- es una novela *con* ciencia-ficción.
Rodrigo Fresán, *El fondo del cielo*.

Contents

3.1 Telescope components 28
3.2 Performance 30
3.3 Science analysis environment 31
3.3.1 Binned likelihood analysis 31

Gamma rays are high energy photons, and therefore high frequency/low wavelength radiation, produced in the most extreme environment of the universe. This radiation is biologically hazardous because typical gamma-ray wavelengths are less than 0.1 nm, lower than the diameter of an atom. Happily for human life, a broad gamma-ray energy band is screened by Earth's atmosphere, thus we must observe the gamma-ray sky from outside the planet by spacecrafts, see the left panel of figure 3.1.

The interaction between gamma rays and matter above few MeVs is dominated by pair production, in other words: a high-energy gamma-ray penetrating a material will transform into a particle-antiparticle pair. For this reason to detect high-energy gamma-rays we need pair conversion telescopes. They consist basically by a tracking system, a calorimeter and an anticoincidence shield to protect the detector from charged particles, see the right panel of figure 3.1. The *Fermi Gamma-ray Space Telescope (Fermi)* in figure 3.2 is a spacecraft launched on June 11, 2008 aboard a Delta II 7920-H rocket. Its main instrument, the Large Area Telescope (LAT) [19], collects high energy gamma rays ($\sim$ 20 MeV to $>$ 300 GeV) with a large effective area ($\sim$ 6200 cm^2 above 1 GeV for P7CLEAN_V6 at normal incidence [30]) and a large field of view (2.4 sr). Gamma rays undergoing the *Fermi*-LAT are converted to electron-positron pairs and the path of the pairs recorded in the thin tungsten foils and silicon layers of the tracker, respectively. The energy of subsequent electromagnetic showers are measured in the telescope's calorimeter.

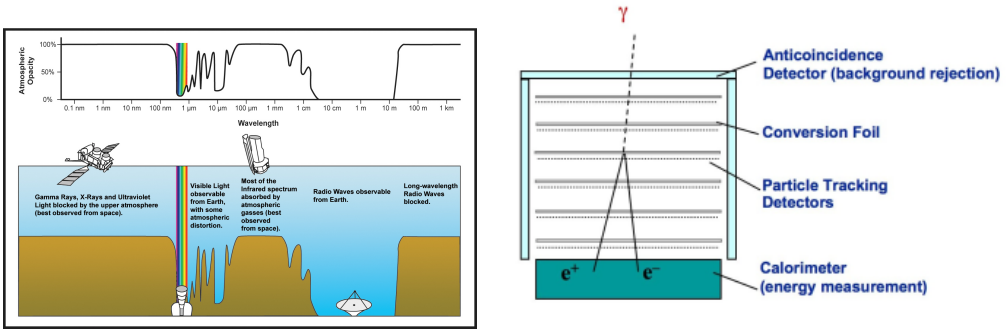

Figure 3.1: Credit: NASA/Aurore Simonnet, Sonoma State University. Left: The Earth's atmosphere is very good at blocking light from outer space coming down to the surface. As a result, from Earth we can see outer space only at very specific wavelength ranges, called 'windows'. Visible light falls within such a window, as do a few infrared wavelength ranges. For gamma-ray band the atmosphere is opaque and spacecraft are needed for its observation. Imaging Air Cherenkov telescopes and shower detectors can observe very high-energy gamma rays using the atmosphere as target. Credit: NASA/IPAC. Right: Unlike visible light, high-energy gamma rays cannot be refracted by a lens or focused by a mirror. Instead, they are detected with the same technology as the detectors used in high-energy particle accelerators. Credit: Fermi-LAT team

The *Fermi* spacecraft orbits the earth in about 96 minutes. It is oriented to point the LAT upward at all time, on alternate orbits *Fermi* rocks to the left and right, allowing the *Fermi*-LAT to cover more of the sky. Thus the whole sky can be surveyed in two orbits.

In this section base on refs. [30, 124] we present the instrument components, and its performance, i.e. the functions relating true variables, as emitted by gamma-ray sources, and measured quantities. Also we give a short introduction to the likelihood analysis. This part is based on three hands-on *Fermi* data schools imparted at the IFT UAM/CSIC Madrid, IFIC UV/CSIC Valencia and the Sexten Center for Astrophysics.

3.1 Telescope components

The *Fermi*-LAT consists of a 4×4 array of modules (37 cm square and 66 cm tall), each consisting of a precision tracker (TRK) and calorimeter (CAL), covered by an anticoincidence detector (ACD) that allows for rejection of charged particles.

TRK The silicon tracker comprising 18 layers of paired $x-y$ Silicon Strip Detector (SSD) planes with interleaved tungsten foils, is the section of the instrument

Figure 3.2: Artistic image of the *Fermi* spacecraft.

where electron-positron conversion of gamma rays ideally take place. The so call FRONT part of the TRK refers to the firs 12 paired layers which are composed of ~ 3% of a radiation length of tungsten. The BACK part is made of 4 layers but the tungsten converters are ~ 6 times thicker. The bottom two layers are dedicated for TRK trigger, they have no converter.

CAL It is a block of 1535 cubic rectangle Thallium-doped Cesium Iodide crystals, showers are absorbed here releasing their energy to the crystals where is measured. Crystals also provide a reasonable 3D imaging combining location of the shower center, from asymmetries in the readout of scintillated light produced by the shower passing through crystals, with the physical location of each crystal. Higher energy events create showers that are not completely contain in the CAL producing a degradation of the energy resolution. The intrinsic 3D imaging capability of the CAL is key to mitigating the that problem at high energy through an event-by-event 3D fit to the shower profile.

ACD This component is for the identification of LAT-entering charged cosmic rays. The ACD consist of 25 scintillating plastic tiles covering the top of the instrument and 16 tiles covering each of the four sides (89 in all). The dimensions of the tiles range between 561 and 2650 cm^2 in geometrical surface and between 10 and 12 mm in thickness. By design, the segmentation of the ACD does not match that of the LAT tower modules, to avoid lining up gaps between tiles with gaps in the TKR and CAL. The design requirements for the ACD specified the capability to reject entering charged particles with

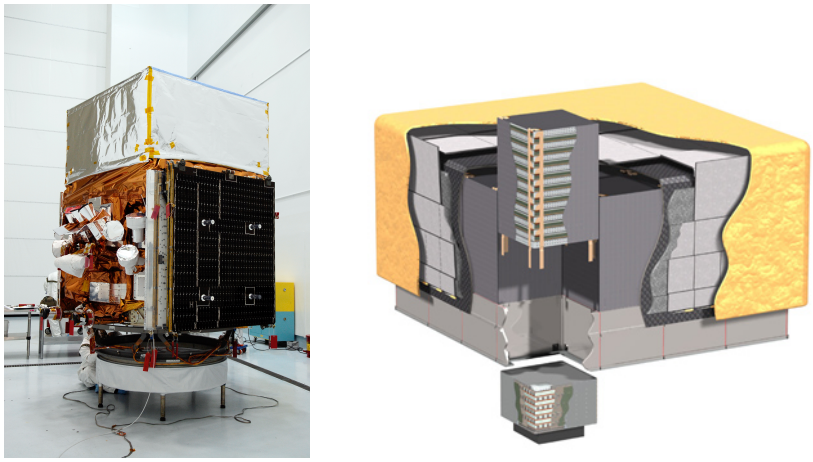

Figure 3.3: Left:The *Fermi* satellite sitting on its payload attach fitting.

an efficiency > 99.97% [124].

3.2 Performance

The basic properties of a source have to be deduced from remotely sensed observations rather than from first-hand on the spot measurements. These remotely sensed data are often difficult to interpret physically because they emerge as severely filtered convolutions of the original source function. The central 'inverse' problem is to transform these data, through integral inversion techniques, into stable and physically meaningful representations of the source [125]. Therefore, we need a good description of the instrument in order to deconvolve source information from observations. That description is enclose in the Instrument Response Functions (IRFS) and can be written in the most general form as:

$$R(E', \hat{p}'; E, \hat{p}, t) = A(E, \hat{p}, t) \times P(\hat{p}'; E, \hat{p}, t) \times D(E'; E, \hat{p}, t),$$

where:

- E is the true photon energy emitted by the source
- $\hat{p}$ the true photon direction
- E' is the measured photon energy in the *Fermi*-LAT
- $\hat{p}'$ the measured photon direction by the *Fermi*-LAT

and

- $A(E, \hat{p}, t)$ is the instrument effective area: the product of the cross-sectional geometrical collection area, gamma ray conversion probability, and the efficiency of a given event selection for a gamma ray with energy E and direction $\hat{p}$ in the *Fermi*-LAT.

- $P(\hat{p}'; E, \hat{p}, t)$ is the Point Spread Function: the probability density to reconstruct an incident direction $\hat{p}'$ for a gamma ray with $(E, \hat{p})$ in an specific event selection.

- $D(E'; E, \hat{p}, t)$ is the energy dispersion: the probability density to measure an event energy E' for a gamma ray with $(E, \hat{p})$ in a given event selection.

The IRFs related to the most updated event selection are posted in the Fermi performance webpage[1] to find more info on IRFs and the systematic uncertainty asociated to their modelling we refer to [124].

3.3 Science analysis environment

Data and analysis software are available to the general public. Members of the scientific community interested in gamma ray astronomy have access to an enormous catalog of photons coming from all the sky, increasing at a rate of around 1000 events every three hours. These these data can be downloaded, processed and analysed using the public resources provided by the Fermi Collaboration. Information about how to use data and tools can be found here `http://fermi.gsfc.nasa.gov/ssc/data/analysis/`. We also refer to the websites of the schools:

- School on Fermi science tools for Multidarkians [2]

- Workshop on DM tools and Hands-on Fermi analysis [3]

- High-energy gamma-ray astrophysics: from solar activity to black holes [4]

3.3.1 Binned likelihood analysis

To analyse *Fermi*-LAT data we maximize a likelihood function to find the best fit model parameters. These parameters include the description of a source's spectrum, its position, and even whether it exists. The likelihood L is the probability of

[1] `http://www.slac.stanford.edu/exp/glast/groups/canda/lat_Performance.htm`
[2] `http://www.ift.uam-csic.es/iftworkshops/index.php?id=7`
[3] `http://www.ift.uam-csic.es/iftworkshops/index.php?id=56`
[4] `http://www.sexten-cfa.eu/en/high-energy-gamma-ray-astrophysics-from-solar-activity-to-black-holes`

obtaining the data given an input model. In our case, the input model is the distribution of gamma-ray sources on the sky, and includes their intensity and spectra. There is an implicit assumption that we understand sufficiently well the response of our detectors to the incident flux, in other words, that we have a sufficiently accurate mapping of the input model (the gamma-ray sky) to the data (the list of counts produced by the *Fermi*-LAT). Clearly, we expect a higher probability of obtaining the data from a model that is a better description of the underlying reality than from a model that is a poor description.

Let S denote a set parameters defining our theoretical model used to describe data. The symbol S (for signal) can in general denote a discrete or continuous set of variables. Let c denote a set of observations describing a event and there are n events in our dataset. In general, for each event, c can be a vector of dimension d. Let $P(c|S)dc$ describe the probability of observing the configuration c in the d-dimensional phase space volume dc given the theoretical parameter set S. Thus $P(c|S)$ is a probability density function (pdf) in the variable c and obeys

$$\int P(c|S)dc = 1. \tag{3.1}$$

Then one can define a likelihood L of observing the dataset as:

$$L = \prod_{i=1}^{i=n} P(c_i|S). \tag{3.2}$$

The maximum likelihood point can be found of observing by minimizing the negative loglikelihood $-\mathtt{Log}L$ defined as:

$$-\mathtt{Log}L = -\sum_{i=1}^{i=n} \mathtt{Log}(P(c_i|S)), \tag{3.3}$$

while varying the parameters S either analytically or numerically to obtain the best values $S^\star$ of S that fit the data.

The data is binned into small spatial bins. Thus, even with many counts, each bin will contain few events. The observed number of counts c_i in each spatial bin is characterized by the Poisson distribution,

$$P(c_i|M_i) = \frac{M_i^{c_i} \exp^{-M_i}}{C_i!}. \tag{3.4}$$

Then the likelihood L of observing the dataset is:

$$-\mathtt{Log}L = -\left(\sum_{i=1}^{i=n} c_i \mathtt{Log}M_i - \sum_{i=1}^{i=n} M_i - \sum_{i=1}^{i=n} \mathtt{Log}c_i!\right), \tag{3.5}$$

where the last term is constant for all the models, and therefore we can neglect it. The term $\sum_{j=1}^{j=n} M_J$ is the number of predicted events in the region of interest (ROI) N_{pred} and the likelihood function become:

$$-\,\mathtt{Log}L \;=\; -\left(\sum_{i=1}^{i=n} c_i \mathtt{Log} M_i - N_{pred}\right). \tag{3.6}$$

The region of the sky that is under analysis can be modelled in the following way:

$$S(E,\hat{p},t) = \sum_i S(E,\hat{p})\delta(\hat{p}-\hat{p}') + S_G(E,\hat{p}) + S_{EG}(E,\hat{p}) + \sum_l S_l(E,\hat{p},t) \tag{3.7}$$

- $S(E,\hat{p})$ Point source intensity,
- $S_G(E,\hat{p})$ Galactic diffuse emission,
- $S_{EG}(E,\hat{p})$ Extra-Galactic diffuse emission,
- $S_l(E,\hat{p},t)$ Possibly time varying sources

Given the *Source Model* it is possible to compute the number of expected events M_i in the spatial bin i given the model. The *Source Region SR* is defined as the portion of the sky that contain all sources that contribute significantly to the ROI. SR $\sim$ 5% larger than ROI.

$$M_i = \sum_k \int_{SR} R(E',\hat{p}';E,\hat{p},t) S_k(E,\hat{p}) dE d\hat{p}. \tag{3.8}$$

The predicted number of observed events in the ROI is the sum of the predicted events M_i over the ROI.

$$N_{pred} = \sum_{i\in ROI} M_i - \tag{3.9}$$

Finally

$$\mathtt{Log}L(S) = \sum_i c_i \mathtt{Log} M_i - N_{pred}. \tag{3.10}$$

Therefore, the likelihood function compares the sum of the number of events in a bin weighted by the probability $\mathtt{Log}M_i$. The sum is taken over all pixels i since M_i is calculated using an average over a finite size bin. We call $\hat{S}$ the optimal model parameters, i.e. the ones that maximize $L(S)$

Chapter 4

Line signal and background

We rushed into the captain's cabin ... there he lay with his brains smeared over the chart of the Atlantic ... while the chaplain stood with a smoking pistol in his hand.
Sir Arthur Conan Doyle, *The Adventure of the Gloria Scott*.

Contents

4.1 CLUES on *Fermi*-LAT prospects for detection of $\mu\nu$SSM gravitino DM 36
4.1.1 Introduction 36
4.1.2 Simulations with the Fermi Science Tools 37
4.1.3 $\mu\nu$SSM gravitino dark matter: prospects of detection with Fermi-LAT 38
4.1.4 Conclusions and outlook 42
4.2 Tentative line at 130 GeV? 43
4.2.1 The *Fermi*-LAT search for gamma-ray lines: focusing on 130 GeV 45
4.2.2 Fitting results and upper limits 46
4.2.3 133 GeV feature in the control regions 46
4.2.4 Conclusions 49

The detection of a gamma-ray line is a smoking-gun evidence for DM particle annihilation or decay as no other plausible phenomena can produce that sharp spectral signature. In this chapter we present prospects and searches for gamma-ray lines in the *Fermi*-LAT data. First, the prospects in the work [22] carried out in collaboration with M. Fornasa, F. Zandanel, A. J. Cuesta, C. Munoz, F. Prada and G. Yepes. There we study the gamma-ray line produced by gravitinos as DM in the $\mu\nu$SSM [23, 24]. In this work we have confirmed the potential of using extragalactic massive structures as optimal targets for decaying DM detection. Second, in this chapter we present the bottom line and main conclusions of the work [25] where the *Fermi*-LAT collaboration perform a thorough search of gamma-ray lines paying special attention to the energy range about 130 GeV, where the detection of a line has been claimed [26, 27].

4.1 CLUES on *Fermi*-LAT prospects for detection of $\mu\nu$SSM gravitino DM

4.1.1 Introduction

As already discussed in chapter 2, the $\mu\nu$SSM is a supersymmetric model that has been proposed to solve the problems generated by other supersymmetric extensions of the standard model of particle physics [99, 100, 101]. Given that R-parity is broken in the $\mu\nu$SSM, the gravitino is a natural candidate for decaying dark matter since its lifetime becomes much longer than the age of the Universe. In this model, gravitino dark matter could be detectable through the emission of a monochromatic gamma ray in a two-body decay. We study the prospects of the Fermi-LAT telescope to detect such monochromatic lines in 5 years of observations of the most massive nearby extragalactic objects. The dark matter halo around the Virgo galaxy cluster is selected as a reference case, since it is associated to a particularly high signal-to-noise ratio and is located in a region scarcely affected by the astrophysical diffuse emission from the galactic plane.

In our analysis we use the following strategy. The DM density field of the nearby extragalactic Universe is described using the maps provided in Ref. [123], and based on a constrained N-body simulation provided by the CLUES project. This density is then taken as an input for the Fermi observation simulation tool to predict the photon signal. We will use the most recent version of the public Fermi Science Tools[1] to describe the performance of the telescope and to simulate both the DM signal and the astrophysical background. From the analysis of the simulated photon maps we finally compute our prospects of detection for the $\mu\nu$SSM gravitino.

In the DM halo of the Milky Way the gamma-ray flux coming from DM decay is maximized in the direction of the galactic center where the DM density is larger. This region, however, should be considered with particular care since the gamma-ray emission due to the presence of conventional astrophysical sources is not fully understood [127, 128].

The expected diffuse gamma-ray emission from DM decay in the mid-latitude range ($10^\circ \leq |b| \leq 20^\circ$) was computed for a Navarro-Frenk-White (NFW) profile [42, 43] in Ref. [120] and compared with the 5-month measurement reported by Fermi-LAT [129]. The non-observation of sharp monochromatic lines in the gamma-ray spectrum permitted to draw bounds on the parameter space of the $\mu\nu$SSM gravitino. In particular, values of gravitino mass $m_{3/2}$ larger than about 10 GeV were excluded, as well as lifetimes $\tau_{3/2}$ smaller than about 3 to 5×10^{27} s. Notice that because of this upper bound on $m_{3/2}$, three body decay modes of the

[1] `http://fermi.gsfc.nasa.gov/ssc/data/analysis`

gravitino [130, 131] are not relevant, and therefore we do not considered them in this work.

It is worth noticing here that in Ref. [132] ([133]) the Fermi-LAT collaboration presented constraints on monochromatic emission using 11 (23) months of data for $|b| > 10^\circ$ *plus* a $20^\circ \times 20^\circ$ square around the galactic center. However, the derived limits only refer to the emission above 30 (7) GeV, covering, in the context of the $\mu\nu$SSM, gravitinos with masses larger than 60 (14) GeV, leaving our region of interest unconstrained. On the other hand, in work [134], two-years Fermi-LAT data for $|b| \geq 10^\circ$ have been used to constrain the DM gamma-ray line flux in the energy range between 1 and 300 GeV. Lower bounds on $\tau_{3/2}$ of about $5{\times}10^{28}$ s were obtained in our region of interest below 10 GeV. Recently, these bounds together with those obtained in [135] by analyzing the data from EGRET were used in [136] to constrain the parameter space of gravitino dark matter in the bilinear R-parity violating model.

We already shown in subsection 2.3.1 how gamma rays are produced in gravitino decays, as well as the procedure to calculate their flux from decays taking place in both, galactic and extragalactic structures. We refer there for more details. Regarding the DM distribution, the Box160CR CLUES simulation was used, containing 1024^3 particles in a box with a side of 160 h^{-1} [123, 39]. The all-sky maps are publicly available[2] both in the case of an annihilating and a decaying DM particle. Here we use the map corresponding to the case of decaying DM. The gamma-ray flux can be derived from the values in the map simply multiplying them by the particle physics factor shown outside the integral in Eq. (2.22). This result is used as input for the Fermi-LAT observation simulations, which we will describe in the next subsection.

4.1.2 Simulations with the Fermi Science Tools

For this work, the simulation of gamma-ray events was carried out with the `gtobssim` routine, part of the Fermi Science Tools package v9r23p1. Its output is a list of mock gamma-ray events with corresponding spatial direction, arrival time and energy, distributed according to an input source model. Our source model accounts for the gamma-ray signal from $\mu\nu$SSM gravitino decay as described in previous sections, and for the galactic and extragalactic background diffuse emission. In particular, the galactic background emission is mainly correlated with structures in the Milky Way since it arises from the interaction of high-energy cosmic rays with the interstellar medium and the interstellar radiation field. The far extragalactic background, on the contrary, is supposed to be almost isotropic. Its value is based on the modelization of the galactic component, on detected Fermi-

[2] `http://www.clues-project.org/articles/darkmattermaps.html`

LAT sources, and on the solar gamma-ray emission. We used the so-called RING model[3] as recommended by the Fermi-LAT collaboration, which is obtained as a fit to the real Fermi-LAT data.

The simulation of gamma-ray events through `gtobssim` is based on in-flight Instrument Response Functions (IRFs), accounting for the telescope effective area, energy dispersion and point-spread function (PSF). Two IRFs publicly available are called P6_V3_DIFFUSE and P6_V3_DATACLEAN. They both profit from the improvement in the knowledge of the telescope performances after the first two years of data taking [137]. The main difference between the two IRFs is the fact that DATACLEAN event selection perform most stringent cuts than DIFFUSE on the interpretation of an event as a real photon. As will be discussed below, in this work we present results from P6_V3_DIFFUSE, but the sensitivity of our results on the choice of the IRFs have been checked without finding any significant effect.

4.1.3 $\mu\nu$SSM gravitino dark matter: prospects of detection with Fermi-LAT

Let us finally study the prospects for $\mu\nu$SSM gravitino DM detection, taking into account the contributions discussed in Sect. 2.3.1. First, we simulate the all-sky map of 5-years Fermi-LAT observations, separately for DM gamma-ray events and background events. For DM, as an example we show in Fig. 4.1 the case of a gravitino with mass $m_{3/2} = 8$ GeV and lifetime $\tau_{3/2} = 2.5 \times 10^{26}$ s. Gamma-rays in the energy range between 3.4 GeV and 4.6 GeV are simulated. This energy range corresponds to an interval of $\pm 2\,\Delta E$ around the position of the line (4 GeV), where ΔE=0.3 GeV is the energy resolution (at 68% containment normal incidence) of the telescope at that energy.

Since we want to determine the Fermi-LAT capability of detecting local extragalactic DM structures, the gamma-ray emission from DM is what we will refer to as *signal*. For each direction of the sky ψ, the number of signal (S) and background (B) photons are determined integrating over a 3×3 degrees region centered in ψ. The S/N ratio is then defined as $S/\sqrt{S+B}$. From the map we can infer which extragalactic structure is the best target to derive our prospects for detecting gravitino DM. Let us remark first that we are not simulating the contribution of the point sources already detected by Fermi-LAT and present in the 2 year catalog [**?**]. Since this contribution represents a source of uncertainty, the S/N ratio should not be considered as a good estimator of the prospects for detecting DM in the regions where the contamination of the point sources is dominant. Also the discover in the Fermi-LAT data of lobes structures [138], extending up to 50 degrees above and below the galactic plane introduce a new source of background not included in this

[3] `http://fermi.gsfc.nasa.gov/ssc/data/access/lat/BackgroundModels.html`

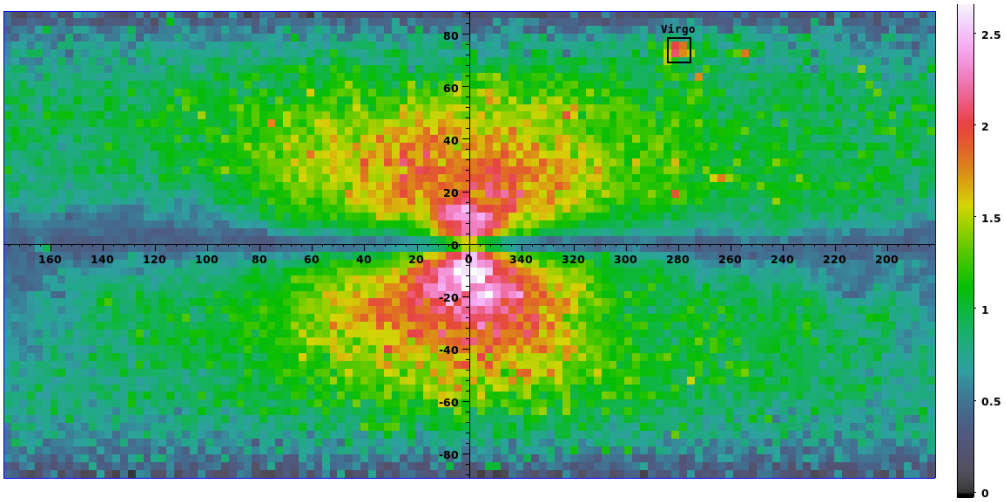

Figure 4.1: S/N all-sky map of gamma-ray emission from gravitino DM decay simulated using the Fermi Science Tools. DM events are from the decay of a $\mu\nu$SSM gravitino with $m_{3/2} = 8$ GeV and $\tau_{3/2} = 2.5 \times 10^{26}$ s. The signal comes from all three DM components: galactic halo, and both, local (from CLUES simulation) and far (isotropic) extragalactic DM density. The black square indicates the position of the Virgo cluster. Pixels in the map have an angular dimension of 3×3 degrees. Figure from [22].

work. The inner galaxy region is characterized by a quite large S/N ratio (around 3). However, contamination from point sources as well as the poorly-understood Fermi lobes is known to be large at low galactic latitudes, significantly affecting the reliability of our predictions in this region. It is worth noticing here that in [132, 133] the region $|b| \geq 10^\circ$ *plus* a $20^\circ \times 20^\circ$ square around the galactic center was used as target. Let us remark that these works follow a different kind of analysis, searching spectral deviations from a power-law behavior. We note that in such a large region of the sky the energy spectra used as background can be well described as a power law. Therefore, these works have no problems concerning background uncertainties.

Thus we neglect the zone with large S/N close to the galactic center and plane, and focus only on the case of extragalactic sources. Among these, the object with the largest S/N ratio ($S/N = 2.1$) is the Virgo cluster. In our analysis we only select this cluster, indicated with a black square in Fig.4.1. Although in [123] filamentary regions of the cosmic web were pointed out as good targets for DM decay searches, in this analysis, where we are using a different particle physics model (and energy range), we do not find in principle a significant S/N ratio in those regions.

As described in Ref. [123], the projected map is generated with Virgo being

fixed in its real observed position because it is the best constrained object in the simulation, and therefore it is certainly the best object to consider for our purposes. Besides, there are two point sources detected near Virgo, M87 and 2E1228+1437, with an integrated flux of $(3.3\pm0.8)\times10^{-10}$ ph/cm^{2}s and $(1.6\pm0.6)\times10^{-10}$ ph/cm^{2}s between 3 and 10 GeV, respectively [20]. In a 5×5 degree region around Virgo and free of the two point sources, the total gamma-ray flux from DM decay is 2.5×10^{-9} ph/cm^{2}s (for an example of a 8 GeV gravitino with a lifetime of 5×10^{27}s), one order of magnitude larger than the contribution of the point sources. Smaller regions like 1×1 or 3×3 degrees are more affected by the emission due to the point sources. On the other hand, going to larger regions like 7×7 degrees, the signal contribution is not significantly increasing and therefore the S/N ratio decreases. Thus, hereafter we select a 5×5 degree region around Virgo as the best target to obtain our predictions.

With the purpose of scanning the most interesting portion of the $\mu\nu$SSM parameter space, we re-simulate the gamma-ray events from the region of 5×5 degrees around Virgo changing the value of the gravitino mass. We run 17 different simulations of this region, each one with a different value for the gravitino mass, ranging from 0.6 to 10 GeV, for a given decay lifetime. The lower bound of 0.6 GeV on the gravitino mass is chosen because it corresponds to a line energy of about 0.3 GeV, where the PSF (point spread function) of the Fermi LAT becomes larger than our region of interest. The energy interval covered by each simulation is $[(m_{3/2}/2-\Delta E),(m_{3/2}/2+\Delta E)]$, where the energy resolution (at 68% containment normal incidence) ΔE is computed at the position of the line. Using the results of those simulations, we determine the values of lifetimes corresponding to a $S/N=5$ ($S/N=3$) . These are plotted as blue (green) dots in Fig. 4.2, as a function of $m_{3/2}$. The blue (green) region indicates points with $S/N\geq5$ (3). This is the main result of our work.

Let us remark that the errors in the figure are obtained propagating the statistical errors on the number of signal and background events (assuming Poissonian statistics). Regarding possible systematic errors, we note here that the points in Fig. 4.2 are obtained with the P6_V3_DIFFUSE IRF but the simulations were repeated using both, P6_V3_DATACLEAN and P7CLEAN_V6, and the results are found to be compatible. The use of P6_V3_DIFFUSE allows us to estimate the systematic error on our limits to be between 5 and 20%.

As mentioned above, in Ref. [120] the area below the red dot-dashed line was disfavored by Fermi-LAT data of the diffuse gamma-ray galactic emission in the mid-latitude range $10^\circ\leq|b|\leq20^\circ$. In addition, in Ref. [134], the area below the black dots was also disfavored. From a likelihood analysis focused on the region $|b|\geq10^\circ$, lower bounds on $\tau_{3/2}$ of about 5×10^{28} s were obtained in our region of interest below 10 GeV. On the other hand, the area below the yellow dashed line is disfavored by the bounds obtained in [135] by analyzing the data from EGRET in

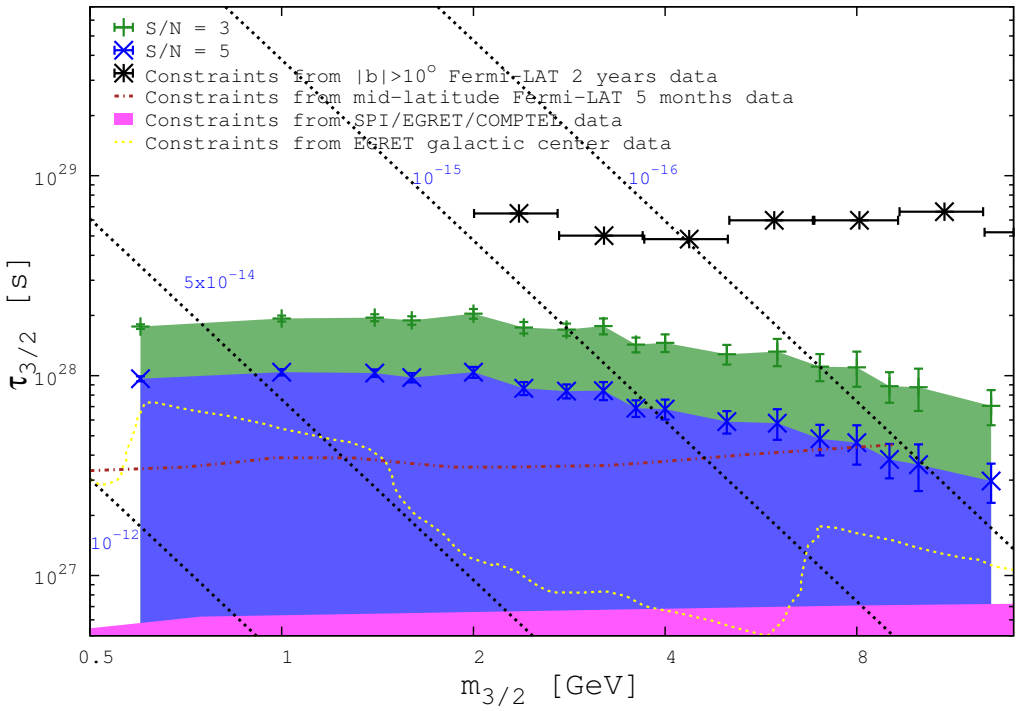

Figure 4.2: Constraints on lifetime versus mass for gravitino DM in the $\mu\nu$SSM. Blue (green) points indicate values of $\tau_{3/2}$ and $m_{3/2}$ of the $\mu\nu$SSM gravitino corresponding to a detection of gamma-rays with a $S/N = 5$ (3) in the 5×5 degree region centered on the position of the Virgo cluster, for a 5 years simulation using the Fermi Science Tools. The blue (green) region indicates points with S/N larger than 5 (3). The red dot-dashed line indicates the lower limit on $\tau_{3/2}$ obtained from the Fermi-LAT measurements of the mid-latitude gamma-ray diffuse emission after 5 months [120]. The yellow dashed line indicates the lower limit on $\tau_{3/2}$ obtained from the EGRET measurements of the galactic center gamma-ray emission. The black dots show the lower limit on $\tau_{3/2}$ obtained in the adopted energy bands [134], from the Fermi-LAT measurements of the $|b| \geq 10^\circ$ gamma-ray diffuse emission after 2 years. The black dashed lines correspond to the predictions of the $\mu\nu$SSM [120] for several representative values $|U_{\tilde{\gamma}\nu}|^2$=$10^{-16}$, 10^{-15}, 5×10^{-14}, 10^{-12} (see Eq. (2.21)). The magenta shaded region is excluded by gamma-ray observations such as SPI, COMPTEL and EGRET [139]. Figure from [22].

the galactic center region. In particular, we used the upper limits on the gamma-ray line fluxes obtained in that work to constrain the $\mu\nu$SSM gravitino lifetime. Finally, points in the magenta shaded region are excluded by gamma-ray observations from the galactic center obtained with the SPI spectrometer on INTEGRAL satellite, and

the isotropic diffuse photon background as determined from SPI, COMPTEL and EGRET data [139].

On the other hand, the black dashed lines correspond to the predictions of the $\mu\nu$SSM for several representative values of the R-parity mixing parameter. As mentioned in Sect. 2.3.1, this is constrained to be $|U_{\tilde{\gamma}\nu}|^2 \sim 10^{-16} - 10^{-12}$ in the $\mu\nu$SSM [120], in order to reproduce the correct neutrino masses. As a consequence, any acceptable point must be in the area between the left and right black dashed lines. Let us remark, however, that these bounds are very conservative, as discussed in [120], and in fact the results of a scan of the low-energy parameter space of the $\mu\nu$SSM implied that the range $10^{-15} \leq |U_{\tilde{\gamma}\nu}|^2 \leq 5 \times 10^{-14}$ is specially favored. The corresponding lines are also shown in the figure.

The combination of the constraints associated to red dot-dashed and black dashed lines, implies already that values of the gravitino mass larger than about 10 GeV are excluded, as well as lifetimes smaller than about 3 to $5{\times}10^{27}$ s [120]. Actually, in the region of gravitino masses between 0.6 and about 1.5 GeV, lifetimes smaller than about 7 to 3×10^{27} s, respectively, are excluded because of the constraints associated to the yellow dashed line. When constraints associated to black dots are also imposed, it turns out that the gravitino mass has to be smaller than about 4 GeV, and lifetimes have to be larger than about 6×10^{28} s for gravitino masses between 2 and 4 GeV. Thus, the combination of these results with the one obtained above for detection of DM from Virgo in 5 years of Fermi-LAT observations, leaves us with the blue and green areas above the yellow dashed and red dot-dashed lines, and gravitino mass smaller than 2 GeV, as those with good prospects for DM detection. Summarizing, we find that a gravitino DM with a mass range of 0.6–2 GeV, and with a lifetime range of about 3×10^{27}–2×10^{28} s would be detectable by the Fermi-LAT with a signal-to-noise ratio larger than 3. If no gamma-ray lines are detected in 5 years, these regions of the parameter space of the $\mu\nu$SSM would be excluded.

4.1.4 Conclusions and outlook

In this work we have obtained the regions of the parameter space $(m_{3/2}, \tau_{3/2})$ of the $\mu\nu$SSM with the best prospects for the detection of a gamma-ray monochromatic line from the decay of gravitino DM (see Fig. 4.2). Summarizing, we find that a gravitino DM with a mass range of 0.6–2 GeV, and with a lifetime range of about 3×10^{27}–2×10^{28} s would be detectable by the Fermi-LAT with a signal-to-noise ratio larger than 3. We also obtain that gravitino masses larger than about 4 GeV are now disfavored in the $\mu\nu$SSM by Fermi-LAT data of the galactic halo.

In the analysis we have assumed 5 years of observation of the Virgo cluster by the Fermi-LAT space telescope. This cluster was selected as our optimal target due to its particularly high S/N ratio. Of course, a more precise determination of the

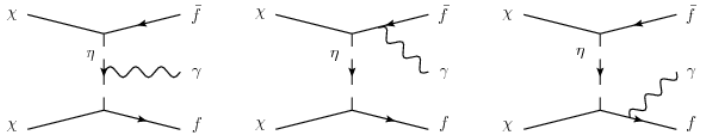

Figure 4.3: Feynman diagrams of the processes that contribute in leading order to the three-body annihilation cross-section and produce internal bremsstrahlung. The first diagram very roughly corresponds to VIB, the second and third to FSR. Figure taken from [26].

Fermi-LAT possibilities of detecting gamma-ray lines towards Virgo would require the simulation of both, M87 and 2E1228+1437. Also a more sophisticated analysis pipeline than the computation of the S/N ratio, possibly through the determination of a test-statistics (TS) likelihood in order to derive the lower value of $\tau_{3/2}$ for which the signature of a line would be detectable with respect to the background.

Let us remark that the simulation of the gamma-ray flux was carried out with the use of the `gtobssim` routine from the Fermi Science Tools, whereas the DM distribution around the cluster has been modeled following the results of Ref. [123] based on a constrained N-body simulation from the CLUES project. With the present work we have also confirmed the potential of using extragalactic massive structures as optimal targets for decaying DM detection. For such a goal the maps of the local extragalactic DM distribution produced in Ref. [123] represent a unique, ready-to-use tool.

We conclude that there are good prospects for Fermi to detect monochromatic lines from gravitino decay in the energy range spanning from hundreds MeV to few GeV. That is also the energy range where it is more difficult to extract information from the data, due to imperfect parametrization of the background as a simple power law. Nevertheless, our results in Fig. 4.2 can be considered as an additional motivation to extend the Fermi-LAT analysis on lines to energies below 2 GeV.

4.2 Tentative line at 130 GeV?

We already mention in 2.2.1 that in some models WIMPs would annihilate to photons through loops. Another possibility for WIMPs to produce sharp spectral features is through internal bremsstrahlung. This process is not loop suppressed, it is a three body final state diagram containing a photon, see figure 4.3, therefore the photon flux is higher than in annihilation to two bodies. T. Bringmann et. al. looking for an internal bremsstrahlung-like signal in the public *Fermi*-LAT found a weak indication (3.1σ and 4.3σ global and local significance, respectively) cor-

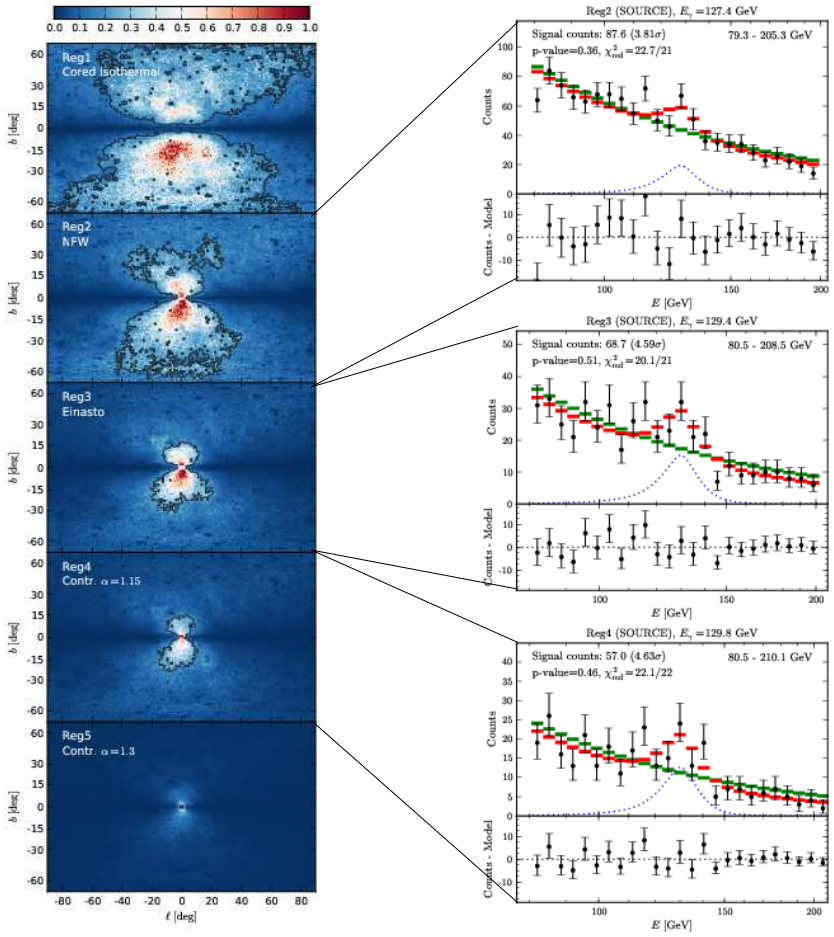

Figure 4.4: Left: Target regions optimized for DM line searches for different DM profiles. Right: Upper sub-panels: the measured events with statistical errors are plotted in black. The horizontal bars show the best-fit models with (red) and without DM (green), the blue dotted line indicates the corresponding line flux component alone. In the lower sub-panel we show residuals after subtracting the model with line contribution. Figures from [27]

responding to a DM mass of $\sim$ 150 GeV, i.e. a gamma-ray line at 130 GeV. The Fermi data analysis in that work was performed by Christopher Weniger, who a month later presented a paper improving the initial analysis, finding 3.2σ and 4.6σ global and local significance, respectively, for the line at 130 GeV [27]. See figure 4.4 for a visual image of the tentative line. This claim generated a big excitement in the community given its implications for DM, and many papers appear in the arXiv confirming the line and/or explaining it, further a group in Harvard claimed for two lines, at 110 GeV and 130 GeV. [140].

Profile	ROI	Ann. Jfactor*	ROI	Decay J-factor**
NFW Contracted	R3	13.9	R180	2.42
Einasto	R16	8.48	R180	2.49
NFW	R41	8.53	R180	2.46
Isothermal	R90	6.94	R180	2.80

Table 4.1: Summary of optimized ROIs and J-factor values for each of the four DM density profiles considered for both annihilation or decaying WIMPs. *in units of 10^{22} GeV^2 cm^{-5}. **in units of 10^{23} GeV cm^{-2}.

4.2.1 The *Fermi*-LAT search for gamma-ray lines: focusing on 130 GeV

The *Fermi*-LAT collaboration performed a careful search for lines [25] significantly improving its previous analysis [132, 133]. We used 3.7 years of reprocessed data in the energy band 5-300 GeV. The improvements in the quality of the *Fermi*-LAT data with the reprocessing include, a better description of the PSF above a few GeV, a slight upward shift in energy of spectral features after account for the decrease in scintillation light yield in the crystals with time (~1% per year) from radiation exposure on orbit, and updated calorimeter calibration constants that allows better reconstruction of photon energy. Following Weniger [27] we have developed a set of five Region Of Interest (ROIs) optimized for sensitivity to WIMP annihilation or decay based in comparing the signal gamma rays expected from WIMP annihilation or decay in four reference models for the distribution of DM in the Galaxy to the background gamma rays expected from astrophysical processes. The 5 ROIs presented in the table 4.1 are circular regions of radius R_{GC} centered on the GC with $|b| < 5^\circ$ and $|l| > 6^\circ$ masked. Left panels of the figure 4.5 shows the outline of the ROIs.

We searched for spectral lines by performing maximum likelihood fits in sliding energy intervals in the five ROIs presented in table 4.1. Specifically, we fit the count spectra in the energy domain, integrating over each ROI. In the likelihood method an important improvement in this analysis is the inclusion of the quantity P_E, that measures the probability that the energy estimated is within the nominal 68% containment band for events of that energy and incidence angle. the fitting method used in previous *Fermi*-LAT line searches [132, 133], use a 1D energy dispersion model (without P_E); in [25] including the extra-information from P_E to parametrize the energy dispersion ("2D" model) in the likelihood fitting, the statistical power is increased by 15% on average. In comparison an analysis with 1D model, would require 30% more data to provide equivalent sensitivity.

4.2.2 Fitting results and upper limits

In the energy range 5-300 GeV we find no globally significant lines in the 5 ROIs under study. The two most statistically significant fits were in R180 at 6.3 GeV, with local significance $s_{\rm local} = 3.1\sigma$ and $f = 0.0010 \pm 0.002$, and in R3 at 135 GeV, with $s_{\rm local} = 3.2\sigma$ and $f = 0.58 \pm 0.18$, where f is the effective signal fraction at the line energy. For the fit at 6.3 GeV in R180 the signal fraction f is similar to the expected systematic uncertainty of $\delta f = \pm 0.008$ for R180 at that energy, see table IV in [25]. Instead for the fit at 135 GeV in R3 the signal fraction f is much larger than systematic level. A finer scan around 135 GeV found the most significant fit in R2 at 133 GeV, with $s_{\rm local} = 3.3\sigma$ and $f = 0.61 \pm 0.19$; this correspond to a global significance $s_{\rm global} = 1.6\sigma$, see middle up panel of the figure 4.5. Since no global significant lines were detected, we have derived 95% confidence level (CL) upper limits (UL) on the gamma-ray flux from spectral lines. Based on that we set constraints on the upper limits on $\langle \sigma v \rangle_{\gamma\gamma}$, see right panel of the figure 4.5, and lower limits on decay lifetime $\tau_{\gamma\nu}$, see figure 4.6. The feature presented in [27] has shifted from 130 GeV to 133 GeV, as expected from the application of improved calibrations.

Following the evolution of the feature at 133 GeV with different datasets and signal models we found that the significance of the line decrease. Changing the energy dispersion model, from 1D to 2D causes $s_{\rm local}$ to decrease by 20% in R3 and 27% in R16. Simulations including DM predict that $s_{\rm local}$ should increase, on average, by 15% in this case. A decrease by 20% or more occurred in 2% of the simulations. The decrease in significance with the 2D model implies that the clustering of events around the peak energy as a function of P_E in the flight data does not match variations in instrument performance well; this disfavors the interpretation of the 133 GeV feature as a DM line. We also perform the fit in R3 using 4.4 years data instead of the 3.7 years used in all the other fits. The significance decreased by $\sim 10\%$ with the 4.4-year dataset relative to the 3.7 year dataset. A very important characteristic of the feature at 133 GeV in R3 is its width. The 2D energy dispersion model predicts a broader distribution of photons than the feature observed in the flight data for a gamma-ray line. After quantify the width of the feature we conclude that it is not compatible with our understanding of the energy dispersion from simulations and beam test, see figure 4.7.

4.2.3 133 GeV feature in the control regions

We examine two control datasets that are expected to contain little or no DM. The first was the Limb dataset, see left panel of the figure 4.8, while the second was a region centered on the Galactic plane but excluding the GC, which we call the inverse ROI. The inverse ROI contains a variety of gamma-ray sources, but provides

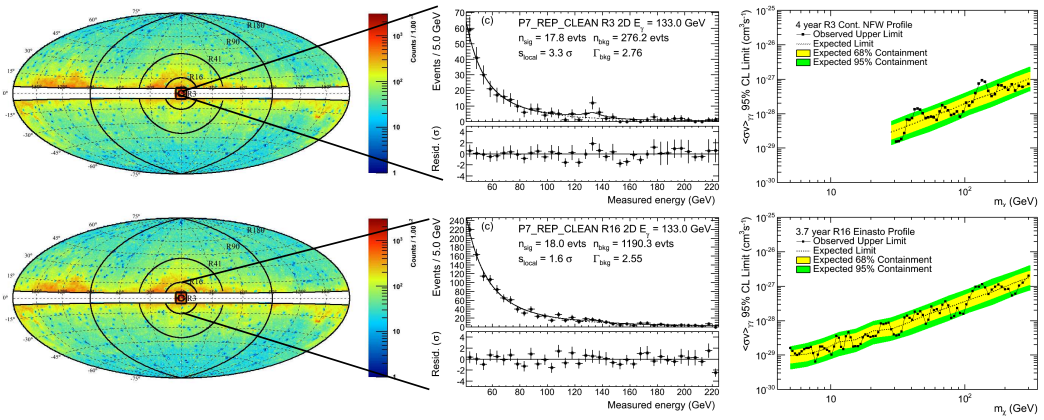

Figure 4.5: Left: Counts map for the line search dataset binned in $1^\circ \times 1^\circ$ spatial bins in the R180 ROI. This is plotted in Galactic coordinates using the Hammer-Aitoff projection. The energy range is 2.6-541 GeV and the most-significant 2FGL sources have been removed using an energy-dependent mask. Also shown are the outlines of the other ROIs (R3, R16, R41, and R90) used in this search. Middle up: Fits for a line at 133 GeV in R3 ROI (NFW contracted) using the 2D energy dispersion model. Middle down: same as middle up but for R16 ROI (Einasto). Right up: 95% CL $\langle\sigma v\rangle$ upper limits for R3 ROI (NFW contracted). Yellow (green) bands show the 68% (95%) expected containment derived from 1000 single-power-law (no DM) MC simulations. The dashed lines show the median expected limits from those simulations. Right down: same that right up but for R16 ROI (Einasto). Figures from [25].

good statistics and a reasonable sample of the astrophysical backgrounds that we might expect from the GC.

For the Earth Limb the right panel of the figure 4.8 shows the fit using our 2D energy dispersion model at 133 GeV to the Limb data, which indicates a 2.0σ excess. We calculated the fractional size of the signal to be $f(133\ \mathrm{GeV})_{\mathrm{Limb}} = 0.14 \pm 0.07$. The gamma-ray spectrum of the Limb is expected to be featureless. Therefore, the appearance of a line-like feature in the Limb at the same energy as the feature seen in the GC suggests that some of the 133 GeV GC feature may be due to a systematic effect. We do note that the fractional size of the feature in the Limb is smaller than observed in the smallest ROIs around the GC: $f(133\ \mathrm{GeV})_{\mathrm{R3}} = 0.61 \pm 0.19$. therefore, the Limb feature is not large enough to explain all the GC signal. In the right panel of the figure 4.8 we can see dips in efficiency below and above 133 GeV, they appear to be related to an event reconstruction effect that could be artificially sculpting the energy spectrum.

Left panels of the figure 4.9 show the inverse ROIs defined to perform the con-

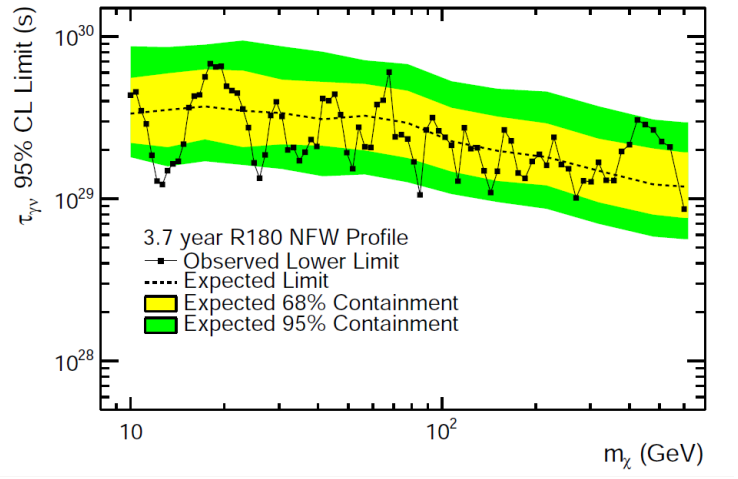

Figure 4.6: 95% CL $\tau_{\gamma\gamma}$ lower limits in R180 for a NFW profile. Yellow (green) band show the 68% (95%) expected containment derived from 1000 single-power-law (no DM) MC simulations. The dashed lines show the median expected limits from those simulations.

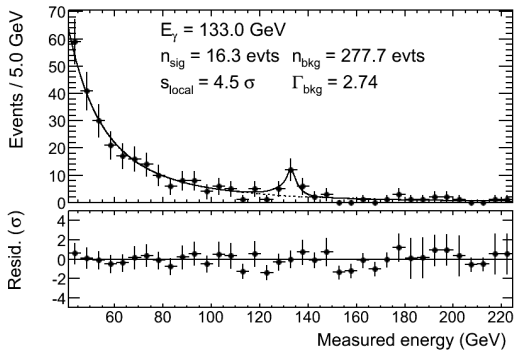

Figure 4.7: Fit to a gamma-ray line at 133 GeV in the R3 reprocessed data using the 2D model including a scale factor for the width of the energy dispersion. The best fit width of the energy resolution was $s_\sigma = 0.32^{+0.30}_{-0.13}$ (95% CL) of that predicted from MC simulations. The dotted line shows the best-fit curve with s_σ fixed to 1.0. Note that when s_σ is allowed to vary the signal model includes two more degrees of freedom than the null hypothesis, so $s_{\rm local}$ is less than $\sqrt{TS}$.

trol test. Right panels in figure 4.9 show the results of fits for lines at 133 GeV in the three inverse ROI regions. We find no clear indication for a 133 GeV line feature in these inverse ROI control datasets.

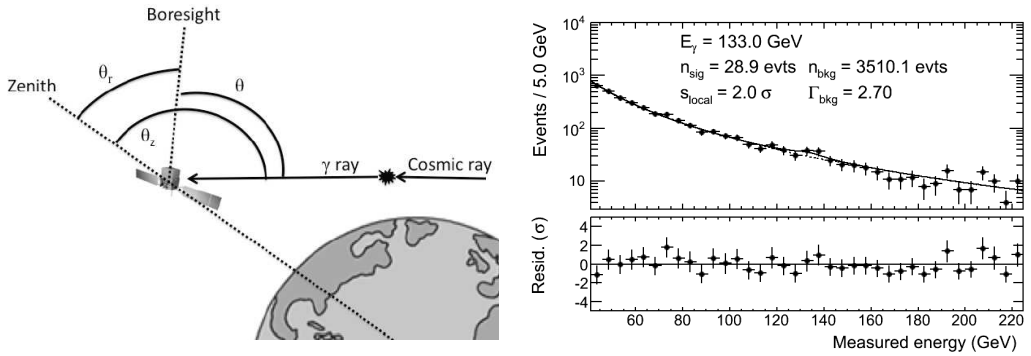

Figure 4.8: Left: Schematic of Limb gamma-ray production by CR interactions in the Earth's atmosphere, showing the de nitions of the zenith angle (θ_z), the spacecraft rocking angle (θ_r) and the incidence angle (θ). Dashed line starts at the center of the Earth. Not drawn to scale. Right: Fit at 133 GeV line to the Limb data (P7REP CLEAN) using the 2D energy dispersion model. Figures from [25].

4.2.4 Conclusions

We have performed a search for gamma-ray spectral lines from 5-300 GeV in 5 ROIs defined a priori to optimize sensitivity for various DM density profiles. This search was performed using 3.7 years of data that have been reprocessed using updated CAL calibration constants, and the 2D energy dispersion model that includes information about the event-by-event energy reconstruction quality.

We found no globally significant spectral line signals and present flux upper limits for monochromatic sources. For a particular DM density profile for the MW, the flux upper limits can be translated to annihilation cross section upper limits or decay-lifetime lower limits. Figure 4.5 shows the 95% CL upper limits on $\langle\sigma v\rangle_{\gamma\gamma}$ for the contracted NFW (R3) and Einasto (R16) DM density profiles for the ROIs that provide the best sensitivity.

Flux of a line-like feature in the GC reported using the public data is not ruled out by our 95% CL gamma-gamma flux limits in R3.

The fit at 133 GeV in R3 yields $s_{\rm local} = 3.3\sigma$ with $f(133\ {\rm GeV})_{\rm R3} = 0.61$, which is larger than any of the systematic effects considered in [25] and is larger than the feature seen at 133 GeV in the Limb: $f(133\ {\rm GeV})_{\rm Limb} = 0.14$. Also, if the feature is due to an instrumental effect, one would have expected it to appear in the spectra of gamma rays from the inverse ROI, which it does not. Therefore, the 133 GeV feature in R3 cannot be entirely explained in terms of known systematic effects. However, the 133 GeV feature does have certain characteristics that disfavor interpreting it as a DM signal. The fit significance reduces when using the 2D energy dispersion model, making the global significance of the feature $s_{\rm global} = 1.6\sigma$. This

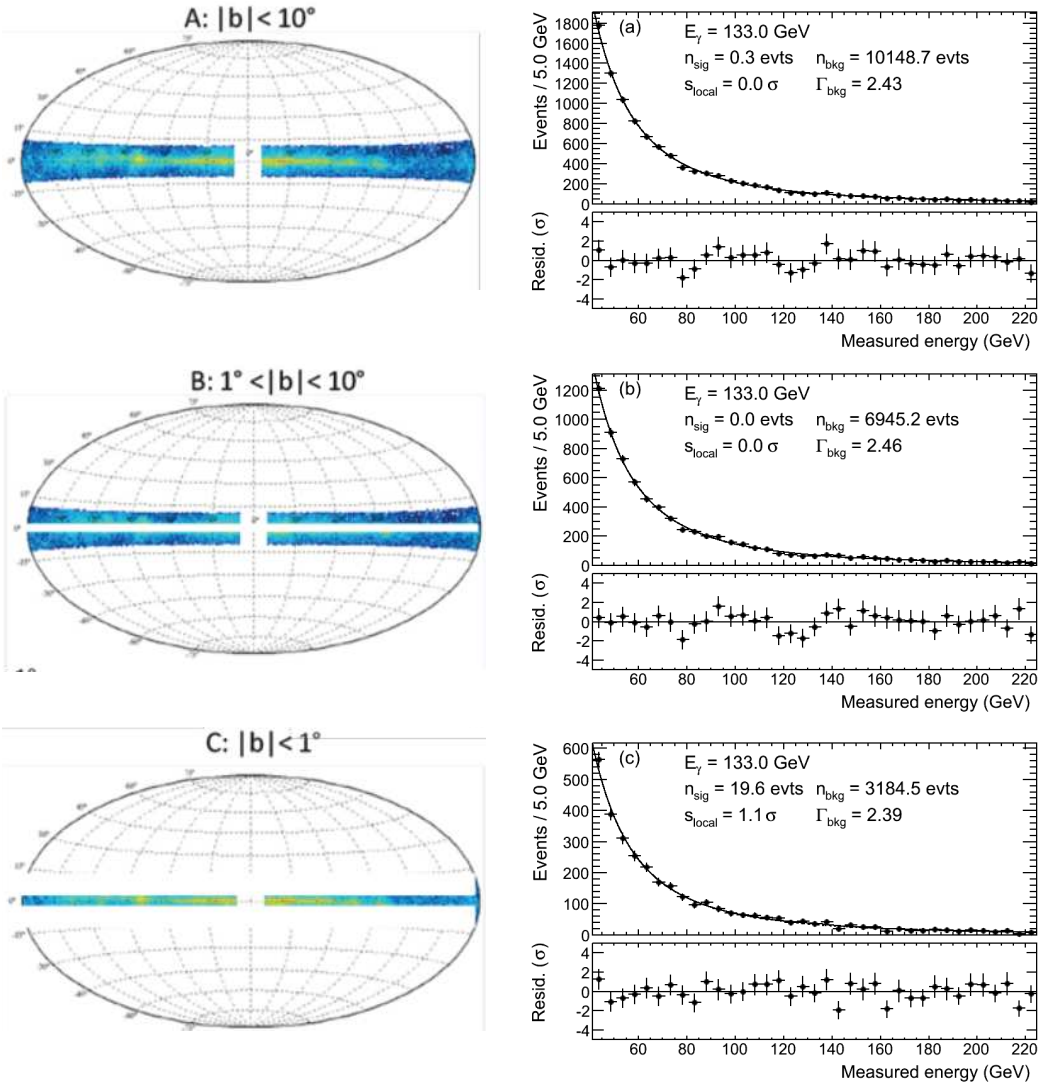

Figure 4.9: Left: Control regions which we expected to have little DM. Right: Fits for a 133 GeV line in inverse ROIs (P7REP CLEAN) using the 2D energy dispersion model. No obvious feature at 133 GeV in the inverse ROIs. Figures from [25].

decrease in significance is in large part due to the 133 GeV feature being much narrower than the LAT energy resolution, and not being present in events with $\theta >$ 50°. More data and study are needed to clarify the origin of this feature.

Two ongoing developments will help to resolve the question of the origin of the 133 GeV feature and also benefit future line searches: A new *Fermi*-LAT event-level analysis framework, the so-call `Pass 8`, is currently being developed and will increase the effective area in about 25%, also will provide different and better

systematics, which will help to clarify if the feature at 133 GeV is a systematically induced artifact. More Limb data from pole stares and future "Target of Opportunity" will help to constrain the uncertainties from narrow features in the effective area, which are among the dominant source of potential systematic uncertainties that may induce a fake signal.

Chapter 5

Diffuse signal and background in the inner region of the Milky Way

...En cualquier caso, la piscina en la que cayó la chica aquella noche es siempre la misma. Sus proporciones y su función en el relato no varían ...Lo que cambia -lo que siempre aparece suelto y sujeto a múltiples interpretaciones- es la chica en cuestión ...

Rodrigo Fresán, *La chica que cayó en la piscina aquella noche*.

Contents

5.1 Constraints on WIMP Annihilation for contracted DM in the Inner Galaxy with the *Fermi*-LAT 54

5.1.1 DM density profiles 55

5.1.2 DM induced gamma rays from WIMP annihilations 56

5.1.3 Gamma-ray flux from *Fermi*-LAT measurements 58

5.1.4 Flux measurement 61

5.1.5 Limits on the dark matter annihilation cross-section 61

5.1.6 Conclusions 66

5.2 *Fermi*-LAT view of the inner Galaxy 66

5.2.1 Diffuse emission model uncertainties 67

5.2.2 Fitting procedure and preliminary results 69

5.2.3 Conclusions 70

The center of the Milky Way is the holy grail for DM searches since this region is predicted to be the closer and denser localized accumulation of DM in the galaxy, as already pointed out in 2.1.2. This region is also well known for the uncertainty in both, complex astrophysical processes and sources of gamma/cosmic rays, that confluence there. The *Fermi*-LAT has been detecting gamma rays in the direction of the GC since its launch in 2008, providing a better resolution and sensitivity in the GeV band compared to its predecessor, EGRET. Nevertheless, disentangle each contribution of the many sources that make up the GC view of the *Fermi*-LAT

require a deep understanding of those sources. Specially, if we are looking for a weak featureless contribution, as the one due to DM annihilation or decay, it can be easily mimic given our level of knowledge in modeling the other sources. Thus, interpretation in terms of DM of the gamma rays collected by the *Fermi*-LAT in the region surrounding the GC strongly depends on the modeling of the background emission. Many groups have claimed for a positive detection of a DM source in the GC, but they are data interpretations in the context of different background models hard to be proven independently. In this chapter we discuss our work [28] where we derive constraints on parameters of generic dark matter candidates by comparing theoretical predictions with the gamma-ray emission observed by the *Fermi*-LAT from the region around the GC. Our analysis is conservative since it simply requires that the expected dark matter signal does not exceed the observed emission.

In addition we present preliminary results on a novel analysis based on GALPROP [29]. [1], of the diffuse emission produced by known astrophysical sources.

5.1 Constraints on WIMP Annihilation for contracted DM in the Inner Galaxy with the *Fermi*-LAT

Astrophysical searches for dark matter (DM) are a fundamental part of the experimental efforts to explore the dark sector. The strategy is to search for DM annihilation products in preferred regions of the sky, i.e., those with the highest expected DM concentrations and still close enough to yield high DM-induced fluxes at the Earth. For that reason, the GC, nearby dwarf spheroidal galaxy (dSphs) satellites of the Milky Way, as well as local galaxy clusters are thought to be among the most promising objects for DM searches. In particular, dSphs represent very attractive targets because they are highly DM-dominated systems and are expected to be free from any other astrophysical gamma-ray emitters that might contaminate any potential DM signal. Although the expected signal cannot be as large as that from the GC, dSphs may produce a larger signal-to-noise (S/N) ratio. This fact allows us to place very competitive upper limits on the gamma-ray signal from DM annihilation [141, 142, 143], using data collected by the Large Area Telescope (LAT) onboard the Fermi gamma-ray observatory [19]. These are often referred to as the most stringent limits on DM annihilation cross-section obtained so far.

Despite these interesting limits derived from dSphs, the GC is still expected to be the brightest source of DM annihilations in the gamma-ray sky by several orders of magnitude. Although several astrophysical processes at work in the crowded GC

[1] A numerical code for cosmic-ray transport and diffuse emission production.

Profile	α	β	γ	ρ_s [GeV cm^{-3}]	r_s [kpc]
Einasto	0.22	$--$	$--$	0.08	19.7
NFW	1	3	1	0.14	23.8
NFW$_c$	0.76	3.3	1.37	0.23	18.5
Burkert	$--$	$--$	$--$	37.76	2

Table 5.1: DM density profiles used in this work, following the notation of Eqs. (2.2-2.4).

region make it extremely difficult to disentangle the DM signal from conventional emissions, the DM-induced gamma-ray emission is expected to be so large there that the search is still worthwhile. Furthermore, the DM density in the GC may be larger than what is typically obtained in N-body cosmological simulations. Ordinary matter (baryons) dominates the central region of our Galaxy [61]. Thus, baryons may significantly affect the DM distribution. As baryons collapse and move to the center they increase the gravitational potential, which in turn forces the DM to contract and increase its density. This is a known and qualitatively well understood physical process [52, 53, 54]. It is also observed in many cosmological simulations that include hydrodynamics and star formation [55, 56, 57, 58, 59, 60]. If this is the only effect of baryons, then the expected annihilation signal will substantially increase [61, 62].

In this work, we analyze in detail the constraints that can be obtained for generic DM candidates from *Fermi*-LAT inner Galaxy gamma-ray measurements assuming some specific (and well motivated) DM distributions. The approach is conservative, requiring simply that the expected DM signal does not exceed the gamma-ray emission observed by the *Fermi*-LAT in an optimized region around the GC. The region is chosen in such a way that the S/N ratio is maximized. This kind of analysis, without modeling of the astrophysical background, was also carried out by the *Fermi*-LAT collaboration to constrain DM models from Galactic halo observations [72].

5.1.1 DM density profiles

In Section 2.1.2 we already discussed general DM density profiles, paying special attention to the effect of baryonic compression. Here we discuss the followin models: Einasto, NFW, NFW compressed (NFW$_c$), and a cored Burkert profile, whose parameters have been constrained from observational data of the Milky Way. We have followed Ref. [61] to choose the parameters of both the NFW and the NFW$_c$. We fitted the resulting data of that work with the power-law parametrization of Eq. (2.2). The results for both profiles are listed in Table 5.1. The effect of baryonic

adiabatic compression is clearly noticed at small r as a steep power law $\rho \propto 1/r^{\gamma}$ with $\gamma = 1.37$ for NFW$_c$, which is in contrast to the standard NFW value, $\gamma = 1$. We note that a value of $\gamma = 1.37$ is indeed perfectly consistent with what has been found in recent hydrodynamic simulations [58] and it is also compatible with current observational constraints (mainly derived from microlensing and dynamics) on the slope of the DM density profile in the central regions of the Milky Way [70]. These studies actually allow for even steeper adiabatically contracted profiles. Concerning the Einasto profile we select the parameters provided in Ref. [71]. Finally, for the Burkert profile, we decided to choose a core radius of 2 kpc. This core size is in line with some works [72, 73] and with that suggested by recent hydrodynamic simulations of Milky Way size halos [74]. For the normalization of the profile we chose the value of the local density suggested in Ref. [71] for Milky Way Burkert-like profiles. The resulting profile is also compatible with current observational constraints [70]. Note, however, that a recent work favors a substantially larger core radius and a slightly higher normalization for Burkert-like profiles [75]. All the profile parameters are summarized in Table 5.1 and the four profiles are shown in Figure 5.1. It is easy to see that the models for the DM halo of our Galaxy differs substantially in their inner regions even when all of them fit the observed features of the Galaxy.

Let us finally point out that there are other possible effects driven by baryons that might steepen the DM density profiles in the centers of DM halos, such as central black holes (see e.g. Refs. [76, 77, 78]), that are not considered here.

5.1.2 DM induced gamma rays from WIMP annihilations

In Section 2.2.1 we presented how to model the gamma-ray flux from DM annihilation, taking into account the contributions from prompt photons and photons induced via inverse Compton scattering (ICS). The latter is specially relevant for the $\mu^+\mu^-$ channel.

In Figure 5.2, the $\bar{J}(\Delta\Omega)\Delta\Omega$ quantity corresponding to each of the four profiles discussed in the previous subsection is shown as a function of the angle Ψ from the GC. The associated observational regions $\Delta\Omega$ to each Ψ are taken around the GC. The angular integration is over a ring with inner radius of 0.5° and external radius of Ψ. We have assumed a $r = 0.1$ pc constant density core for both NFW and NFW$_c$, although as discussed e.g. in Refs. [90, 62] the results are almost insensitive to any core size below ∼1 pc (or even larger given the *Fermi*-LAT PSF). Remarkably, the adiabatic compression increases the DM annihilation flux by several orders of magnitude in the inner regions, i.e., the regions of interest in the present study. This effect will turn out to be especially relevant when deriving limits on the DM annihilation cross section. We also note that for the Burkert profile the value of $\bar{J}(\Delta\Omega)\Delta\Omega$ is larger than for the NFW and Einasto profiles. This is so because of

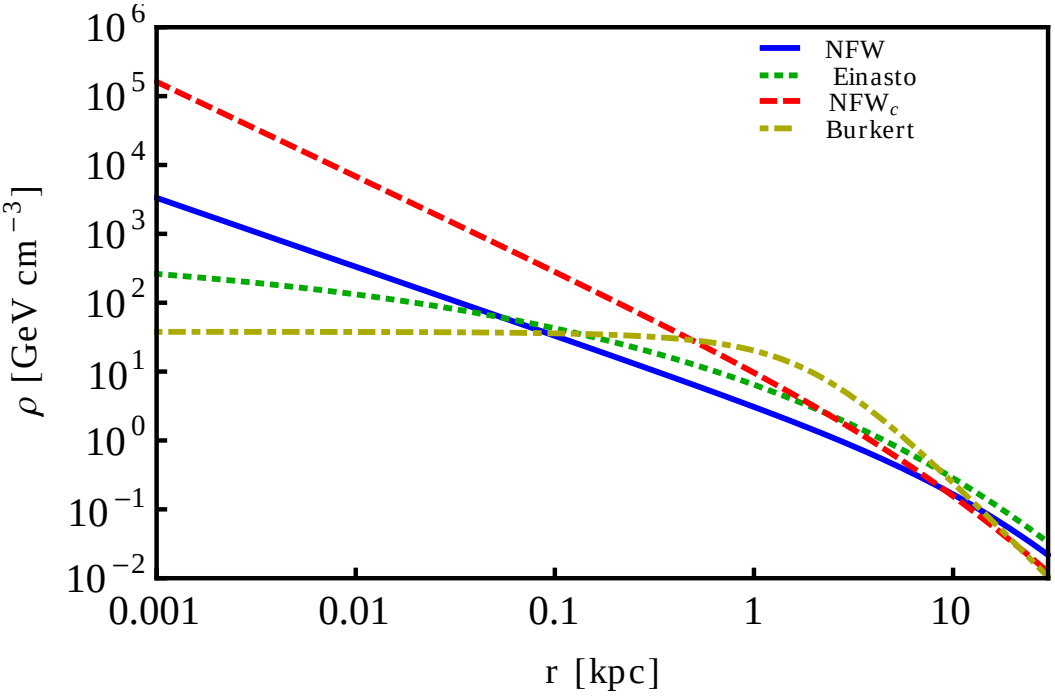

Figure 5.1: DM density profiles based on observational data of the Milky Way, the parameters are given in Table 5.1. Blue (solid), red (long-dashed), green (short-dashed) and yellow (dot-dashed) lines correspond to NFW, NFW$_c$, Einasto and Burkert profiles, respectively.

the relative high normalization used for this profile compared to the others and, especially, due to the annular region around the GC where we are focusing our studies, which excludes the GC itself (where such cored profiles would certainly give much less annihilation flux compared to cuspy profiles, see Figure 5.1). We note, however, that the use of another Burkert-like profile with a larger DM core than the one used here, as e.g., the one proposed in Ref. [75], may lead to substantially lower $\bar{J}(\Delta\Omega)\Delta\Omega$ values, and thus to less flux of DM-induced gamma rays. In particular, we checked for the profile in Ref. [75] that the values of $\bar{J}(\Delta\Omega)\Delta\Omega$ in the region shown in Figure 5.2 are always smaller than about 10^{22} GeV^2 cm^{-5} sr. Notice finally that the NFW$_c$ profile reaches a constant value of $\bar{J}(\Delta\Omega)\Delta\Omega$ for a value of Ψ smaller than the other profiles. This is relevant for our discussion below on optimization of the region of interest for DM searches, since we see that for NFW$_c$ a larger region of analysis will not increase the DM flux significantly as for NFW, Einasto and Burkert profiles.

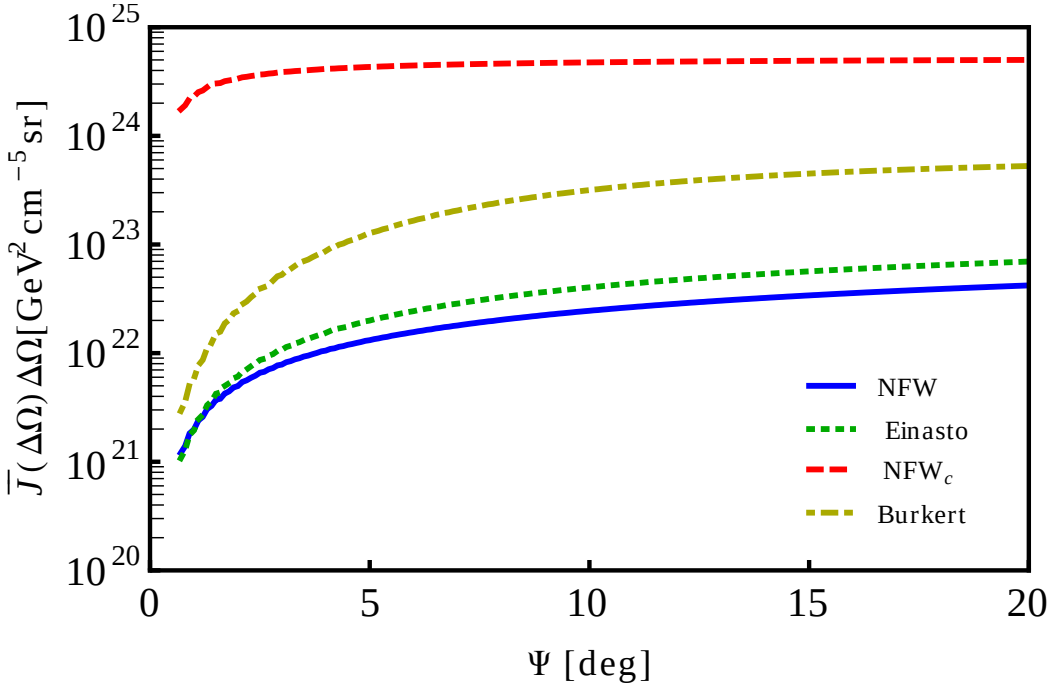

Figure 5.2: The $\bar{J}(\Delta\Omega)\Delta\Omega$ quantity integrated on a ring with inner radius of 0.5° (~ 0.07 kpc) and external radius of Ψ ($R_\odot \tan\Psi$) for the DM density profiles given in Table 5.1. Blue (solid), red (long-dashed), green (short-dashed) and yellow (dot-dashed) lines correspond to NFW, NFW$_c$, Einasto and Burkert profiles, respectively. The four DM density profiles are compatible with current observational data.

5.1.3 Gamma-ray flux from *Fermi*-LAT measurements

5.1.3.1 Data selection and processing

In our analysis we use the LAT photon data measured between August 4, 2008, and June 15, 2012, in the energy range between 1 GeV and 100 GeV. Events with zenith angles < 100° are selected to reduce the contamination by gamma-ray emission coming from cosmic-ray interactions in the atmosphere. We select events from the P7ULTRACLEAN_V6::FRONT class. This choice reduces the cosmic-ray background contamination and takes advantage of a narrower PSF as compared to back-converting events. We make a reasonable assumption on systematic uncertainty extending it from Source and Clean classes. The systematic uncertainty of the effective area for both Source and Clean class events is quoted as 10% at 100 MeV, decreasing to 5% at 560 MeV, and increasing to 20% at 10 GeV and above [30]. Maps of flux for different energy ranges from a region of 30° around the GC

is made using version V9r28 of the LAT Science Tools [2]. As we will show below, we can use a single flux map (built summing up the flux maps for the different energy ranges) to select the Region Of Interest (ROI) with the aim of maximizing the S/N ratio for each individual DM profile under study.

5.1.3.2 Optimization of the region of interest for dark matter searches

An important step in our analysis is the optimization of the ROI using a data-driven procedure that maximizes the S/N ratio. In order to do so, we follow a procedure similar to the one presented in the appendix A of [26]:

1. We produce $40^\circ \times 40^\circ$ maps centered on the GC of the quantity $\bar{J}(\Delta\Omega)\Delta\Omega$ for the four DM density profiles considered (i.e., Einasto, NFW, NFWc and Burkert) and use them as signal. Each pixel i has an area of $0.2^\circ \times 0.2^\circ$ and contains a J-factor value J_i calculated with Eq. (2.15).

2. We use as noise the square root of the observed photon flux integrated in the energy range 1-100 GeV. We use a single map, instead of a different one for each energy bin since the morphology of the background does not exhibit strong variations in energy. The flux in pixel i is labelled as F_i.

3. A mask, defined by three angles θ_1, θ_2 and $|b|$ as shown in Figure 5.3, is introduced to cover the GC, the Galactic plane, and the high galactic latitude regions, where the statistical fluctuations of the Galactic foreground dominate over the expected DM signal.

4. The optimization procedure consists of finding the set of angles that mask a region such that the S/N ratio is the largest for each DM profile considered. What we technically do is to minimize the inverse of the following quantity

$$S/N = \frac{\sum_i J_i}{\sqrt{\sum_i F_i}} \tag{5.1}$$

   with i running over unmasked pixels, varying masks. We use the numerical routine `Fmin` of the Python module `scipy.optimize` [3], which minimizes a function using the downhill simplex algorithm. We end up with four masks characterized by those angles given in Table 5.2. In the same Table, we also show the values of $\Delta\Omega$ and $\bar{J}(\Delta\Omega)\Delta\Omega$ for each profile. As expected, $\theta_1 = |b|$ for all the profiles, since the broadest emission in the Galactic plane is the one in

[2] `http://fermi.gsfc.nasa.gov/ssc/data/analysis/software/`
[3] http://docs.scipy.org/doc/scipy/reference/optimize.html#

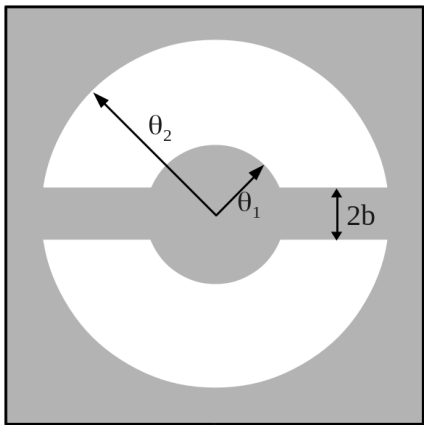

Figure 5.3: Schematic view of our choice of the ROI. The gray area represents the masked region.

Figure 5.4 shows the ROI that we have obtained for each DM density profile in Table 5.1. Clearly, the NFW$_c$ ROI is the smallest one. This can be easily understood by inspecting the Figure 5.2: the $\bar{J}(\Delta\Omega)\Delta\Omega$ quantity for NFW$_c$ becomes almost constant beyond only 5°, whereas for the other profiles this quantity becomes flat at much larger radii. Therefore, in the case of the NFW$_c$ profile, increasing the angular aperture by a few more degrees does not increase the S/N.

Note that the usual quantities to calculate S/N ratios are observed counts and expected DM-induced counts but in this work, instead, we use observed gamma-ray flux (rather than counts) and J-factors (formally proportional to the expected DM-induced gamma-ray flux). Nevertheless, we checked that the use of observed fluxes and predicted J-factors turns out to be a very good approximation, which leads to similar optimized ROIs. We performed the following test. Using the gtobssim tool and assuming the NFW profile, we simulated the events that different DM models could produce in the LAT after 46 months of observation. We used the same IRFs, cuts and procedure to select events as those used for the real observations. Instead of using a fixed 1 – 100 GeV energy range we further optimize this quantity choosing an energy range centered around the DM emission peak. We then compare the simulated DM counts maps and the actually observed counts map in the given energy range to re-derive the optimized S/N region. As anticipated above we find that the derived ROI's parameters using counts maps do not change significantly for different DM models from those calculated using observed fluxes and J-factors and a fixed energy range.

Profile	θ_1 [°]	θ_2 [°]	$\lvert b\rvert$ [°]	$\Delta\Omega$ [sr]	$\bar{J}(\Delta\Omega)\,\Delta\Omega$ [$\times 10^{22}$ GeV^2 cm^{-5} sr]	Flux (1 − 100 GeV) [$\times 10^{-7}$ cm^{-2}s^{-1}]
Burkert	0.8	15.9	0.8	0.225	41.9	32.1 ± 0.3
Einasto	0.7	15.6	0.7	0.217	5.1	31.4 ± 0.3
NFW	0.6	16.7	0.6	0.253	3.3	38.0 ± 0.3
NFW$_c$	1.0	3.0	1.0	0.005	86.8	2.2 ± 0.1

Table 5.2: The optimized regions for the DM density profiles studied, defined by the angles shown in Figure 5.3. The corresponding values for $\Delta\Omega$, $\bar{J}(\Delta\Omega)\Delta\Omega$, and observed flux with statistical errors only (in the energy range between 1 − 100 GeV) are also shown.

5.1.4 Flux measurement

Following the analysis described above, we show in Figure 5.4 the flux observed by the *Fermi*-LAT, and the ROIs corresponding to each of the DM profiles considered. The value of this flux integrated in the energy range 1 − 100 GeV can be found in the last column of Table 5.2. The energy spectra from the ROI associated to each profile are shown in Figure 5.5. We limit the energy range of the analysis to be below 100 GeV in order to have a small statistical uncertainty in each bin, falling generally below the systematic uncertainty. In this way we remove the possibility for the upper limits to be accidentally dominated by a large downward fluctuation in the energy bins close to the peak of the gamma-ray emission from DM annhilation, which is the most constraining point when comparing to the measured flux.

To set constraints we require that the DM-induced gamma-ray flux does not exceed the flux upper limit (UL) evaluated as follows. We set 99.98% UL signal counts using the Bayesian approach presented in Ref. [144], for the case of absence of background with systematic uncertainties not included, which correctly takes into account the Poisson limit (i.e. the case of low counts). Using exposure maps calculated with the gtexpcube2 tool of the Science Tools we are able to convert UL signal counts into the UL signal flux needed to set constraints.

5.1.5 Limits on the dark matter annihilation cross-section

As already discussed, we adopt a conservative approach in the analysis of the limits on the DM annihilation cross section, simply requiring that the integrated gamma-ray flux of the expected DM signal for each energy bin does not exceed the upper limit signal flux evaluated following the Bayesian procedure in Ref. [144][4]. We do

[4]It is worth noting that even though we optimize the ROIs based on both, DM and observed distributions, to set limits on DM annihilation cross section we perform a spectral analysis. It

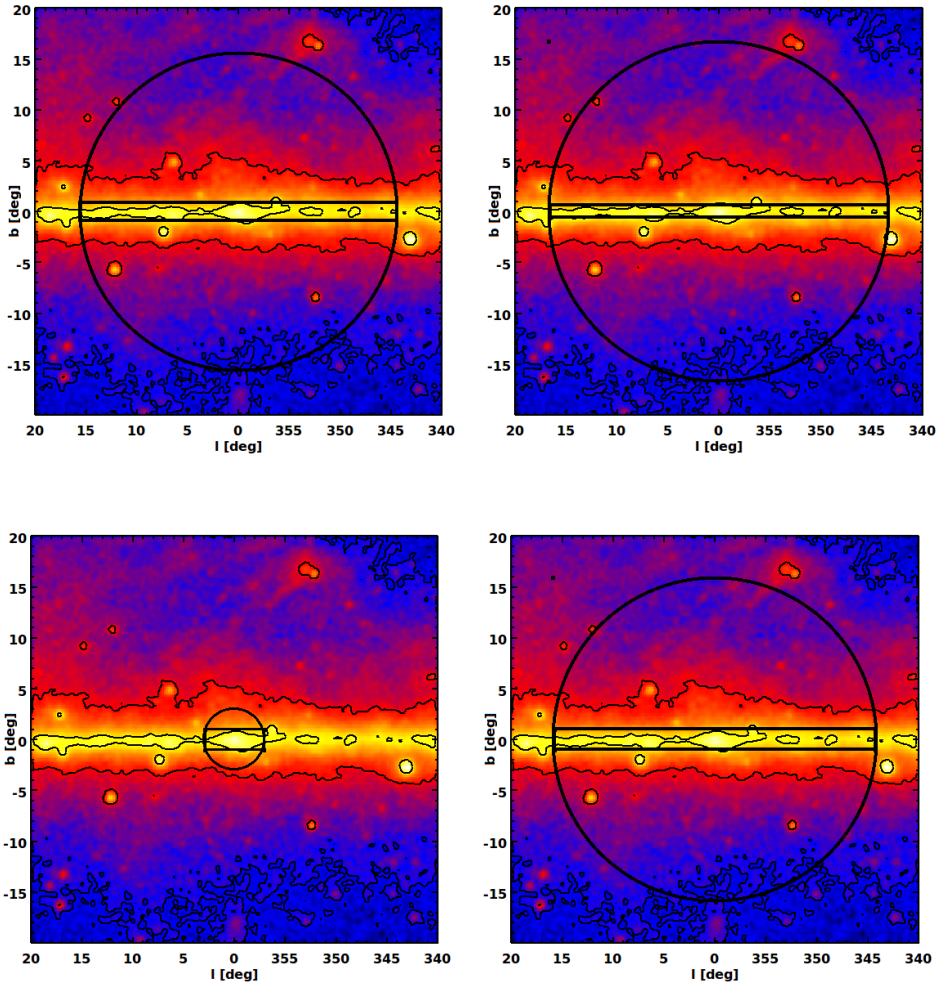

Figure 5.4: Maps of the observed flux by the *Fermi*-LAT in the energy range $1 - 100$ GeV, in units of photons cm^{-2} s^{-1}, for the four DM profiles studied. Upper left: Einasto, upper right: NFW, bottom left: NFW$_c$, and bottom right: Burkert. For each profile, the ROI is the region inside the circle excluding the band on the Galactic plane. Color scale is logarithmic, yellow, red and blue correspond to 3.6×10^{-9}, 6.4×10^{-10} and 1.2×10^{-10} photons cm^{-2} s^{-1}, respectively. These values also correspond to black contours. In order to reduce statistical noise and to bring up finer features in the inner galaxy the map is smoothed with a 0.2° FWHM Gaussian function.

not subtract any astrophysical background.

would be interesting for a future work to check that at the upper limit cross sections derived here, the implied spatial distribution of the gamma-ray signal intensity does not significantly exceed the data anywhere within the ROI at any energy.

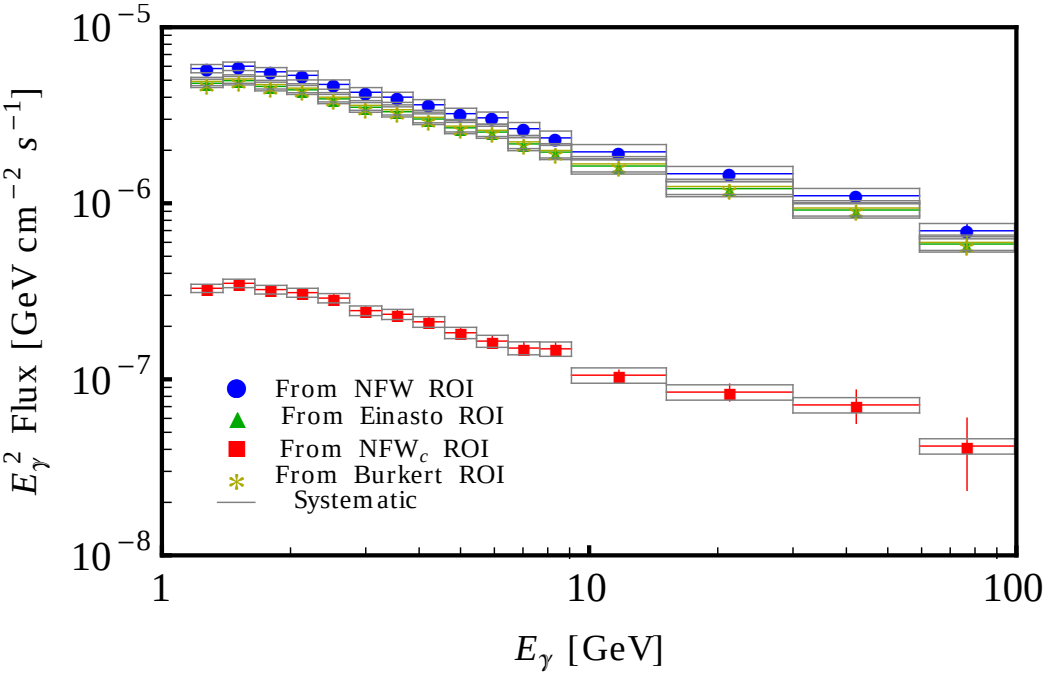

Figure 5.5: Energy spectra extracted from *Fermi*-LAT data for the optimized regions that are shown in Figure 5.4. Data are shown as points and the vertical error bars represent the statistical errors. The latter are in many cases smaller than the point size. The boxes represent the systematic error in the *Fermi*-LAT effective area.

We present the results in Figure 5.6, where the constraints obtained are shown for different final states. There we also illustrate the case $\langle\sigma v\rangle = 3\times10^{-26}$ cm^3 s^{-1}, which corresponds to the value of the annihilation cross-section associated to the correct thermal relic abundance for a WIMP whose annihilation is dominated by the s-wave (velocity-independent) contribution and thus, $\Omega_{DM}\, h^2 \approx 3\times10^{-27}$ cm^3 s^{-1} $\langle\sigma v\rangle^{-1} \approx 0.1$ [145]. For comparison, the constraints are given considering only the contribution from prompt gamma rays and the total contribution from prompt plus ICS gamma rays.

First, it is worth noting that if the DM density follows an Einasto, NFW or Burkert profile, the upper limits on the annihilation cross section are above the value of the thermal cross-section for any annihilation channel. Nevertheless, the situation is drastically different when we consider the DM compression due to baryonic infall in the inner region of the Galaxy. Indeed, by adopting the NFW$_c$ profile and for a $b\bar{b}$, $\tau^+\tau^-$ and W^+W^- channel, the thermal annihilation cross-section is already reached for a DM mass of 680, 530 and 490 GeV, respectively. For the $\mu^+\mu^-$ channel the effect of the prompt gamma rays is less important since generally

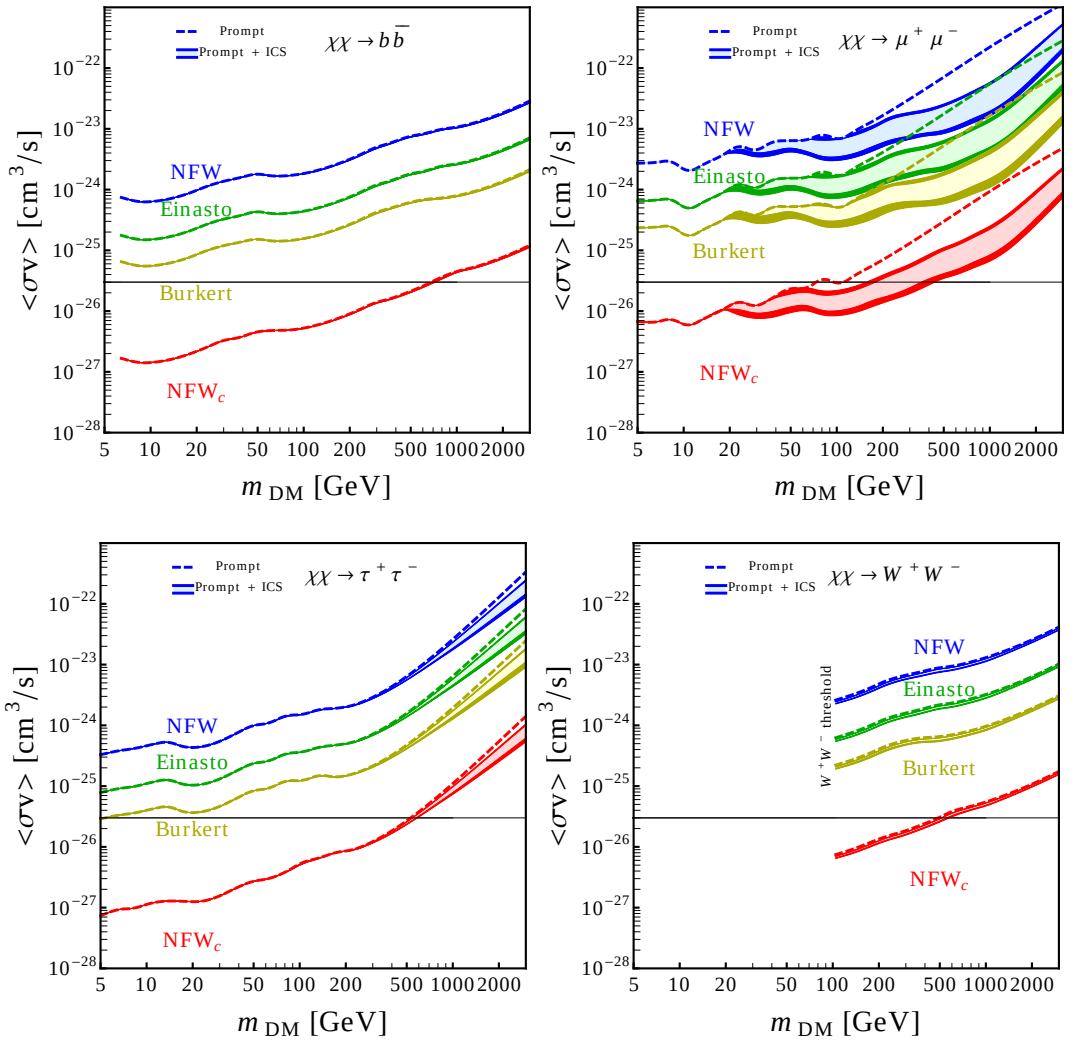

Figure 5.6: 3σ upper limits on the annihilation cross-section of models in which DM annihilates into $b\bar{b}$, $\mu^+\mu^-$ (upper panel), $\tau^+\tau^-$ or W^+W^- (lower panel), for the four DM density profiles discussed in the text. Upper limits set without including the ICS component in the computation are also given as dashed curves (prompt) for comparison. The uncertainty in the diffusion model is shown as the thickness of the solid curves (from top to bottom: MIN, MED, MAX) while the lighter shaded regions represent the impact of the different strengths of the Galactic magnetic field with lower(higher) values of the cross-section corresponding to $B_0 = 1\ \mu$G($B_0 = 10\ \mu$G). The horizontal line corresponds to the expected value of the thermal cross-section for a generic WIMP candidate.

fewer photons are produced in the FSR compared to the hadronic decays of the other channels. (For the W^+W^- which is open when $m_{DM} \gtrsim 90$ GeV, the $W^\pm$ decays produce a large number of photons, especially at high energy). Notice that the

lower bound associated with prompt gamma rays for $\mu^+\mu^-$ is 100 GeV compared to about 500–700 GeV in the other channels. Thus the ICS is important in this case, also due to the relatively harder $e^{\pm}$ spectrum [82]. We can see that for $B_0 = 1\ \mu$G the lower bound on the DM mass turns out to be 358 GeV and for $B_0 = 10\ \mu$G the bound is 157 GeV, using the MIN diffusion model. For MED and MAX diffusion models the values turn out to be 404, 171 GeV and 439, 179 GeV, respectively. As discussed in Subsection 2.2.1, when the magnetic field is stronger the energy of the injected $e^{\pm}$ is more efficiently liberated in the form of microwaves, resulting in a softer gamma-ray spectrum, and producing therefore lower constraints . Therefore, we have shown that in those cases in which the ICS component is dominant (for heavy WIMP masses in general), the variation of the magnetic field can significantly alter the expected gamma-ray fluxes from the inner regions of the Galaxy.

Although the above results can be interpreted in general as implying that vanilla WIMP models and contracted DM profiles are incompatible with the Fermi data, one should keep in mind that if one works in the framework of a specific particle physics model this conclusion might in principle be avoided in some regions of the parameter space. For example, the final state can be a combination of the annihilation channels presented here, as in supersymmetry where the lightest neutralino annihilation modes are 70% $\bar{b}b$ − 30% $\bar{\tau}\tau$ for a Bino DM, and 100% W^+W^- for a Wino DM (or for a Higgs-portal model). More importantly, the value of the annihilation cross section in the Galactic halo might be smaller than 3×10^{-26} cm^3 s^{-1} for a DM candidate that is thermally produced. For example, in the early Universe coannihilation channels can also contribute to $\langle\sigma v\rangle$. Also, DM particles whose annihilation in the early Universe is dominated by p-wave (velocity-dependent) contributions would have a smaller value of $\langle\sigma v\rangle$ in the Galactic halo, where the DM velocity is much smaller than at the time of freeze-out, and can therefore escape the constraints derived in this work. These two effects can in fact occur in some regions of the parameter space of well motivated models for particle DM, such as the neutralino. In this sense, the results derived above for pure annihilation channels can be interpreted as limiting cases that give an idea of what can happen in realistic scenarios.

Let us remark that the upper limits on the annihilation cross-section that we have obtained for the cases of NFW, Einasto and Burkert profiles are comparable to the ones previously reported by the *Fermi*-LAT collaboration [72], after a similar analysis of the Galactic halo without modeling of the astrophysical background (similar results were also obtained in Ref. [146, 147]). Modeling of the background was also considered in Ref. [72], and the results are competitive with those from dSphs [141, 142, 143], where the upper limit of the annihilation cross section is below the thermal one for DM masses smaller than 27 and 37 GeV assuming a $b\bar{b}$ and a $\tau^+\tau^-$ channel, respectively.

Remarkably, when we take into account the baryonic infall in our conservative

analysis, forcing the DM to contract in those inner regions of the Galaxy, we obtain much stronger limits. In particular, as discussed above, using our compressed DM density profile, NFW$_c$, the thermal cross section is excluded for a DM mass smaller than 680 and 530 GeV in the $b\bar{b}$ and $\tau^+\tau^-$ channel, respectively, thus improving those limits obtained from dSphs [141, 142, 143], and also those obtained from galaxy clusters [148]. In the latter, DM masses smaller than about 100 GeV are constrained provided that DM subhalos significantly contribute to boost the DM signal. In general, the upper limits on the DM annihilation cross section are two orders of magnitude stronger than without contraction. In recent works on the GC a similar analysis was carried out but subtracting the emission from known point sources and from the Galactic disk [149, 73].

5.1.6 Conclusions

We derived constraints on the parameter space of generic DM candidates using *Fermi*-LAT inner Galaxy measurements. We considered well motivated DM density profiles, such as Burkert, Einasto and NFW, which are perfectly compatible with current observational data of the Milky Way. We then selected optimal regions around the GC, such that the S/N ratio is maximized. When the effect of contraction in the DM halo due to baryons is included in the computation [61, 62], the constraints turn out to be very strong. In particular, a compressed DM density profile allows us to place upper limits on the DM annihilation cross section that exclude the thermal cross section for a broad range of DM masses, as shown in Figure 5.6. This is the case for masses smaller than 680, 530 and 490 GeV for $b\bar{b}$, $\tau^+\tau^-$ and W^+W^- channels, respectively. For the $\mu^+\mu^-$ channel, where the ICS effect is important, the exclusion of the thermal cross-section is for a mass smaller than about 150 to 400 GeV, depending on models of the Galactic magnetic field. Alternatively, one may interpret these results as implying that vanilla WIMP models and contracted DM profiles are incompatible with the *Fermi* data.

Although the constraints are very strong, the analysis is conservative since we require that the expected DM signal does not exceed the gamma-ray emission observed by the *Fermi*-LAT, and modeling of the astrophysical background is not carried out. The latter would only lead to better constraints on the DM annihilation cross section.

5.2 *Fermi*-LAT view of the inner Galaxy

The emission detected in the direction of the inner Galaxy is made of: outer Galaxy, true inner Galaxy, unresolved sources, point or small extended sources, extragalactic emission, possible DM contribution, and cosmic-ray instrumental background;

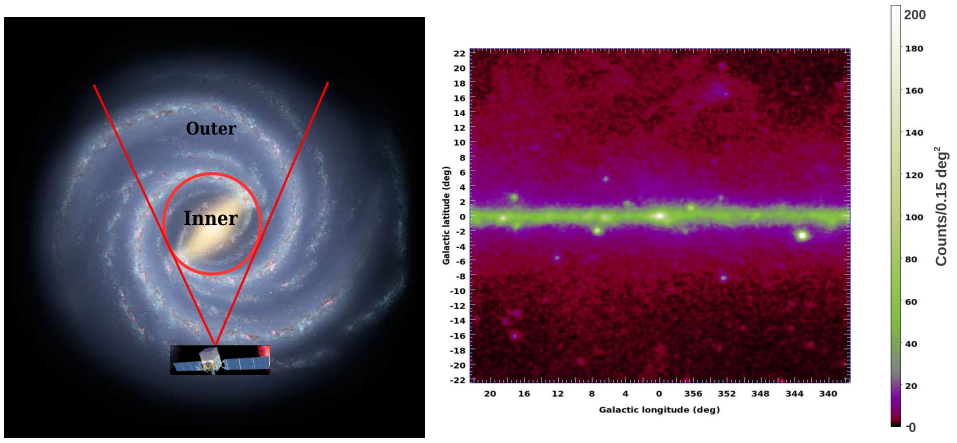

Figure 5.7: Left: Schematic of the GC view with the *Fermi*-LAT. Right: Data counts with energy larger than 1 GeV collected in ∼ 32 months in the direction of the GC.

see figure 5.7. Here we are interested in the standard astrophysical production of the high-energy gamma-ray diffuse emission, therefore we model the diffuse emission created by interaction of cosmic rays with interestellar gas (pion decay and bremsstrahlung), radiation fields (ICS), and magnetic fields (synchrotron). To build diffuse emission models of the inner Galaxy we use GALPROP[5]. This code calculates the propagation of cosmic rays, and computes diffuse gamma-ray emission in the same framework. Each run of the code is governed by a configuration file. Thus, each run corresponds to a potentially different model.

5.2.1 Diffuse emission model uncertainties

The GALPROP code uses realistic astrophysical inputs together with theoretical models. Each run needs a specific set of those parameters. The gas-related gamma-ray intensities calculated from the emissivities using the column densities of HI LAB survey and composite CO survey for Galactocentric rings. The ICS is treated using the formalism for an anisotropic radiation field developed by Moskalenko & Strong in [150] and uses a model for ISRF. Other parameters for a given GALPROP model are the CR primary injection spectra, the spatial distribution of CR sources, the size of the propagation region, the spatial and momentum diffusion coefficients and the Galactic magnetic field model. All these parameters have uncertainties associated, in the following we go deeper into some of them.

[5]For a detailed description of the GALPROP code and the most recent release that we use in this work (version 54), we refer the reader to the dedicated website `http://galprop.stanford.edu`

5.2.1.1 Molecular Hydrogen H2

Concentrated mostly in the plane. The main tracer is CO. Distance information from velocity and a rotation curve is used to assign the gas to galactocentric rings. The standard method of assigning velocity to distance, in order to create the rings, breaks down toward the galactic center. More details in 5.2.1.3. The so call Xco factor to convert CO to H2 column density is believed to vary as a function of the galactocentric radius. However, the exact form of the variation is not well know.

5.2.1.2 Atomic Hydrogen HI

The 21 cm line HI used is from [151]. As for H2 distance information from velocity and a rotation curve is used to assign the gas to galactocentric rings. The main uncertainty come from the spin temperature T_s. We adopt a single T_s = 150 K among many possibilities. Indeed, HI is a mixture of various phases, observations of T_s show it to vary from tens of K up to thousands of K, so that the adoption of a single T_s is in any case an approximation.

5.2.1.3 Galactocentric rings toward the GC

The kinematic resolution of the method used to relate velocity and distance vanishes for directions near the GC. We linearly interpolate each annulus independently across the range $|l| < 10^\circ$ to get an estimate of the radial profile of the gas. Nevertheless, the innermost annulus is entirely enclosed within the interpolated region, necessitating a different method to estimate its column density. For HI the innermost annulus contains 60% more gas than its neighbouring annulus. This is a conservative number. For CO, we assign all high velocity emission in the innermost annulus. See Appendix 2 of [81] for more details.

5.2.1.4 Interstellar Radiation Field (ISRF)

Emission from stars, and the scattering, absorption, and re-emission of absorbed starlight by dust in the ISM.The `FRaNKIE` radiation transport code [152] is used to model the distribution of optical and infrared (IR) photons throughout the Galaxy. Further details about the ISRF model used in this analysis and recent developments about modelling this component, can be found in Appendix 3 of [81]. The main uncertainty is the overall input stellar luminosity and how it is distributed amongst the components of the model (bulge, thin and thick disk, and halo)

5.2.1.5 Cosmic-Ray injection and propagation

SNRs are widely accepted as the main sources of CRs. However, their distribution is not well determined. Pulsars are SN explosion end state and its distribution is

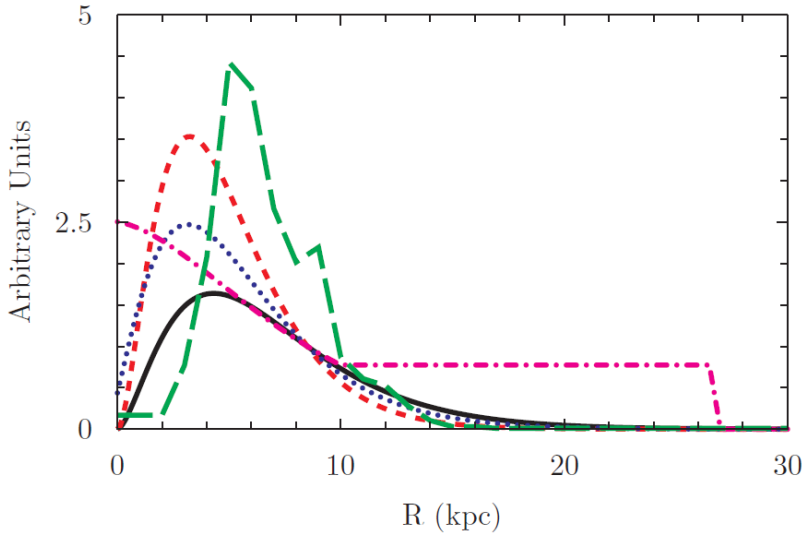

Figure 5.8: Primary CR nuclei and electron source distribution for the large-scale diffuse Galactic model (dot-dashed line) compared with those used in [81]. Solid, SNR [153]; short-dashed, pulsars [154]; dotted, pulsars [155]; long-dashed, OB-stars [156]

better determined than SNRs, but still, it suffers from observational bias. CR propagation is not well known and its uncertainties involve spectra injection, transport parameters, halo size, etc. In figure 5.8 we present the distribution of cosmic rays used in this work in comparison with other distributions widely used, as e.g. in [81].

5.2.2 Fitting procedure and preliminary results

In this work we assume that foreground and background (see figure 5.7) region can be relatively well modelled. We also assume that the emission from the inner Galaxy region is brighter than foreground/background emissions. The analysis begin with the construction of an all sky diffuse galactic model based on the GALPROP code with the model parameters adjusted to provide a good representation of the whole sky *Fermi*-LAT data. Although this diffuse model is not unique, since the models in [81] also give a good agreement to the data, this is not a problem for our analysis of the inner Galaxy region. One important result in the study [81] was that a scaling factor for the ICS emission is needed to account for the data, this factor is model dependent and vary according to the region of the sky. In particular, toward the inner Galaxy it was found that the models considered in that study tended to underpredict the ICS intensity. This increase in the ICS intensity is distributed over a larger region than our ROI ($15^\circ \times 15^\circ$ about the GC) and is not associated

with localised emissions. In order to study this additional background component we used the ICS intensity sky map toward the inner Galaxy as a template and fit for the enhancement factor over the larger $45^\circ \times 45^\circ$ region about the GC, we find the ICS factor to be ~ 2. Then we focus on the $15^\circ \times 15^\circ$ region where we fit for enhance gas-related emission using the π^0-decay intensity maps for the inner gas rings 1-3 for HI and the inner most C0 ring 1. Figure 5.9 shows preliminary results. After subtraction of a physically-motivated model based on GALPROP from the *Fermi*-LAT data, the residual is compatible with detected point sources and small fluctuations (upper right panel in 5.9). Further investigations are going on in the collaboration in order refine this preliminary results. The new analysis using an iterative fitting procedure to characterise the data according to the contributions by discrete and diffuse sources is able to account for approximately 97% of the gamma-ray emissions from the $15^\circ \times 15^\circ$ about the GC in terms of diffuse emission models from standard astrophysical processes, point sources, and sub-detection threshold candidates (lower panel in 5.9). Of the remaining gamma-ray emissions, approximately 3% can be attributed to a low-intensity component. However, further study is required to properly characterise the spatial and spectral properties of these residual emissions.

5.2.3 Conclusions

The majority of the diffuse emission is removed using a physically-motivated model based on GALPROP. The diffuse model subtraction yield spatial residuals in $45^\circ \times 45^\circ$ about the center of the galaxy consistent with known point sources and small fluctuations. Preliminary results from *Fermi*-LAT show that most of the emission from a $15^\circ \times 15^\circ$ region around the direction of the Galactic center can be modeled in terms of diffuse emission and point sources. The major conclusion of these works is that our knowledge of the conventional astrophysical background is uncertain. This is currently a big limitation for the search of DM in the Galactic center with gamma rays, which otherwise has huge potential for discovery or for setting constraints. Papers are forthcoming and will include DM results.

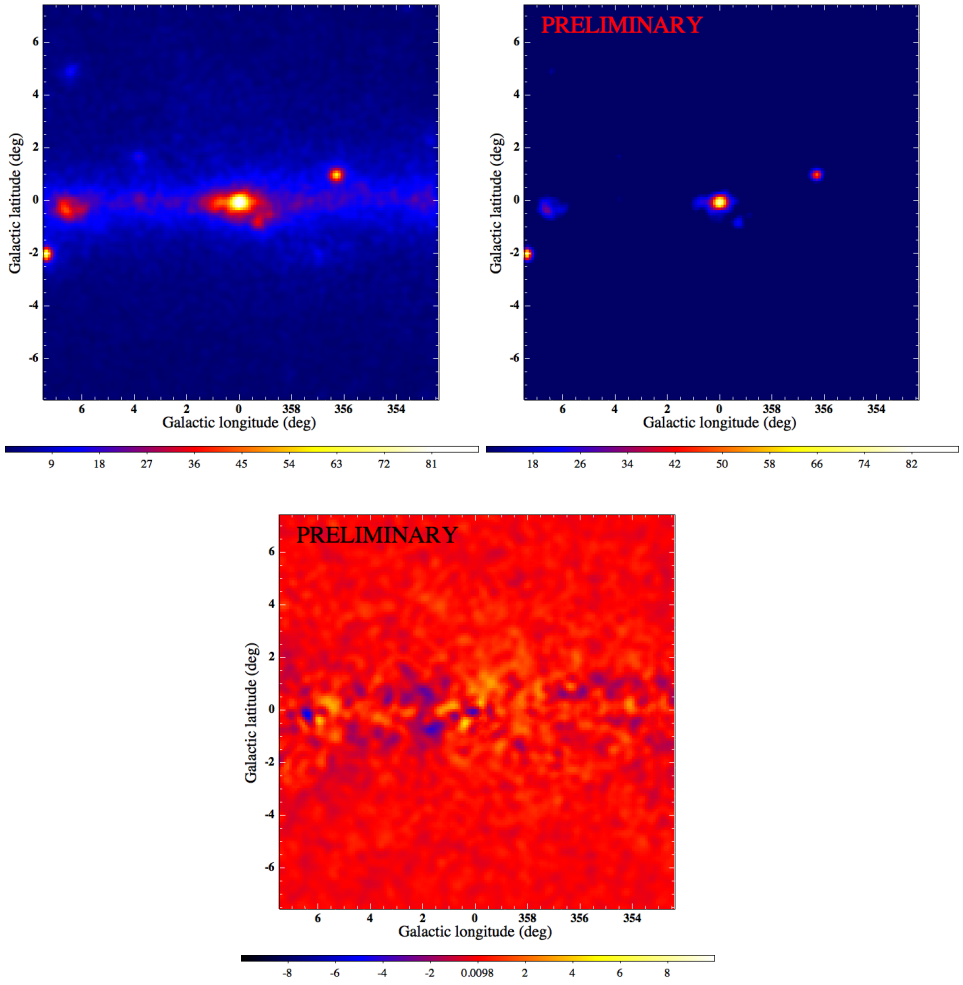

Figure 5.9: Upper left: Fermi's view of the 15° × 15° region center on the GC. Pass 7 front photons with energy larger than 1 GeV. Upper right: Bright excesses after subtracting diffuse emission model are consistent with known sources. Lower panel: Diffuse emission and point sources account for most of the emission observed in the region.

Chapter 6

Measurement of anisotropies in the gamma-ray diffuse background: DM signal and background

The Aleph's diameter was probably little more than an inch,
but all space was there, actual and undiminished.
Jorge Luis Borges, *The Aleph*.

Contents

6.1 *Fermi*-LAT measurement of anisotropies in the IGRB 74
6.1.1 The angular power spectrum (APS) as a metric for anisotropy 75
6.1.2 Method 75
6.1.3 Results and conclusions 76
6.2 DM implications of *Fermi*-LAT measurement of anisotropies in the IGRB 78
6.2.1 DM predictions 78
6.2.2 Setting constraints 79
6.2.3 Preliminary results 79

The diffuse gamma-ray background is characterized by an isotropic or nearly isotropic distribution and is therefore known as the Isotropic Gamma-ray Background (IGRB) [21]. It is constituted by gamma rays produced by various sources, including blazars, pulsars, and possible DM structures, not yet detected due to the limited angular resolution and photon statistics of the Fermi-LAT. Figure 6.1 shows the IGRB spectrum and the estimated contributions from unresolved blazars, star-forming and radio galaxies. Even so, the detailed origin of the IGRB is still unknown. The contribution of unresolved sources is expected to induce small-scale anisotropies in this emission, which may provide a way to identify and constrain the properties of its contributors. Recent studies have predicted the contributions to the angular power spectrum (APS) from extragalactic and galactic DM annihilation or decay, therefore the detailed structure of the universe might be imprinted in

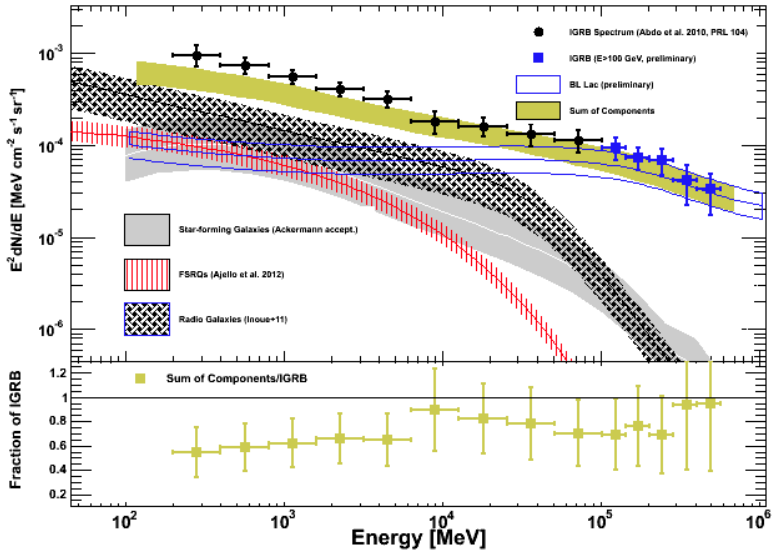

Figure 6.1: IGRB spectrum and the contribution from all the different extragalactic source classes that have been detected by Fermi. The golden band shows the sum of all the source populations. By summing all contributions it is apparent that there is still room for other components at all energies within the uncertainties [157]. See also [158] for other theoretical estimates of the relative contributions of unresolved blazars and star-forming galaxies to the IGRB.

the anisotropies of the IGRB. The Fermi-LAT collaboration reported detection of angular power with a significance larger than 3σ in the energy range from 1 GeV to 10 GeV on 22 months of data [30]. In this chapter we present that APS measurement, as well as a comparison to the accurate predictions for DM anisotropies from state-of-the-art cosmological simulations as presented in [33] to derive constraints on different DM candidates.

6.1 *Fermi*-LAT measurement of anisotropies in the IGRB

We present the results of an anisotropy analysis of the extragalactic diffuse emission measured by the Fermi-LAT. We calculate the angular power spectrum of the emission from $\sim$ 22 months of Fermi data and of the emission from a simulated model (galactic diffuse emission, 11-month sources from Fermi catalog and isotropic emission), and compare the results from the data and model in order to identify significant differences in anisotropy properties.

6.1.1 The angular power spectrum (APS) as a metric for anisotropy

We consider the APS C_l of intensity fluctuations,

$$\delta I(\psi) = \frac{I(\psi) - \langle I \rangle}{\langle I \rangle}, \tag{6.1}$$

where $I(\psi)$ is the intensity in the direction ψ. The APS is given by $C_l = \langle |a_{lm}|^2 \rangle$, where a_{lm} are determined by expanding (6.1) in spherical harmonics, $\delta I(\psi) = \sum_{l,m} a_{lm} Y_{lm}$.

The $1 - \sigma$ statistical uncertainty in the measured APS is given by

$$\delta C_l = \sqrt{\frac{2}{(2l+1)\Delta l f_{sky}}} \left(C_l + \frac{C_N}{W_l^2} \right), \tag{6.2}$$

where W_l =exp$(-l^2\sigma_b^2/2)$ is the window function of a Gaussian beam of width σ_b. f_{sky} is the fraction of the sky observed and Δl multipole bins. The noise power spectrum C_N is the Poisson noise, $C_N = (4\pi f_{sky})/N_\gamma$, where N_γ is the number of photons observed.

Predicted values of C_l at $l = 100$ of various USP cover a large range, e.g., $\sim 1 \times 10^{-4}$ for blazars [170], $\sim 1 \times 10^{-7}$ for starforming galaxies [171] , and $\sim 1 \times 10^{-4}$ to 1 for DM [162, 163, 164, 165, 166, 167, 168, 169].

6.1.2 Method

The first 22 months of Fermi-LAT data were analyzed, dividing the energy range between 1 GeV and 50 GeV in 4 energy bins. The point sources in the first year catalogue [159] have been masked, as well as the emission within a band of 30 degrees above and below the Galactic plane. The masking was done to cover the regions in the sky where the emission is dominated by resolved sources and by the Galactic foreground, and to restrict the analysis only to where the IGRB is a significant component. See the maps used in figure 6.2. Then we follow these steps:

- Calculate angular power spectrum of the data in energy bins using the HEALPix package [172]
- Focus on multipoles greater than 100 (angular scales $\lesssim 1 - 2^\circ$), because the contamination from Galactic diffuse is likely to be small
- Compare results from data and simulated model to identify significant differences in anisotropy properties.

E_{min} GeV	E_{max} GeV	C_P $[(\mathrm{cm}^{-2}\mathrm{s}^{-1}\mathrm{sr}^{-1})^{-2}\ \mathrm{sr}]$	Significance -	$C_P/\langle I\rangle^2$ $[10^{-6}\ \mathrm{sr}]$	Significance -
1.04	1.99	$4.62 \pm 1.11 \times 10^{-18}$	4.2σ	6.38± 1.53	4.2σ
1.99	5.00	$1.30 \pm 0.22 \times 10^{-18}$	6.0σ	6.90± 1.16	5.9σ
5.00	10.4	$8.45 \pm 2.46 \times 10^{-20}$	3.4σ	8.37± 2.41	3.5σ
10.4	50.0	$2.22 \pm 0.86 \times 10^{-20}$	2.4σ	7.27± 3.36	2.2σ

Table 6.1: Best-fit values of the angular power C_P and fluctuation angular power $C_P/\langle I\rangle^2$ in each energy bin over the multipole range for the cleaned data.

- Estimate $1-\sigma$ statistical uncertainty in the measurement; systematic uncertainties NOT included

We used P6_V3 instrument response, for data and simulations. Maps binned into order 9 HEALPix, which implies a pixel size of 0.125°. The simulated data are produced using `gtobssim` routine part of the Fermi Science Tools package. We used current background models released by the Fermi collaboration[1] and 1-year point source catalog [159].

6.1.3 Results and conclusions

We report detection of angular power in all four energy bins considered, with a significance larger than 3σ in the energy bins from 1 GeV to 10 GeV. The data have been compared with the APS of a source model made of i) the point sources in [159], ii) a model for the interstellar diffuse emission and iii) an isotropic component at the level of the IGRB, more details on the measurement in [160]. Plots in figure 6.3 show the main results. The model angular power at $155 \leq l \leq 504$ is consistently below that measured in the data.

Despite the mask applied along the Galactic plane, some known Galactic emission can extend to high latitudes. Therefore a model of the Galactic foregrounds was subtracted from the data, and then the APS of the residual maps was calculated. This measurement is referred to as the cleaned data in [30]. We use this second measurement when comparing with DM predictions in the next section, table 6.1 present the measured values.

Due to decreasing photon statistics, the amplitude of anisotropies detectable by this analysis decreases with increasing energy. For this reason, the non-detection of power above the noise level at 10-50 GeV does not exclude the presence of anisotropies at the level of those detected at 1-10 GeV

[1] `http://fermi.gsfc.nasa.gov/ssc/data/access/lat/BackgroundModels.html`

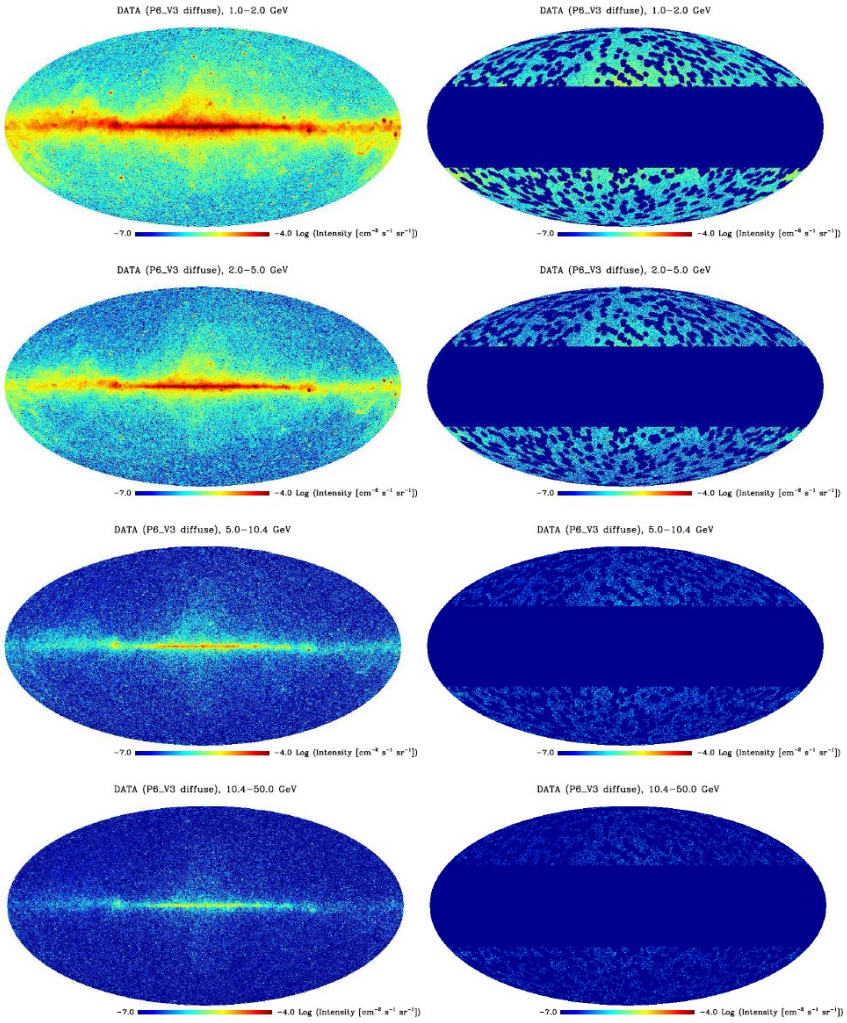

Figure 6.2: All-sky intensity maps of the data in the four energy bins used in this analysis in Galactic coordinates. The data is shown unmasked (left panels) and with the default mask applied (right panels). The mask excludes Galactic latitudes $|b| < 30^\circ$ and 2° angular radius around each point source in the 1FGL catalog. The map images shown have been downgraded in resolution to order 7 to improve the visual quality of the images; however, the analysis was performed on the higher resolution maps as described in the text.

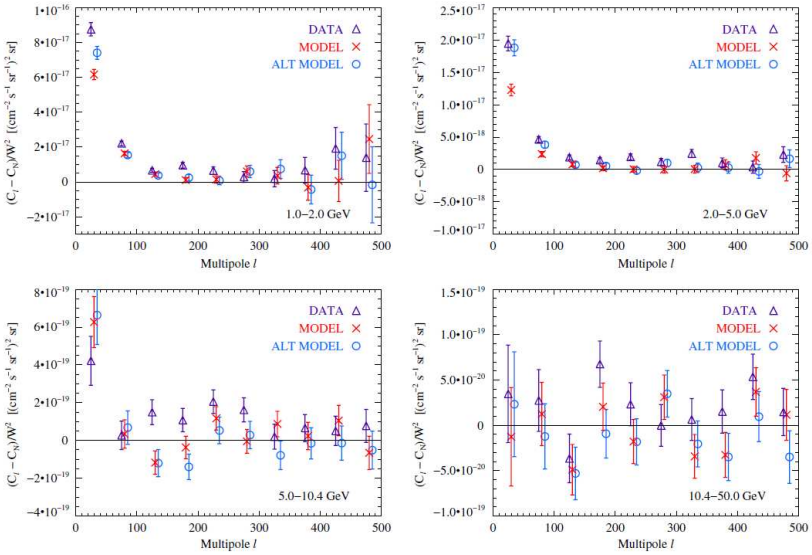

Figure 6.3: Angular power spectra of the data, the default simulated model (MODEL), and an alternate simulated model (ALT MODEL). The angular power spectra of the two models are in good agreement in all energy bins. The smaller amplitude angular power at l‘155 measured at lower significance in both models is inconsistent with the angular power observed in the data at all energies. Points from different data sets are offset slightly in multipole for clarity.

6.2 DM implications of *Fermi*-LAT measurement of anisotropies in the IGRB

6.2.1 DM predictions

The APS of gamma rays from DM annihilations or decays has been computed from the all-sky template maps produced in [33]. The authors of [33] used the Millennium-II N-body simulation to model the abundance and the clustering of extragalactic DM halos and subhalos. The technique presented in [161], based on the random repetition of copies of the Millennium-II simulation box, is implemented to probe the universe up to $z = 2$. The emission from DM halos with a mass below the resolution of the simulation was estimated assuming that the halo number density and the mass-luminosity relation obtained from the halos in Millennium-II remains unchanged below the resolution, down to the minimal self-bound halo mass M_{min}. On the other hand, the contribution of low mass subhalos was modeled following the technique described in [173] and extended in [174].

The smooth DM halo of the Milky Way was parametrized in [33] as an Einasto profile, since this provides the best fit to the Milky Way-like halo obtained in the

Aquarius N-body simulation. Galactic subhalos down to 10^5 $M_\odot$ were accounted for directly from the Aquarius simulation, while we use the same procedure as before to account for the contribution of unresolved subhalos. It has been shown that such objects do not contribute significantly to the total intensity APS.

In [33] the effect of the assumptions made in the modeling of the DM distribution also was estimated, looking for their effect both on the intensity of the DM-induced emission and on its APS. The two most relevant sources of uncertainty are the amount of substructures hosted by DM halos and the value of M_{min}. The first gives rise to an uncertainty of a factor 20-30 both in the average intensity and in the intensity APS; when the uncertainty on the value of M_{min} is taken into account, these factors build up to 40 and 100 for the average intensity and the intensity APS, respectively.

6.2.2 Setting constraints

Here we present the method used to set conservative limits on the thermally averaged cross section, $\langle\sigma v\rangle$, for DM annihilation into three different channels, $b\bar{b}$ quarks, $\mu^+\mu^-$, and $\tau^+\tau^-$ leptons.

- To set constraints we use the foreground-cleaned C_p shown in table 6.1. There are four C_p values measured corresponding to four energy bins, $1-2$ GeV, $2-5$ GeV, $5-10$ GeV, and $10-50$ GeV. We use them independently to set limits.

- Requiring that the DM-induced intensity APS averaged in $155 < l < 204$ does not overshoot the measured C_p in the $155 < l < 504$ multipole range plus 1.64 times its error leads to 95% CL limits on $\langle\sigma v\rangle$[2].

- We know that the IGRB anisotropy has multiple contributors, therefore these constraints are conservative. Other contributors to IGRB anisotropy are not well known, but we already have constraints on the contribution of blazars [176]. We subtract this contribution from the measured C_p and require that the DM-induced APS does not overshoot this new limit.

6.2.3 Preliminary results

We set competitive 95% CL limits on the annihilation cross section, as shown in figures 6.4 - 6.6 for three different channels, $b\bar{b}$ quarks, $\mu^+\mu^-$, and $\tau^+\tau^-$ leptons, respectively [31]. The main uncertainty in the predictions obtained in [33] lies

[2]We assume Gaussian erros, then the value of 1.64 is based on the fact that 95% of the area of a Gaussian distribution is within 1.64 standard deviations of the mean.

in the properties of low-mass subhalos, below the mass resolution of the simulations. Different values of the "subhalo boost" strongly affect the prediction for the DM-induced gamma-ray intensity and its anisotropies. In ref. [33] two benchmark scenarios for subhalos were considered, assuming that the uncertainties can be modeled by changing the subhalo abundance: i) the LOW case, where halos are relatively poor in subhalos, according to the predictions of [173] and [174]; the constraints using this scenario are shown in the left-upper panel of figures 6.4 - 6.6, and ii) the HIGH case, with large subhalo boosts, compatible with what was found by [175, 89]; the right-upper and lower panels in the figures 6.4 - 6.6 use this case. In the lower panels the predictions for the DM-induced APS (with a HIGH subhalo boost) are compared with the APS measured by Fermi-LAT once the contribution from blazars is subtracted. This represents the case where the most stringent constraints on $\langle \sigma v \rangle$ are obtained.

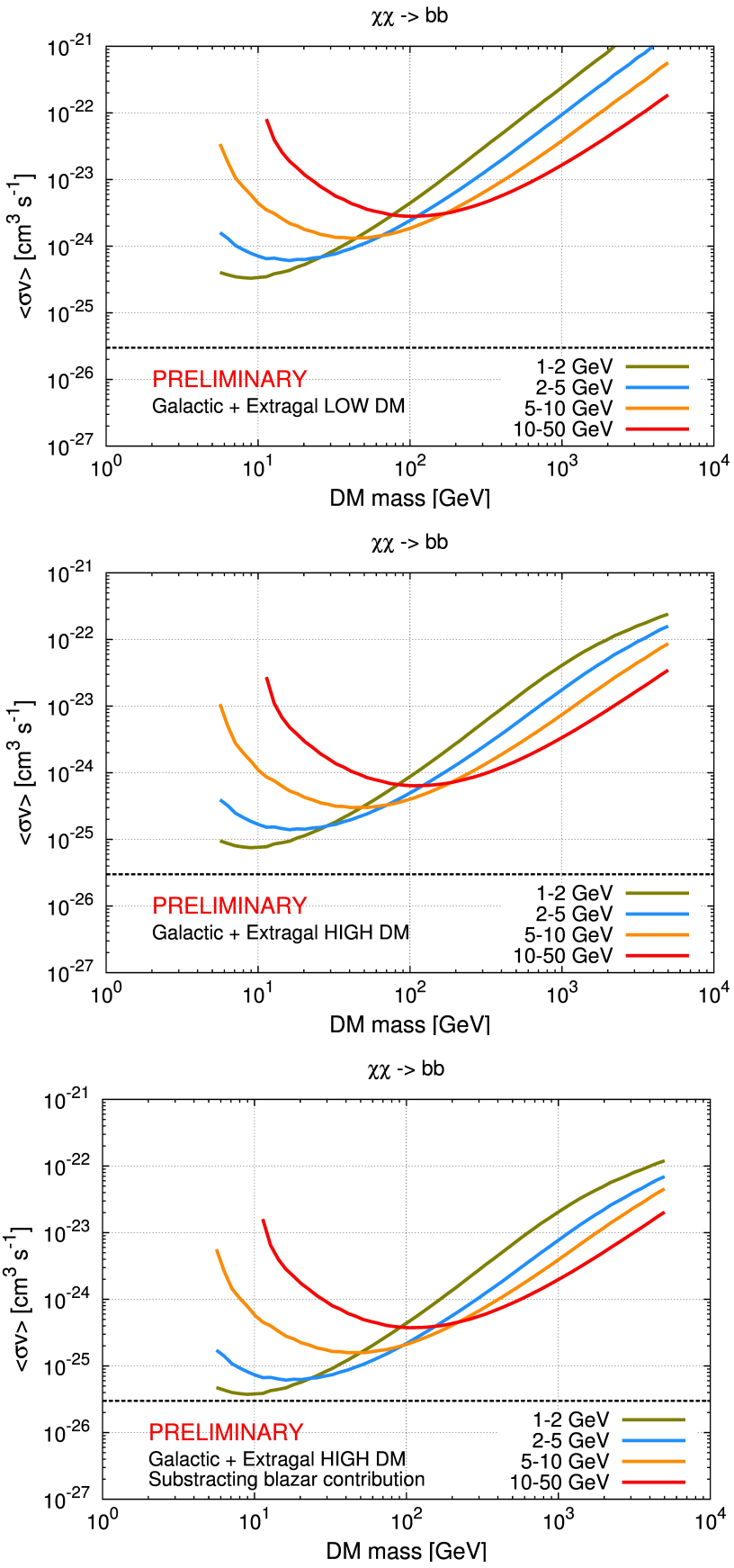

Figure 6.4: 95% CL limits on the annihilation cross section for the $b\bar{b}$ channel.

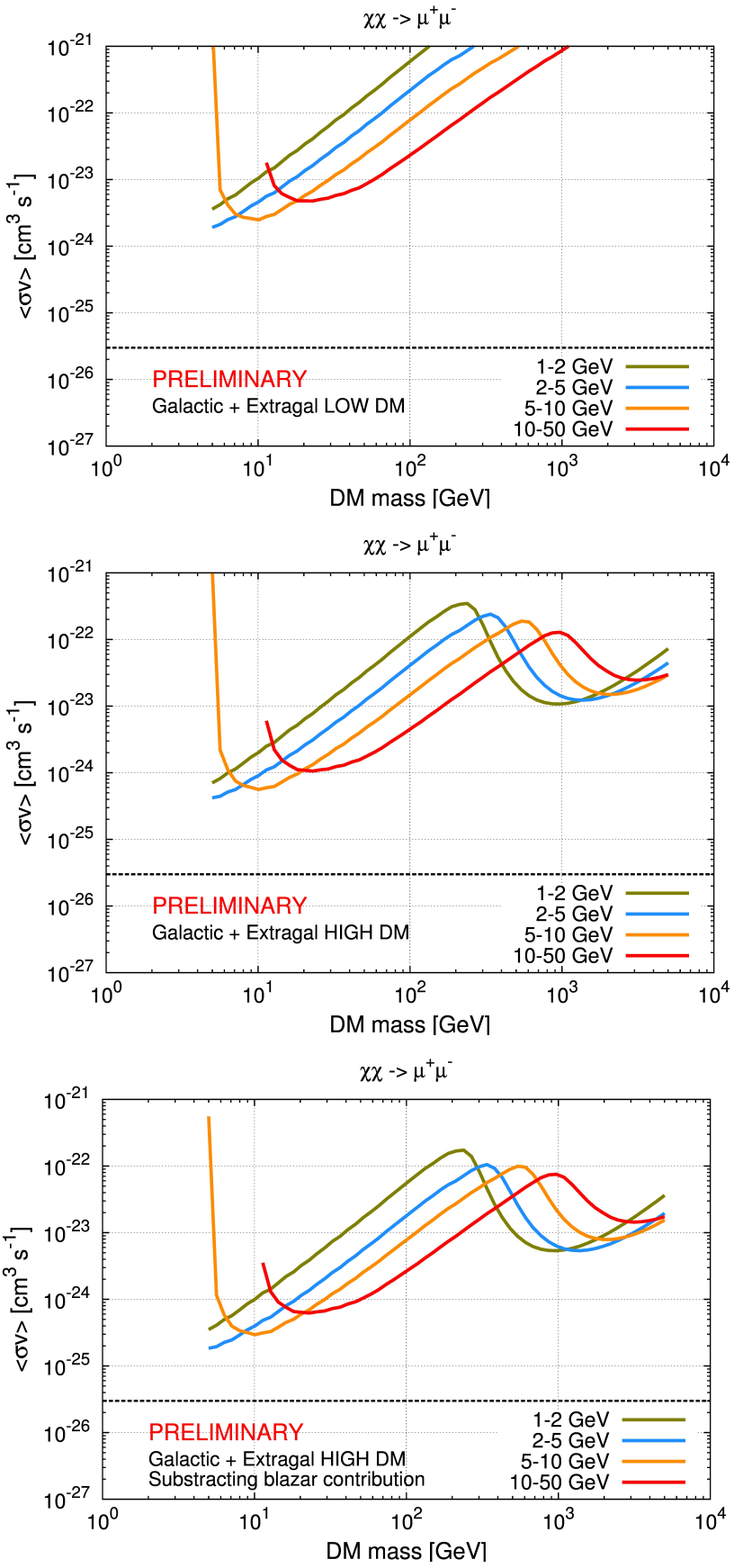

Figure 6.5: 95% CL limits on the annihilation cross section for the $\mu^+\mu^-$ channel.

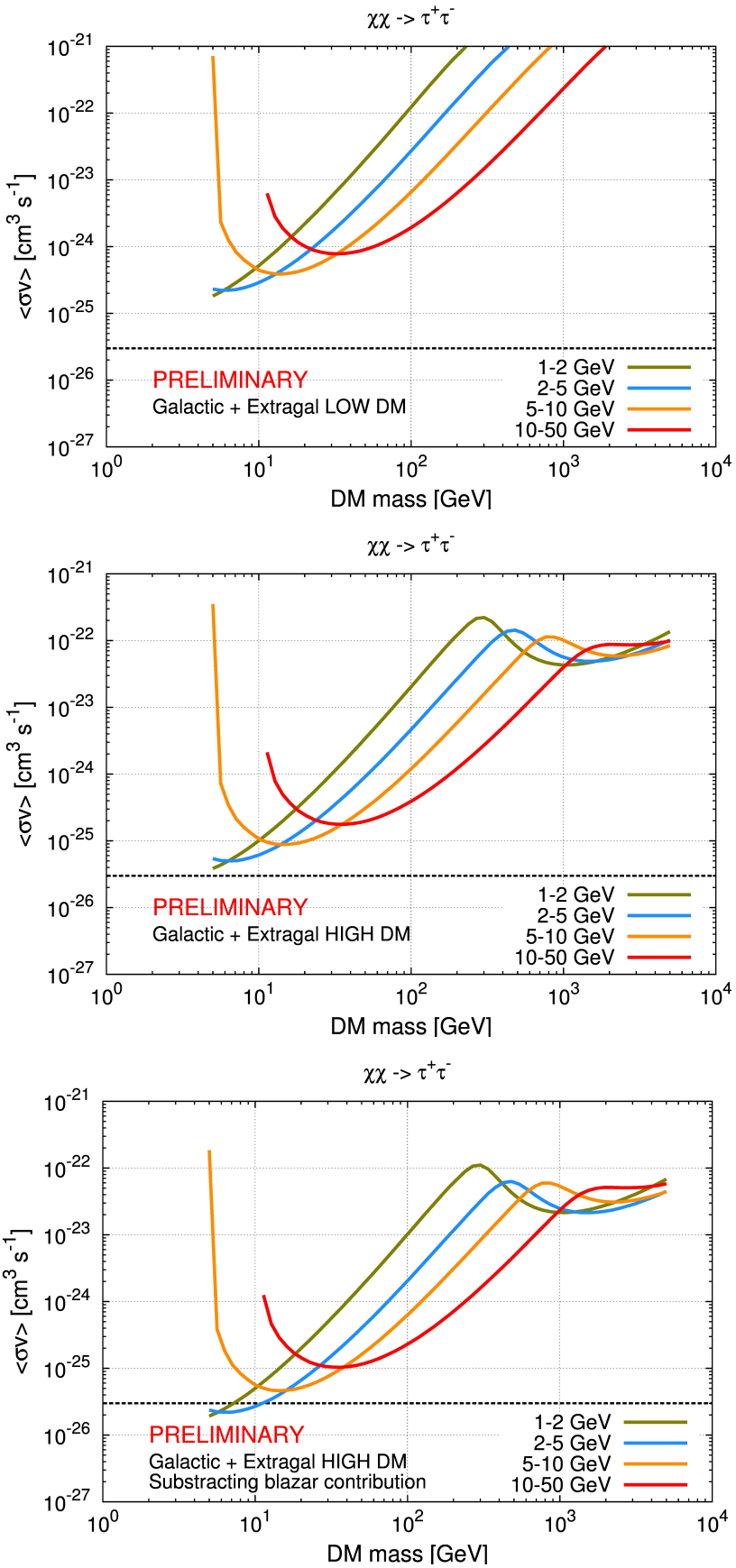

Figure 6.6: 95% CL limits on the annihilation cross section for the $\tau^+\tau^-$ channel.

Chapter 7
Conclusions and Outlook

I've been cordially invited to join the visceral realists. I accepted, of course.
There was no initiation ceremony. It was better that way.
Roberto Bolaño, *The savage detectives.*

The best way to prove the dark matter (DM) paradigm is to detect signatures of the particle that made up the unseen matter needed to fit observations. The main objective of this thesis is to seek for particle DM signals in the data taken by the *Fermi*-LAT space telescope. To achieve this goal, we determine three different targets: the Virgo cluster, the inner region of the Milky Way and the extragalactic gamma-ray background. First, we study the predicted signal and background, their energy spectrum and morphology. Second, we look at the sky with the *Fermi*-LAT and compare with predictions. Although we have not found a significant DM signal, we have been able to set interesting constraints on DM candidates

Using Virgo as target for DM searches, we have confirmed the potential of using extragalactic massive structures as optimal targets for decaying DM detection [22]. In particular, we have obtained the regions of the parameter space $(m_{3/2}, \tau_{3/2})$ of the $\mu\nu$SSM with the best prospects for the detection of a gamma-ray monochromatic line from the decay of gravitino DM, as shown in Fig. 4.2. We have found that a gravitino DM with a mass range of 0.6–2 GeV, and with a lifetime range of about 3×10^{27}–2×10^{28} s would be detectable by the *Fermi*-LAT with a signal-to-noise ratio larger than 3. We have also obtained that gravitino masses larger than about 4 GeV are now disfavoured in the $\mu\nu$SSM by *Fermi*-LAT data of the galactic halo. Finally, let us remark that the simulation of the gamma-ray flux was carried out with the use of the `gtobssim` routine from the Fermi Science Tools, whereas the DM distribution around the cluster has been modeled following the results of ref. [123] based on a constrained N-body simulation from the CLUES project.

Using the inner Galaxy region as target, we have performed a search for gamma-ray spectral lines from 5-300 GeV in several regions of interest defined a priori to optimize sensitivity for various DM density profiles, such as NFW contracted and Einasto [25]. This search was performed using 3.7 years of data that have been reprocessed using updated calorimeter calibration constants, and the 2D energy dispersion model that includes information about the event-by-event energy reconstruction quality. We have found no globally significant spectral line

signals, and obtain flux upper limits for monochromatic sources. For a particular DM density profile for the Milky Way, the flux upper limits can be translated to annihilation cross-section upper limits or decay-lifetime lower limits, as shown in figures 4.5 and 4.6, respectively. For the case of annihilation the limits lie in the range $\langle\sigma v\rangle_{\gamma\gamma} \equiv 10^{-29} - 10^{-27}$ cm^{3}s^{-1} with the precise limit depending on the WIMP mass and the DM density profile assumed for the Milky Way; cuspier profiles and lower masses are constrained more strongly. For decay the limits lie in the range $\tau_{\gamma\gamma} \equiv 1 - 8 \times 10^{-29}$ extending constraints to lower energies previous results from the collaboration.

We have also performed a careful fit at 133 GeV [25]. Although the feature in the region of interest optimized for a NFW compressed profile cannot be entirely explained in terms of known systematic effects, it does have certain characteristics that disfavor interpreting it as a DM signal. The fit significance reduces when using the 2D energy dispersion model, making the global significance of the feature 1.6σ. This decrease is in large part due to the 133 GeV feature being much narrower than the *Fermi*-LAT energy resolution, and not being present in events with incidence angle larger than 50°. More data and study are needed to clarify the origin of this feature.

Also using the inner Galaxy region as target, we have derived constraints on the parameter space of generic DM candidates using *Fermi*-LAT inner Galaxy measurements [28]. We have considered well motivated DM density profiles, such as Burkert, Einasto and NFW, which are perfectly compatible with current observational data of the Milky Way. With a compressed DM density profile we obtain upper limits on the DM annihilation cross-section that exclude the thermal cross section for a broad range of DM masses, as shown in Fig. 5.6. This is the case for masses smaller than 680, 530 and 490 GeV for $b\bar{b}$, $\tau^+\tau^-$ and W^+W^- channels, respectively. For the $\mu^+\mu^-$ channel, where the inverse Compton scattering effect is important, the exclusion of the thermal cross-section is for a mass smaller than about 150 to 400 GeV, depending on models of the Galactic magnetic field. Alternatively, one may interpret these results as implying that generic WIMP models and contracted DM profiles are incompatible with the *Fermi* data. Although the constraints are very strong, the analysis is conservative since we require that the expected DM signal does not exceed the gamma-ray emission observed by the *Fermi*-LAT, and modeling of the astrophysical background is not carried out. The latter would only lead to better constraints on the DM annihilation cross section.

Regarding the background in the inner Galaxy region we have shown results concluding that the majority of the diffuse emission is removed using a physically-motivated model based on GALPROP, as shown in the upper panels of Fig. 5.9. The diffuse model subtraction yield spatial residuals in $45° \times 45°$ about the center of the galaxy consistent with known point sources and small fluctuations. Preliminary results from *Fermi*-LAT show that most of the emission from a $15° \times 15°$ region

around the direction of the Galactic center can be modeled in terms of diffuse emission and point sources. The major conclusion of these works is that our knowledge of the conventional astrophysical background is uncertain. This is currently a big limitation for the search of DM in the Galactic center with gamma rays, which otherwise has a huge potential for discovery or for setting constraints.

Using the anisotropies in the extragalactic gamma-ray background (that we have measured with *Fermi*-LAT), we set competitive 95% CL limits on the annihilation cross section for three different channels, $b\bar{b}$ quarks, $\mu^+\mu^-$ and $\tau^+\tau^-$ leptons [31]. To set this constraints we have contrasted predictions for the DM-induced angular power spectrum (APS) from ref. [33] with the APS measured by *Fermi*-LAT. In ref. [33] two benchmark scenarios for subhalos were considered, assuming that the uncertainties can be modeled by changing the subhalo abundance: i) the LOW case, where halos are relatively poor in subhalos; the constraints using this scenario are shown in the upper panels of figures 6.4 - 6.6, and ii) the HIGH case, with large subhalo boosts; the middle and lower panels in the figures 6.4 - 6.6 use this case. In the lower panels the DM predictions (with a HIGH subhalo boost) are compared with the measurement by *Fermi*-LAT once the contribution from blazars is subtracted. This represents the case where the most stringent constraints on $\langle\sigma v\rangle$ are obtained.

In order to keep exploring theories beyond the standard model through their DM candidates with observations of the sky, my plans for future research are in the direction of looking deeper in the inner region of our galaxy and consider the implications of recent results from the LHC and direct DM detection experiments on those theories.

In this sense concerning the inner region of the Milky Way, I would like to explore the parameter space of specific particle physics models, such as the Minimal Supersymmetric Standard Model (MSSM) and the Next-to-MSSM (NMSSM) with neutralinos and righ-handed neutrinos as DM candidates. Let us remark that in general the DM annihilation final state will be a combination of the final states usually considered [28, 31]. For example, in the MSSM the lighest neutralino annihilation modes are 70% $\bar{b}b$ − 30% $\bar{\tau}\tau$ for a Bino DM, and 100% W^+W^- for a Wino DM (or for a Higgs-portal model). Also, the emission from known astrophysical gamma-ray emitters must be taken into account but there is not a unique diffuse model that can globally explain of all the events detected by the *Fermi*-LAT [81]. Therefore marginalization of diffuse models and computation of DM spectrum from specific DM candidates are needed in order to ruled out or favour parameter space regions of the DM models.

Following up the paper on the $\mu\nu$SSM gravitino line searches [22], together with Dr. Michael Grefe (IFT), Prof. Aldo Morselli (INFN), Prof. Carlos Muñoz

(UAM & IFT), and Dr. Christopher Weniger (GRAPPA), we have recently started a project with the *Fermi*-LAT collaboration to search for gamma-ray lines over the energy range 100 MeV to 10 GeV in the inner Galaxy region. This energy range has not been analysed yet by the collaboration because only a few DM models predict lines in that region and given the characteristics of the *Fermi*-LAT and the nature of the astrophysical background for line searches, the systematic uncertainties differ from the analysis at energies above 10 GeV. A deeper knowledge of the instrument is needed to study the low energy band, indeed, this is one of the milestone in the operation extension of the Fermi mission. We are convince that even with conservative systematic errors put into the analysis the limits would be very interesting for the $\mu\nu$SSM.

Looking further ahead, information from the inner region of our galaxy and other important DM targets is continuously growing, not only the gamma-ray data from the *Fermi*-LAT or Cherenkov telescopes, also data in other wavelengths as microwave and infra-red from Planck. Multi-wavelength studies are bringing us a complete picture of the sky at high energies and exotic contributors as DM can be constrained more and more or even observed. The LHC is improving our understanding of the physics at the GeV-TeV scale where most of the DM candidates are expected to live, giving us constrains on fundamental interactions. Indirect detection experiments are also doing very well excluding important regions of the parameter space of DM candidates. Therefore, I see big opportunities for future investigations in the study of the sky with different instruments and complementarity among experiments, to extract information about the DM nature as a window to explore theories beyond the standard model.

Bibliography

[1] W. Hu, N. Sugiyama and J. Silk, "The Physics of microwave background anisotropies," Nature **386** (1997) 37 (Cited on page 1.)

[2] E. Komatsu *et al.* [WMAP Collaboration], "Seven-Year Wilkinson Microwave Anisotropy Probe (WMAP) Observations: Cosmological Interpretation," Astrophys. J. Suppl. **192** (2011) 18 (Cited on pages 1 and 2.)

[3] P. A. R. Ade *et al.* [Planck Collaboration], "Planck 2013 results. XVI. Cosmological parameters," arXiv:1303.5076 [astro-ph.CO]. (Cited on pages 1 and 2.)

[4] A. Biviano, "Tracing the mass profiles of galaxy clusters with member galaxies," Invited review at Conference: C05-07-04.5 astro-ph/0509679. (Cited on page 1.)

[5] A. Cavaliere and A. Lapi, "The Astrophysics of the Intracluster Plasma," Accepted by Physics Reports [arXiv:1308.6673 [astro-ph.CO]]. (Cited on page 1.)

[6] F. Zwicky, "Die Rotverschiebung Von Extragalaktischen Nebeln," Helvetica Physica Acta, **6** (1933) 110 (Cited on page 1.)

[7] Y. Sofue and V. Rubin, "Rotation curves of spiral galaxies," Ann. Rev. Astron. Astrophys. **39** (2001) 137 (Cited on pages 2 and 11.)

[8] C. S. Kochanek, P. Schneider, J. Wambsganss, "Gravitational Lensing: Strong, Weak and Micro," Proceedings of the 33rd Saas-Fee Advanced Course 2004, G. Meylan, P. Jetzer and P. North, editors (Springer-Verlag: Berlin). (Cited on page 2.)

[9] K. A. Olive, "TASI lectures on dark matter," astro-ph/0301505. (Cited on page 2.)

[10] D. Clowe, M. Bradac, A. H. Gonzalez, M. Markevitch, S. W. Randall, C. Jones and D. Zaritsky, "A direct empirical proof of the existence of dark matter," Astrophys. J. **648** (2006) L109 [astro-ph/0608407]. (Cited on page 2.)

[11] M. Roos, "Astrophysical and Cosmological Probes of Dark Matter," Journal of Modern Physics, **29** (2012) 1152 (Cited on page 2.)

[12] W. Hu and S. Dodelson, "Cosmic microwave background anisotropies," Ann. Rev. Astron. Astrophys. **40** (2002) 171 (Cited on page 2.)

[13] A. R. Liddle and D. H. Lyth, "The Cold dark matter density perturbation," Phys. Rept. **231** (1993) 1 (Cited on page 2.)

[14] G. Bertone, D. Hooper and J. Silk, "Particle dark matter: Evidence, candidates and constraints," Phys. Rept. **405** (2005) 279 (Cited on pages 2 and 16.)

[15] C. Munoz, "Dark matter detection in the light of recent experimental results," Int. J. Mod. Phys. A **19** (2004) 3093 (Cited on page 2.)

[16] H. Reeves, "On the origin of the light elements (Z<6)," Rev. Mod. Phys. **66** (1994) 193. (Cited on page 2.)

[17] A. Coc, "Primordial Nucleosynthesis," J. Phys. Conf. Ser. **420** (2013) 012136 (Cited on page 2.)

[18] J. Silk and M. Srednicki, "Cosmic Ray anti-Protons as a Probe of a Photino Dominated Universe," Phys. Rev. Lett. **53** (1984) 624. (Cited on page 2.)

[19] W. B. Atwood *et al.* [Fermi-LAT Collaboration], "The Large Area Telescope on the Fermi Gamma-ray Space Telescope Mission," Astrophys. J. **697** (2009) 1071 (Cited on pages 4, 27 and 54.)

[20] [Fermi-LAT Collaboration], "Fermi Large Area Telescope Second Source Catalog," Astrophys. J. Suppl. **199** (2012) 31 (Cited on pages 4 and 40.)

[21] W. L. Kraushaar, G. W. Clark, G. P. Garmire, R. Borken, P. Higbie, V. Leong and T. Thorsos, "High-Energy Cosmic Gamma-Ray Observations from the OSO-3 Satellite," Astrophys. J. **177** (1972) 341. (Cited on pages 4 and 73.)

[22] **G. A. Gomez-Vargas**, M. Fornasa, F. Zandanel, A. J. Cuesta, C. Munoz, F. Prada and G. Yepes, "CLUES on Fermi-LAT prospects for the extragalactic detection of $\mu\nu$SSM gravitino Dark Matter," JCAP **1202** (2012) 001 (Cited on pages 4, 35, 39, 41, 85 and 87.)

[23] D. E. Lopez-Fogliani and C. Muñoz, "Proposal for a supersymmetric standard model," Phys. Rev. Lett. **97** (2006) 041801 (Cited on pages 5, 22 and 35.)

[24] C. Muñoz, "Effects of right-handed neutrinos on supersymmetric models", unpublished notes (1994). (Cited on pages 5, 22 and 35.)

[25] M. Ackermann*et al.* [Fermi-LAT Collaboration including **G. A. Gomez-Vargas**], "Search for Gamma-ray Spectral Lines with the Fermi Large Area Telescope and Dark Matter Implications," arXiv:1305.5597 [astro-ph.HE]. (Cited on pages 5, 35, 45, 46, 47, 49, 50, 85 and 86.)

[26] T. Bringmann, X. Huang, A. Ibarra, S. Vogl and C. Weniger, "Fermi LAT Search for Internal Bremsstrahlung Signatures from Dark Matter Annihilation," JCAP **1207** (2012) 054 (Cited on pages 5, 19, 35, 43 and 59.)

[27] C. Weniger, "A Tentative Gamma-Ray Line from Dark Matter Annihilation at the Fermi Large Area Telescope," JCAP **1208** (2012) 007 (Cited on pages 5, 35, 44, 45 and 46.)

[28] **G. A. Gomez-Vargas**, M. A. Sanchez-Conde, J. -H. Huh, M. Peiro, F. Prada, A. Morselli, A. Klypin, D. G. Cerdeno, Y. Mambrini and C. Munoz. "Constraints on WIMP Annihilation for Contracted Dark Matter in the Inner Galaxy with the Fermi-LAT," JCAP **1210** (2013) 029 (Cited on pages 5, 54, 86 and 87.)

[29] A. W. Strong and I. V. Moskalenko, "Propagation of cosmic-ray nucleons in the galaxy," Astrophys. J. **509** (1998) 212 (Cited on pages 5 and 54.)

[30] M. Ackermann *et al.* [Fermi LAT Collaboration, including **G. A. Gomez-Vargas**], "Anisotropies in the diffuse gamma-ray background measured by the Fermi LAT," Phys. Rev. D **85** (2012) 083007 (Cited on pages 6, 27, 28, 58, 74 and 76.)

[31] **G. A. Gomez-Vargas**, A. Cuoco, T. Linden, M.A. Sanchez-Conde, and J.M. Siegal-Gaskins for the *Fermi*-LAT collaboration, and T. Delahaye, M. Fornasa, E. Komatsu, F. Prada, J. Zavala, "Dark Matter implications of *Fermi*-LAT measurement of anisotropies in the diffuse gamma-ray background," accepted for publication in Nuclear Instruments and Methods in Physics Research A [arXiv:1303.2154 [astro-ph.HE]] (Cited on pages 6, 79 and 87.)

[32] A. Cuoco, **G. A. Gomez-Vargas**, L. Latronico T. Linden, A. Morselli, M.A. Sanchez-Conde, J.M. Siegal-Gaskins, V. Vitale for the *Fermi*-LAT collaboration, and T. Delahaye, M. Fornasa, C. Frenk, E. Komatsu, F. Prada, M. Vogelsberger, J. Zavala, "Dark Matter implications of *Fermi*-LAT measurement of anisotropies in the diffuse gamma-ray background," In preparation, preliminary results already presented in the 4th International Fermi Symposium, 28 Oct - 2 Nov 2012. Monterey, California, USA (Cited on page 6.)

[33] M. Fornasa, J. Zavala, M. A. Sánchez-Conde, J. M. Siegal-Gaskins, T. Delahaye, F. Prada, M. Vogelsberger, F. Zandanel, C. S. Frenk, "Characterization of dark-matter-induced anisotropies in the diffuse gamma-ray background, " Mon. Not. Roy. Astron. Soc. **429** (2013) 1529-1553 (Cited on pages 6, 74, 78, 79, 80 and 87.)

[34] J. P. Ostriker, P. J. E. Peebles, "A Numerical Study of the Stability of Flattened Galaxies: or, can Cold Galaxies Survive?, " Astrophys. J. **186** (1973) 467 (Cited on page 10.)

[35] Y. Sofue, Y. Tutui, M. Honma, A. Tomita, T. Takamiya, J. Koda and Y. Takeda, "Central rotation curves of spiral galaxies," Astrophys. J. **523** (1999) 136 (Cited on page 11.)

[36] P. J. E. Peebles, "Dark Matter," arXiv:1305.6859 [astro-ph.CO]. (Cited on page 11.)

[37] M. Boylan-Kolchin, V. Springel, S. D. M. White, A. Jenkins and G. Lemson, "Resolving Cosmic Structure Formation with the Millennium-II Simulation," Mon. Not. Roy. Astron. Soc. **398** (2009) 1150 (Cited on page 12.)

[38] V. Springel, C. S. Frenk and S. D. M. White, "The large-scale structure of the Universe," Nature **440** (2006) 1137 (Cited on page 12.)

[39] S. Gottloeber, Y. Hoffman and G. Yepes, "Constrained Local UniversE Simulations (CLUES)," Proceedings of High Performance Computing in Science and Engineering, Garching/Munich 2009, pp 309 - 322, Springer-Verlag, 2010. (Cited on pages 13 and 37.)

[40] A. Klypin, Y. Hoffman, A. Kravtsov and S. Gottloeber, "Constrained Simulations of the Real Universe: the Local Supercluster," Astrophys. J. **596** (2003) 19 (Cited on page 13.)

[41] A. V. Kravtsov, A. A. Klypin, J. S. Bullock and J.R. Primack, The Cores of dark matter dominated galaxies: Theory versus observations, Astrophys. J. **502** (1998) 48 (Cited on page 13.)

[42] J. F. Navarro, C. S. Frenk and S. D. M. White, The Structure of cold dark matter halos, Astrophys. J. **462** (1996) 563 (Cited on pages 14, 15 and 36.)

[43] J. F. Navarro, C. S. Frenk and S. D. M. White, A Universal density profile from hierarchical clustering, Astrophys. J. **490** (1997) 493 (Cited on pages 14, 15 and 36.)

[44] J. Einasto, Publications of the Tartuskoj Astrofizica Observatory **36** (1968) 414. (Cited on page 14.)

[45] J. F. Navarro, E. Hayashi and C. Power *et al.*, The Inner structure of Lambda-CDM halos 3: Universality and asymptotic slopes, Mon. Not. Roy. Astron. Soc. **349** (2004) 1039 (Cited on page 14.)

[46] A. W. Graham, D. Merritt, B. Moore, J. Diemand and B. Terzic, "Empirical models for Dark Matter Halos. I. Nonparametric Construction of Density Profiles and Comparison with Parametric Models," Astron. J. **132** (2006) 2685 (Cited on page 14.)

[47] A. Burkert, A. Burkert, "The Structure of dark matter halos in dwarf galaxies," IAU Symp. **171** (1996) 175 [Astrophys. J. **447** (1995) L25] (Cited on page 14.)

[48] B. Moore, T. R. Quinn, F. Governato, J. Stadel and G. Lake, "Cold collapse and the core catastrophe," Mon. Not. Roy. Astron. Soc. **310** (1999) 1147 (Cited on page 15.)

[49] J. Diemand, M. Kuhlen, P. Madau, M. Zemp, B. Moore, D. Potter and J. Stadel, Clumps and streams in the local dark matter distribution, Nature **454** (2008) 735 (Cited on page 15.)

[50] J. Stadel, D. Potter, B. Moore, J. Diemand, P. Madau, M. Zemp, M. Kuhlen and V. Quilis, "Quantifying the heart of darkness with GHALO - a multi-billion particle simulation of our galactic halo," MNRAS **398** (2009) L21 (Cited on page 15.)

[51] V. Springel, J. Wang, M. Vogelsberger *et al.*, The Aquarius Project: the subhalos of galactic halos, MNRAS **391** (2008) 1685 [arXiv:0809.0898 [astro-ph]]. (Cited on page 15.)

[52] Ya. B. Zeldovich, A. A. Klypin, M. Yu. Khlopov and V. M. Chechetkin, Sov. J. Nucl. Phys. **31** (1980) 664. (Cited on pages 15 and 55.)

[53] G.R. Blumenthal, S.M. Faber, R. Flores and J.R. Primack, Astrophys. J. **301** (1986) 27. (Cited on pages 15 and 55.)

[54] O. Y. Gnedin, A. V. Kravtsov, A. A. Klypin and D. Nagai, Astrophys. J. **616** (2004) 16 [astro-ph/0406247 [astro-ph]]. (Cited on pages 15 and 55.)

[55] M. Gustafsson, M. Fairbairn and J. Sommer-Larsen, Phys. Rev. D **74** (2006) 123522 [astro-ph/0608634 [astro-ph]]. (Cited on pages 15 and 55.)

[56] P. Colín, O. Valenzuela and A. A. Klypin, Astrophys. J. **644** (2006) 687 [astro-ph/0506627 [astro-ph]]. (Cited on pages 15 and 55.)

[57] P. B. Tissera, S. D. M. White, S. Pedrosa and C. Scannapieco, MNRAS **406** (2010) 922 [arXiv:0911.2316 [astro-ph.CO]]. (Cited on pages 15 and 55.)

[58] O. Y. Gnedin, D. Ceverino, N. Y. Gnedin, A. A. Klypin, A. V. Kravtsov, R. Levine, D. Nagai and G. Yepes, arXiv:1108.5736 [astro-ph.CO]. (Cited on pages 15, 55 and 56.)

[59] M. Zemp, O. Y. Gnedin, N. Y. Gnedin and A. V. Kravtsov, "The impact of baryon physics on the structure of high-redshift galaxies," Astrophys. J. **748** (2012) 54 (Cited on pages 15 and 55.)

[60] J. Sommer-Larsen and M. Limousin, "Moderate Steepening of Galaxy Cluster Dark Matter Profiles by Baryonic Pinching," MNRAS **408** (2010) 1998 (Cited on pages 15 and 55.)

[61] F. Prada, A. Klypin, J. Flix Molina, M. Martinez and E. Simonneau, "Dark Matter Annihilation in the Milky Way Galaxy: Effects of Baryonic Compression," Phys. Rev. Lett. **93** (2004) 241301 [(Cited on pages 15, 20, 25, 55 and 66.)

[62] Y. Mambrini, C. Muñoz, E. Nezri and F. Prada, 'Adiabatic compression and indirect detection of supersymmetric dark matter', JCAP **01** (2006) 010 (Cited on pages 15, 55, 56 and 66.)

[63] S. Ando and D. Nagai, JCAP **07** (2012) 17 [arXiv:1201.0753[astro-ph.HE]]. (Cited on page 15.)

[64] S. Mashchenko, H. M. P. Couchman and J. Wadsley, Nature 442 (2006) 539 [astro-ph/0605672]. (Cited on page 16.)

[65] S. Mashchenko, J. Wadsley and H. M. P. Couchman, Science 319 (2008) 174 [arXiv:0711.4803[astro-ph]]. (Cited on page 16.)

[66] A. Pontzen and F. Governato, MNRAS **421** (2012) 3464 [arXiv:1106.0499 [astro-ph.CO]]. (Cited on page 16.)

[67] F. Governato, C. Brook, L. Mayer *et al.*, Nature **463** (2010) 203 [arXiv:0911.2237 [astro-ph.CO]]. (Cited on page 16.)

[68] A. V. Macciò, G. Stinson, C. B. Brook *et al.* Astrophys. J. Lett. **744** (2012) L9 [arXiv:1111.5620 [astro-ph.CO]]. (Cited on page 16.)

[69] A. Di Cintio, C. B. Brook, A. V. Maccio, G. S. Stinson, A. Knebe, A. A. Dutton and J. Wadsley, arXiv:1306.0898 [astro-ph.CO]. (Cited on page 16.)

[70] F. Iocco, M. Pato, G. Bertone and P. Jetzer, JCAP **11** (2011) 29 [arXiv:1107.5810 [astro-ph.GA]]. (Cited on page 56.)

[71] R. Catena and P. Ullio, "A novel determination of the local dark matter density," JCAP **08** (2010) 004 [arXiv:0907.0018 [astro-ph.CO]]. (Cited on page 56.)

[72] M. Ackermann *et al.* [LAT Collaboration], "Constraints on the Galactic Halo Dark Matter from Fermi-LAT Diffuse Measurements," Astrophys. J. **761** (2012) 91 (Cited on pages 55, 56 and 65.)

[73] D. Hooper, C. Kelso and F. S. Queiroz, "Stringent and Robust Constraints on the Dark Matter Annihilation Cross Section From the Region of the Galactic Center," arXiv:1209.3015 [astro-ph.HE]. (Cited on pages 56 and 66.)

[74] J. Guedes, S. Callegari, P. Madau & L. Mayer, Astrophys. J. **742** (2011) 76 [arXiv:1103.6030[astro-ph.CO]]. (Cited on page 56.)

[75] F. Nesti and P. Salucci, arXiv:1304.5127[astro-ph.GA]. (Cited on pages 56 and 57.)

[76] P. Gondolo and J. Silk, Phys. Rev. Lett. **83** (1999) 1719 [astro.ph/9906391]. (Cited on page 56.)

[77] O. Y. Gnedin and J. R. Primack, Dark Matter Profile in the Galactic Center, Phys. Rev. Lett. **93** (2004) 061302 [astro-ph/0308385]. (Cited on page 56.)

[78] G. Bertone, G. Sigl and J. Silk, MNRAS **337** (2002) 98 [astro-ph/0203488]. (Cited on page 56.)

[79] S. Profumo, "TASI 2012 Lectures on Astrophysical Probes of Dark Matter," arXiv:1301.0952 [hep-ph]. (Cited on page 16.)

[80] See, e.g.: N. Bernal and S. Palomares-Ruiz, Nucl. Phys. **B857** (2012) 380 [arXiv 1006.0477[astro-ph.HE]]. (Cited on page 18.)

[81] M. Ackermann *et al.* [Fermi-LAT Collaboration], "Fermi-LAT Observations of the Diffuse Gamma-Ray Emission: Implications for Cosmic Rays and the Interstellar Medium," Astrophys. J. **750** (2012) 3 (Cited on pages 18, 68, 69 and 87.)

[82] A. Birkedal, K. T. Matchev, M. Perelstein and A. Spray, "Robust gamma ray signature of WIMP dark matter," hep-ph/0507194. (Cited on pages 19 and 65.)

[83] T. Bringmann, L. Bergstrom and J. Edsjo, "New Gamma-Ray Contributions to Supersymmetric Dark Matter Annihilation," JHEP **01** (2008) 049 (Cited on page 19.)

[84] M. A. Sánchez-Conde, F. Prada, E. L. Lokas, M.E. Gómez, R. Wojtak and M. Moles, Dark Matter annihilation in Draco: New considerations of the expected gamma flux, Phys. Rev. D **76** (2007) 123509 (Cited on page 20.)

[85] T. Bringmann, M. Doro and M. Fornasa, Dark Matter signals from Draco and Willman 1: Prospects for MAGIC II and CTA, JCAP **01** (2009) 016 (Cited on page 20.)

[86] M. Cirelli, G. Corcella, A. Hektor, G. Hutsi, M. Kadastik, P. Panci, M. Raidal, F. Sala *et al.*, JCAP **03** (2011) 051, Erratum-ibid. **10** (2012) E01 (Cited on pages 19, 20, 21 and 22.)

[87] T. Sjostrand, S. Mrenna and P. Z. Skands, "PYTHIA 6.4 Physics and Manual," JHEP **05** (2006) 026 (Cited on page 19.)

[88] A. Pinzke, C. Pfrommer and L. Bergstrom, "Prospects of detecting gamma-ray emission from galaxy clusters: cosmic rays and dark matter annihilations," Phys. Rev. D **84** (2011) 123509 (Cited on page 20.)

[89] L. Gao, C. S. Frenk, A. Jenkins, V. Springel and S. D. M. White, "Where will supersymmetric dark matter first be seen?," Mon. Not. Roy. Astron. Soc. **419** (2012) 1721 (Cited on pages 20 and 80.)

[90] N. Fornengo, L. Pieri and S. Scopel, Neutralino annihilation into gamma-rays in the Milky Way and in external galaxies, Phys. Rev. D **70** (2004) 103529 (Cited on page 56.)

[91] M. Cirelli and P. Panci, "Inverse Compton constraints on the Dark Matter e+e- excesses," Nucl. Phys. B **821** (2009) 399 (Cited on page 21.)

[92] A. W. Strong, I. V. Moskalenko and O. Reimer, "Diffuse continuum gamma-rays from the galaxy," Astrophys. J. **537** (2000) 763, Erratum-ibid. **541** (2000) 1109 (Cited on page 21.)

[93] T. Delahaye, R. Lineros, F. Donato, N. Fornengo and P. Salati, "Positrons from dark matter annihilation in the galactic halo: Theoretical uncertainties," Phys. Rev. D **77** (2008) 063527 (Cited on page 21.)

[94] D. Maurin, F. Donato, R. Taillet and P. Salati, "Cosmic rays below z=30 in a diffusion model: new constraints on propagation parameters," Astrophys. J. **555** (2001) 585 (Cited on page 21.)

[95] `https://ccse.lbl.gov/BoxLib/index.html` (Cited on page 21.)

[96] For a review, see: C. Muñoz, "SUSY: New Perspectives and Variants," XLIth Rencontres de Moriond: Electroweak Interactions and Unified Theories, Ed. J. Tran Thanh Van, The Gioi Publishers (2006), arXiv:0705.2007 [hep-ph]. (Cited on page 22.)

[97] For a review, see: S. P. Martin, "A Supersymmetry primer," In Kane, G.L. (ed.): Perspectives on supersymmetry II* 1-153, World Scientific (2010) [hep-ph/9709356]. (Cited on page 22.)

[98] J. E. Kim and H. P. Nilles, "The μ-Problem and the Strong CP-Problem," Phys. Lett. B **138** (1984) 150. (Cited on page 22.)

[99] N. Escudero, D. E. López-Fogliani, C. Muñoz and R. R. de Austri, "Analysis of the parameter space and spectrum of the $\mu\nu$SSM," JHEP **0812** (2008) 099 (Cited on pages 22, 23 and 36.)

[100] For a review, see: C. Muñoz, "Phenomenology of a New Supersymmetric Standard Model: The $\mu\nu$SSM," AIP Conf. Proc. **1200** (2010) 413 (Cited on pages 22 and 36.)

[101] For a review, see: D. E. López-Fogliani, "The Seesaw mechanism in the $\mu\nu$SSM," arXiv:1004.0884 [hep-ph]. (Cited on pages 22 and 36.)

[102] For a review, see: U. Ellwanger, C. Hugonie and A. M. Teixeira, "The Next-to-Minimal Supersymmetric Standard Model," Phys. Rept. **496** (2010) 1 (Cited on page 22.)

[103] J. Fidalgo, D. E. López-Fogliani, C. Muñoz and R. Ruiz de Austri, "Neutrino Physics and Spontaneous CP Violation in the $\mu\nu$SSM," JHEP **0908** (2009) 105 (Cited on page 23.)

[104] P. Ghosh and S. Roy, "Neutrino masses and mixing, lightest neutralino decays and a solution to the μ problem in supersymmetry," JHEP **0904** (2009) 069 (Cited on page 23.)

[105] P. Ghosh, P. Dey, B. Mukhopadhyaya and S. Roy, "Radiative contribution to neutrino masses and mixing in $\mu\nu$SSM," JHEP **1005** (2010) 087 (Cited on page 23.)

[106] For a review, see: M. Hirsch and J. W. F. Valle, "Supersymmetric origin of neutrino mass," New J. Phys. **6** (2004) 76 [hep-ph/0405015]. (Cited on page 23.)

[107] A. Bartl, M. Hirsch, A. Vicente, S. Liebler and W. Porod, "LHC phenomenology of the $\mu\nu$SSM," JHEP **0905** (2009) 120 (Cited on page 23.)

[108] P. Bandyopadhyay, P. Ghosh and S. Roy, "Unusual Higgs boson signal in R-parity violating nonminimal supersymmetric models at the LHC," Phys. Rev. D **84** (2011) 115022 (Cited on page 23.)

[109] S. Liebler and W. Porod, "On-shell renormalization of neutralino and chargino mass matrices in R-parity violating models - Correlation between LSP decays and neutrino mixing angles revisited," Nucl. Phys. B **855** (2012) 774 (Cited on page 23.)

[110] J. Fidalgo, D. E. López-Fogliani, C. Muñoz and R. R. de Austri, "The Higgs sector of the $\mu\nu$SSM and collider physics," JHEP **1110** (2011) 020 (Cited on page 23.)

[111] P. Ghosh, D. E. López-Fogliani, V.A. Mitsou, C. Muñoz and R. R. de Austri, "Probing the μ -from- ν supersymmetric standard model with displaced multileptons from the decay of a Higgs boson at the LHC," arXiv:1211.3177 [hep-ph]. (Cited on page 23.)

[112] Y. Farzan and J. W. F. Valle, "R-parity violation assisted thermal legtogenesis in the seesaw mechanism," Phys. Rev. Lett. **96** (2006) 011601 [hep-ph/0509280]. (Cited on page 23.)

[113] D. J. H. Chung and A. J. Long, "Electroweak Phase Transition in the $\mu\nu$SSM," Phys. Rev. D **81** (2010) 123531 (Cited on page 23.)

[114] J. Fidalgo and C. Muñoz, "The $\mu\nu$SSM with an Extra $U(1)$," JHEP **1204** (2012) 090 (Cited on page 23.)

[115] For a review, see: H. K. Dreiner, "An Introduction to explicit R-parity violation," In *Kane, G.L. (ed.): Perspectives on supersymmetry II* 565-583, World Scientific (2010) [hep-ph/9707435]. (Cited on page 23.)

[116] J. A. Casas, E. K. Katehou and C. Muñoz, "U(1) Charges in Orbifolds: Anomaly Cancellation and Phenomenological Consequences," Nucl. Phys. B **317** (1989) 171. (Cited on page 23.)

[117] J. A. Casas and C. Muñoz, "Yukawa Couplings in $SU(3)\times SU(2)\times U(1)_Y$ Orbifold Models," Phys. Lett. B **212** (1988) 343. (Cited on page 23.)

[118] F. Takayama and M. Yamaguchi, "Gravitino dark matter without R-parity," Phys. Lett. B **485** (2000) 388 (Cited on pages 24 and 25.)

[119] L. Covi, M. Grefe, A. Ibarra and D. Tran, "Unstable Gravitino Dark Matter and Neutrino Flux," JCAP **0901** (2009) 029 [arXiv:0809.5030 [hep-ph]]. (Cited on page 24.)

[120] K. Y. Choi, D. E. López-Fogliani, C. Muñoz and R. R. de Austri, "Gamma-ray detection from gravitino dark matter decay in the $\mu\nu$SSM," JCAP **03** (2010) 028 (Cited on pages 24, 25, 36, 40, 41 and 42.)

[121] W. Buchmuller, L. Covi, K. Hamaguchi, A. Ibarra and T. Yanagida, "Gravitino dark matter in R-parity breaking vacua," JHEP **03** (2007) 037 G. Bertone, W. Buchmuller, L. Covi and A. Ibarra, "Gamma-Rays from Decaying Dark Matter," JCAP **11** (2007) 003 A. Ibarra and D. Tran, "Gamma Ray Spectrum from Gravitino Dark Matter Decay," Phys. Rev. Lett. **100** (2008) 061301 K. Ishiwata, S. Matsumoto and T. Moroi, "High Energy Cosmic Rays from the Decay of Gravitino Dark Matter," Phys. Rev. **D78** (2008) 063505 W. Buchmuller, A. Ibarra, T. Shindou, F. Takayama and D. Tran, "High Energy Cosmic Rays from the Decay of Gravitino Dark Matter," JCAP **09** (2009) 021 (Cited on page 24.)

[122] J. M. Overduin and P. S. Wesson, "Dark matter and background light," Phys. Rept. **402** (2004) 267 (Cited on page 25.)

[123] A. J. Cuesta, T. E. Jeltema, F. Zandanel, S. Profumo, F. Prada, G. Yepes, A. Klypin and Y. Hoffman *et al.*, "Dark Matter decay and annihilation in the Local Universe: CLUES from Fermi," Astrophys. J. **726** (2011) L6

[124] M. Ackermann *et al.* [Fermi-LAT Collaboration], "The Fermi Large Area Telescope On Orbit: Event Classification, Instrument Response Functions, and Calibration," Astrophys. J. Suppl. **203** (2012) 4 (Cited on pages 36, 37, 39, 43 and 85.)

[125] J. C. Brown, I. J. D. Craig "Inverse Problems in Astronomy, A guide to inversion strategies for remotely sensed data," Taylor & Francis. ISBN-10: 0852743696 (1986) (Cited on pages 28, 30 and 31.)

[126] L. Bergstrom and H. Snellman, "Observable Monochromatic Photons From Cosmic Photino Annihilation," Phys. Rev. D **37** (1988) 3737 (Cited on page 30.)

[127] A. Lapi, A. Paggi, A. Cavaliere, A. Lionetto, A. Morselli and V. Vitale, "Gamma Rays from Annihilations at the Galactic Center in a Physical

Dark Matter Distribution," Astron. Astrophys. **510** (2010) id.A90 (Not cited.)

[128] V. Vitale, A. Morselli and f. t. F. Collaboration, "Indirect Search for Dark Matter from the center of the Milky Way with the Fermi-Large Area Telescope," arXiv:0912.3828 [astro-ph.HE] (Cited on page 36.)

[129] A. A. Abdo *et al.* [Fermi LAT Collaboration], "Fermi Large Area Telescope Measurements of the Diffuse Gamma-Ray Emission at Intermediate Galactic Latitudes," Phys. Rev. Lett. **103** (2009) 251101 (Cited on page 36.)

[130] K. Y. Choi, D. Restrepo, C. E. Yaguna and O. Zapata, "Indirect detection of gravitino dark matter including its three-body decays," JCAP **10** (2010) 033 (Cited on page 36.)

[131] M.A. Diaz, S. Garcia Saenz, B. Koch, "Indirect detection of gravitino dark matter including its three-body decays," Phys. Rev. **D84** (2011) 055007 (Cited on page 37.)

[132] A. A. Abdo *et al.* [Fermi LAT Collaboration], "Fermi LAT Search for Photon Lines from 30 to 200 GeV and Dark Matter Implications," Phys. Rev. Lett. **104** (2010) 091302 (Cited on page 37.)

[133] M. Ackermann *et al.* [LAT Collaboration], "Fermi LAT Search for Dark Matter in Gamma-ray Lines and the Inclusive Photon Spectrum," Phys. Rev. D **86** (2012) 022002 (Cited on pages 37, 39 and 45.)

[134] G. Vertongen and C. Weniger, "Hunting Dark Matter Gamma-Ray Lines with the Fermi LAT," JCAP **05** (2011) 027 (Cited on pages 37, 39 and 45.)

[135] A.R. Pullen, R.-R. Chary and M. Kamionkowski, Phys. Rev. **D76** (2007) 063006, Erratum-ibid. **D83** (2011) 029904 [arXiv:1109.0512 [hep-ph]] (Cited on pages 37, 40 and 41.)

[136] D. Restrepo, M. Taoso, J. W. F. Valle and O. Zapata, "Gravitino dark matter and neutrino masses with bilinear R-parity violation," Phys. Rev. D **85** (2012) 023523 (Cited on pages 37 and 40.)

[137] R. Rando and for the Fermi LAT Collaboration, "Post-launch performance of the Fermi Large Area Telescope," Contribution to the 31st ICRC, Lodz, Poland, July 2009. arXiv:0907.0626 [astro-ph.IM]. (Cited on page 37.)

[138] M. Su, T. R. Slatyer and D. P. Finkbeiner, "Giant Gamma-ray Bubbles from Fermi-LAT: AGN Activity or Bipolar Galactic Wind?," Astrophys. J. **724** (2010) 1044 (Cited on page 38.)

(Cited on page 38.)

[139] H. Yuksel and M. D. Kistler, "Dark Matter Might Decay... Just Not Today!," Phys. Rev. **D78** (2008) 023502 (Cited on pages 41 and 42.)

[140] M. Su and D. P. Finkbeiner, "Strong Evidence for Gamma-ray Line Emission from the Inner Galaxy," arXiv:1206.1616 [astro-ph.HE]. (Cited on page 44.)

[141] M. Ackermann *et al.* [Fermi-LAT Collaboration], "Constraining Dark Matter Models from a Combined Analysis of Milky Way Satellites with the Fermi Large Area Telescope," Phys. Rev. Lett. **107** (2011) 241302 (Cited on pages 54, 65 and 66.)

[142] A. A. Abdo *et al.* [Fermi-LAT Collaboration], "Observations of Milky Way Dwarf Spheroidal galaxies with the Fermi-LAT detector and constraints on Dark Matter models," Astrophys. J. **712** (2010) 147 (Cited on pages 54, 65 and 66.)

[143] A. Geringer-Sameth and S. M. Koushiappas, "Exclusion of canonical WIMPs by the joint analysis of Milky Way dwarfs with Fermi," Phys. Rev. Lett. **107** (2011) 241303 (Cited on pages 54, 65 and 66.)

[144] F. Loparco and M.N. Mazziotta, "A Bayesian approach to evaluate confidence intervals in counting experiments with background ," Nuc. Inst. Methods A646 (2011) 167 (Cited on page 61.)

[145] G. Jungman, M. Kamionkowski and K. Griest, "Supersymmetric Dark Matter," Phys. Rep. **267** (1996) 195 (Cited on page 63.)

[146] M. Cirelli, P. Panci and P.D. Serpico, "Diffuse gamma ray constraints on annihilating or decaying Dark Matter after Fermi," Nucl. Phys. **B840** (2010) 284 (Cited on page 65.)

[147] M. Papucci and A. Strumia, "Robust implications on Dark Matter from the first FERMI sky gamma map," JCAP **03** (2010) 014 (Cited on page 65.)

[148] J. Han, C. S. Frenk, V. R. Eke, L. Gao, S. D. M. White, A. Boyarsky, D. Malyshev and O. Ruchayskiy, "Constraining Extended Gamma-ray Emission from Galaxy Clusters," Mon. Not. Roy. Astron. Soc. **427** (2012) 1651 (Cited on page 66.)

[149] D. Hooper and T. Linden, "On The Origin Of The Gamma Rays From The Galactic Center," Phys. Rev. D **84** (2011) 123005 (Cited on page 66.)

[150] I. V. Moskalenko and A. W. Strong, "Anisotropic inverse Compton scattering in the galaxy," Astrophys. J. **528** (2000) 357 (Cited on page 67.)

[151] P. M. W. Kalberla, W. B. Burton, D. Hartmann, E. M. Arnal, E. Bajaja, R. Morras and W. G. L. Poppel, "The Leiden/Argentine/Bonn (LAB) survey of Galactic HI: Final data release of the combined LDS and IAR surveys with improved stray-radiation corrections," Astron. Astrophys. **440** (2005) 775 (Cited on page 68.)

[152] T. A. Porter, I. V. Moskalenko, A. W. Strong, E. Orlando and L. Bouchet, "Inverse Compton Origin of the Hard X-Ray and Soft Gamma-Ray Emission from the Galactic Ridge," Astrophys. J. **682** (2008) 400 (Cited on page 68.)

[153] G. L. Case and D. Bhattacharya, "A new sigma-d relation and its application to the galactic supernova remnant distribution," Astrophys. J. **504** (1998) 761 (Cited on page 69.)

[154] D. R. Lorimer, A. J. Faulkner, A. G. Lyne, R. N. Manchester, M. Kramer, M. A. McLaughlin, G. Hobbs and A. Possenti *et al.*, "The Parkes multibeam pulsar survey: VI. Discovery and timing of 142 pulsars and a Galactic population analysis," Mon. Not. Roy. Astron. Soc. **372** (2006) 777 (Cited on page 69.)

[155] I. Yusifov and I. Kucuk, "Revisiting the radial distribution of pulsars in the galaxy," Astron. Astrophys. **422** (2004) 545 (Cited on page 69.)

[156] L. Bronfman, S. Casassus, J. May and L. A. Nyman, "The radial distribution of ob star formation in the galaxy," Astron. Astrophys. **358** (2000) 521 (Cited on page 69.)

[157] M. A. Sanchez-Conde, "Dark matter constraints from the Fermi/LAT Extragalactic Gamma-ray Background and the role of halo substructure," American Astronomical Society Meeting Abstracts 220, (2012) #116.05. (Cited on page 74.)

[158] F. W. Stecker, T. M. Venters, "Components of the Extragalactic Gamma-ray Background," The Astrophysical Journal 736 (2011) 40 (Cited on page 74.)

[159] A. A. Abdo *et al.* [The Fermi-LAT collaboration], "Fermi Large Area Telescope First Source Catalog". The Astrophysical Journal Supplement Series 188, 405-436, (2010). (Cited on pages 75 and 76.)

[160] A. A. Abdo *et al.* [The Fermi-LAT collaboration], "The Spectrum of the Isotropic Diffuse Gamma-Ray Emission Derived From First-Year Fermi Large Area Telescope Data," Phys. Rev. Lett. **104** (2010) 101101 (Cited on page 76.)

[161] J. Zavala, V. Springel, M. Boylan-Kolchin, "Extragalactic gamma-ray background radiation from dark matter annihilation." MNRAS 405, 593-612 (2010). (Cited on page 78.)

[162] S. Ando and E. Komatsu, "Anisotropy of the cosmic gamma-ray background from dark matter annihilation," Phys. Rev. D **73** (2006) 023521 (Cited on page 75.)

[163] S. Ando, E. Komatsu, T. Narumoto and T. Totani, "Dark matter annihilation or unresolved astrophysical sources? Anisotropy probe of the origin of cosmic gamma-ray background," Phys. Rev. D **75** (2007) 063519 (Cited on page 75.)

[164] J. M. Siegal-Gaskins, "Revealing dark matter substructure with anisotropies in the diffuse gamma-ray background," JCAP **0810** (2008) 040 (Cited on page 75.)

[165] J. M. Siegal-Gaskins and V. Pavlidou, "Robust identification of isotropic diffuse gamma rays from Galactic dark matter," Phys. Rev. Lett. **102** (2009) 241301 (Cited on page 75.)

[166] S. Ando, "Gamma-ray background anisotropy from galactic dark matter substructure," Phys. Rev. D **80** (2009) 023520 (Cited on page 75.)

[167] M. Fornasa, L. Pieri, G. Bertone and E. Branchini, "Anisotropy probe of galactic and extra-galactic Dark Matter annihilations," Phys. Rev. D **80** (2009) 023518 (Cited on page 75.)

[168] J. Zavala, V. Springel and M. Boylan-Kolchin, "Mapping extragalactic dark matter structures through gamma-rays," 2009 Fermi Symposium, eConf Proceedings C091122 arXiv:1001.3307 [astro-ph.CO]. (Cited on page 75.)

[169] M. Taoso, S. Ando, G. Bertone and S. Profumo, "Angular correlations in the cosmic gamma-ray background from dark matter annihilation around

intermediate-mass black holes," Phys. Rev. D **79** (2009) 043521 (Cited on page 75.)

[170] S. Ando, E. Komatsu, T. Narumoto and T. Totani, "Angular power spectrum of gamma-ray sources for GLAST: blazars and clusters of galaxies," Mon. Not. Roy. Astron. Soc. **376** (2007) 1635 (Cited on page 75.)

[171] S. Ando and V. Pavlidou, "Imprint of galaxy clustering in the cosmic gamma-ray background," Mon. Not. Roy. Astron. Soc. **400** (2009) 2122 (Cited on page 75.)

[172] K. M. Gorski, E. Hivon, A. J. Banday, B. D. Wandelt, F. K. Hansen, M. Reinecke and M. Bartelman, "HEALPix – a Framework for High Resolution Discretization, and Fast Analysis of Data Distributed on the Sphere," Astrophys. J. **622** (2005) 759 (Cited on page 75.)

[173] M. Kamionkowski, S. M. Koushiappas, M. Kuhlen, 2010. "Galactic substructure and dark-matter annihilation in the Milky Way halo," Physical Review D 81, 043532 (Cited on pages 78 and 80.)

[174] M. A. Sánchez-Conde, M. Cannoni, F. Zandanel, M. E. Gómez, F. Prada, 2011. "Dark matter searches with Cherenkov telescopes: nearby dwarf galaxies or local galaxy clusters?," Journal of Cosmology and Astro-Particle Physics 12, 11 (Cited on pages 78 and 80.)

[175] A. Pinzke, C. Pfrommer, L. Bergström, 2011. "Prospects of detecting gamma-ray emission from galaxy clusters: Cosmic rays and dark matter annihilations," Physical Review D 84, 123509 (Cited on page 80.)

[176] A. Cuoco, E, Komatsu, J. M. Siegal-Gaskins, 2012. "Joint anisotropy and source count constraints on the contribution of blazars to the diffuse gamma-ray background," Physical Review D 86, 063004 (Cited on page 79.)

34. I dreamt I was a really old Latin American detective. I lived in New York and Mark Twain was hiring me to save the life of someone without a face. “It’s going to be a damn tough case, Mr. Twain,” I told him.

40. I dreamt that a storm of phantom numbers was the only thing left of human beings three billion years after Earth ceased to exist.

46. I dreamt I was an old Latin American detective and a mysterious Foundation hired me to find the death certificates of the Flying Spics. I was traveling all around the world: hospitals, battlefields, pulque bars, abandoned schools.

Roberto Bolaño, *Tres*.

34. Soñé que era un detective latinoamericano muy viejo. Vivía en Nueva York y Mark Twain me contrataba para salvarle la vida a alguien que no tenía rostro. Va a ser un caso condenadamente difícil, señor Twain, le decía.

40. Soñé que una tormenta de números fantasmales era lo único que quedaba de los seres humanos tres mil millones de años después de que la Tierra hubiera dejado de existir.

46. Soñé que era un viejo detective latinoamericano y que una Fundación misteriosa me encargaba encontrar las actas de defunción de los Sudacas Voladores. Viajaba por todo el mundo: hospitales, campos de batalla, pulquerías, escuelas abandonadas.

Roberto Bolaño, *Tres*.

MultiDark
Multimessenger Approach for Dark Matter Detection

ift Instituto de Física Teórica UAM-CSIC

Universidad Autónoma de Madrid
Departamento de Física Teórica